1-1-2019

Coupling of Light's Orbital Angular Momentum to a Quantum Dot Ensemble

Alaa A. Bahamran
University of Denver

Coupling of Light's Orbital Angular Momentum to a Quantum Dot Ensemble

---

A Dissertation

Presented to

the Faculty of Natural Sciences and Mathematics

University of Denver

In Partial Fulfillment

of the Requirements for the Degree

Doctor of Philosophy

---

by

Alaa A. Bahamran

March 2019

Advisor: Mark Siemens

Author: Alaa A. Bahamran
Title: Coupling of Light's Orbital Angular Momentum to a Quantum Dot Ensemble
Advisor: Mark Siemens
Degree Date: March 2019

Abstract

We theoretically and experimentally investigate the transfer of orbital angular momentum from light to an ensemble of semiconductor-based nanostructures composed of lead sulfide quantum dots. Using an ensemble of quantum dots offers a higher cross-section and more absorption of twisted light fields compared to experimentally challenging single-nanostructure measurements. However, each quantum dot (except for on-center) sees a displaced light beam parallel to its own axis of symmetry. The transition matrix elements for the light-matter interaction are calculated by expressing the displaced light beam in terms of the appropriate light field centered on the nanoparticles. The resulting transition rate induced by light's orbital angular momentum depends on the nanostructure size, the displacement between the beam center and nanostructure axis, and the ratio of the nanostructure size to the beam waist. In addition, while the strength of the transitions induced by twisted light is much weaker than those induced by plane waves for the center case, they are almost identical when conceding illuminating an ensemble of nanostructures. Although we attempted to measure this transfer of orbital angular momentum, due to experimental limitations the transfer remained undetectable.

Acknowledgements

First and foremost, my full gratitude is due to Allah who guided and assisted me to complete this work.

This dissertation would not have been completed without the help of my advisor, Dr. Mark Siemens. His guidance, encouragement, and understanding were of great help throughout my academic journey. Many thanks to Dr. Guillermo Quinter, who I owe a lot for what I have learned about twisted light; I consider myself lucky having the opportunity to learn from Dr. Quinter. I would also like to thank my committee members, Dr. Shannon Murphy, Dr. Davor Balzar, and Dr. Xin Fan, for their time and insightful comments.

I also would like to express my sincere gratitude to Dr. Zain Yamani, who has shown me what a good scientist should be; Dr. Yamani is everything one could look for in a mentor, and I cannot thank him enough for all the help and support during my academic journey. To all the faculty, staff members, and fellow students at the Department of Physics and Astronomy at the University of Denver, thank you. I also would like to thank Geoffrey Diederich for providing me with the samples used in this study. Many thanks to Brian Green, and Jasmine Andersen—it has been an honor to have met you and worked with you. And of course this work would not have been possible without the financial support from King Abdual Aziz University.

Many thanks to my supportive parents and my wonderful brothers. Their encouragement over the years is the reason I have reached this point in my education. Last but not least, I would like to express my special gratitude to my loving husband Sabry and my children Joury and Adel for their support and patience while I spent countless hours preparing this dissertation.

Table of Contents

List of Figures

Chapter 1

Introduction

For centuries, light has inspired scientists not just to understand its fundamental nature, but also to explore its potential uses. From long-wavelength infrared electromagnetic waves to high-energy γ-rays, light has been used as an instrument for probing material and solid-state physics ranging from the atomic scale to astrophysics. Light-matter interaction has been an essential tool for understanding phenomena and testing theories, and its applications have rapidly progressed in most areas of science such as biology, chemistry, and medicine.

When electromagnetic waves meet matter, many processes can be observed, including absorption, scattering, and emission (as photons at certain wavelengths or as electrons at specific energies). When considering optically induced transitions between electronic states within an atom, selection rules can be used. These selection rules are based on conservation of energy, linear momentum, and angular momentum of the electron and the photon, and they may differ depending upon the system used to observe the transition. For example,

for circularly polarized light that carries spin angular momentum, the excitation of atomic transitions must exhibit change in angular momentum equal to zero or one unit of $\hbar$ (where $\hbar$ is the reduced Planck constant or Planck's constant divided by 2π).

Selection rules have been derived assuming that light can be described by three properties: energy, linear momentum, and polarization (spin angular momentum). But Allen *et al* realized that light possesses another degree of freedom associated with its spatial profile [1]. This new degree of freedom, known as the orbital angular momentum (OAM) of light (also referred to as *twisted light*), has given rise to new selection rules. Consequently, this adds new possibilities for atomic transition excitations and a plethora of applications.

1.1 Outline of Thesis

In this thesis I will discuss my contributions to the field of light-matter interaction using light that carries OAM and how twisted light may activate forbidden optical transitions in nanostructures. Chapter 2 is an introduction to OAM with a brief history, mathematical derivation, overview of methods used to generate and measure OAM, and examples of possible twisted light applications. Chapter 3 discusses in detail the fundamentals of light-matter interaction, the concept of selection rules, and the electronic and the optical properties of the nanostructures (semiconductor quantum dots) that have been studied in this research. Then, in Chapter 4 we will explain how twisted light with OAM affects the selection rules in such interactions. Chapter 5

describes the experimental setup used to study the OAM-dependent absorption spectrum in nanostructures and the experimental results. Lastly, Chapter 6 summarizes my work in the context of the field of light-matter interaction and offers suggestions for continuation of this work in the future.

Chapter 2

Light Angular Momentum

It is well known that light carries both energy, $\hbar\omega$, and linear momentum, $\hbar k$, in the direction of propagation (where ω is the angular frequency and k is the wave number) [2]. Photons may also carry frequency-independent angular momentum in two different forms.

The most well-understood form of photonic angular momentum is associated with the direction that the electric and magnetic field rotate around the beam axis during propagation [3]. In other words, the tip of the electric field vector, at a given point in space, traces out a circle as time progresses. For such a beam, this rotation or spinning is known as spin angular momentum (SAM), and it is related to the optical polarization of the beam. Each photon can carry SAM of $\pm\hbar$ [4], aligned parallel (counter-clockwise rotation, positive) or antiparallel (clockwise rotation, negative) to the direction of propagation, or a superposition of the two when having linear polarization [5]. Figure 2.1 shows the difference between linearly polarized light and light carrying SAM when it is right-handed and left-handed circularly polarized.

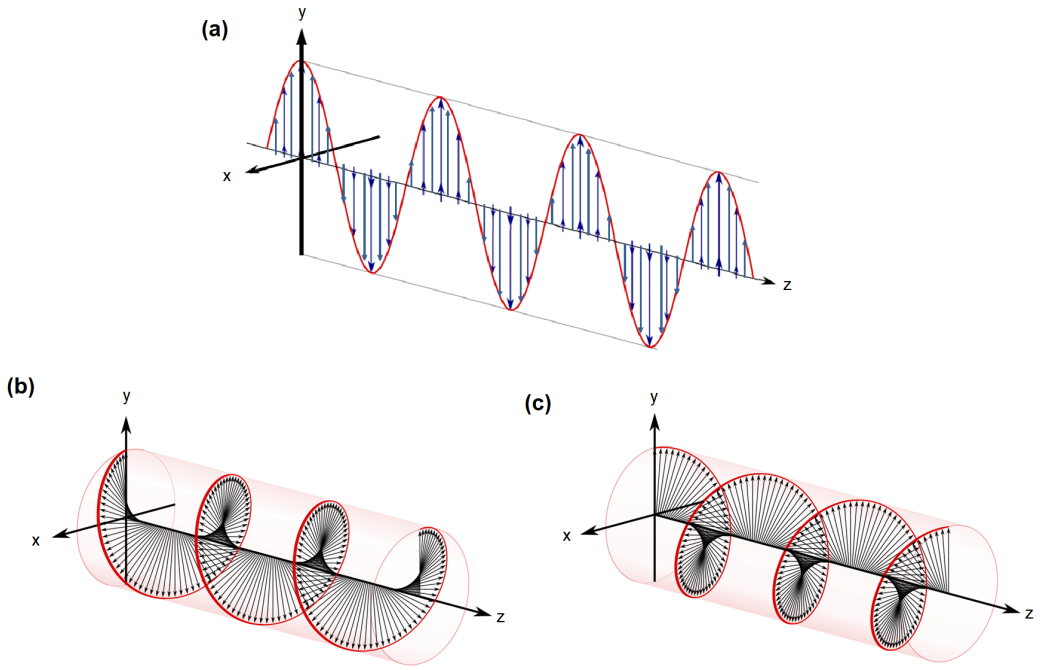

Figure 2.1: (a) Diagram of the electric field vectors for linearly polarized light propagating along the z-axis shows that the electric field is confined to a plane along the propagation direction. (b) The electric field vectors of right-handed circularly polarized light appears to be rotating clockwise (SAM of $-\hbar$). (c) The electric field vectors of left-handed circularly polarized light appears to be rotating anticlockwise (SAM of $+\hbar$) [6].

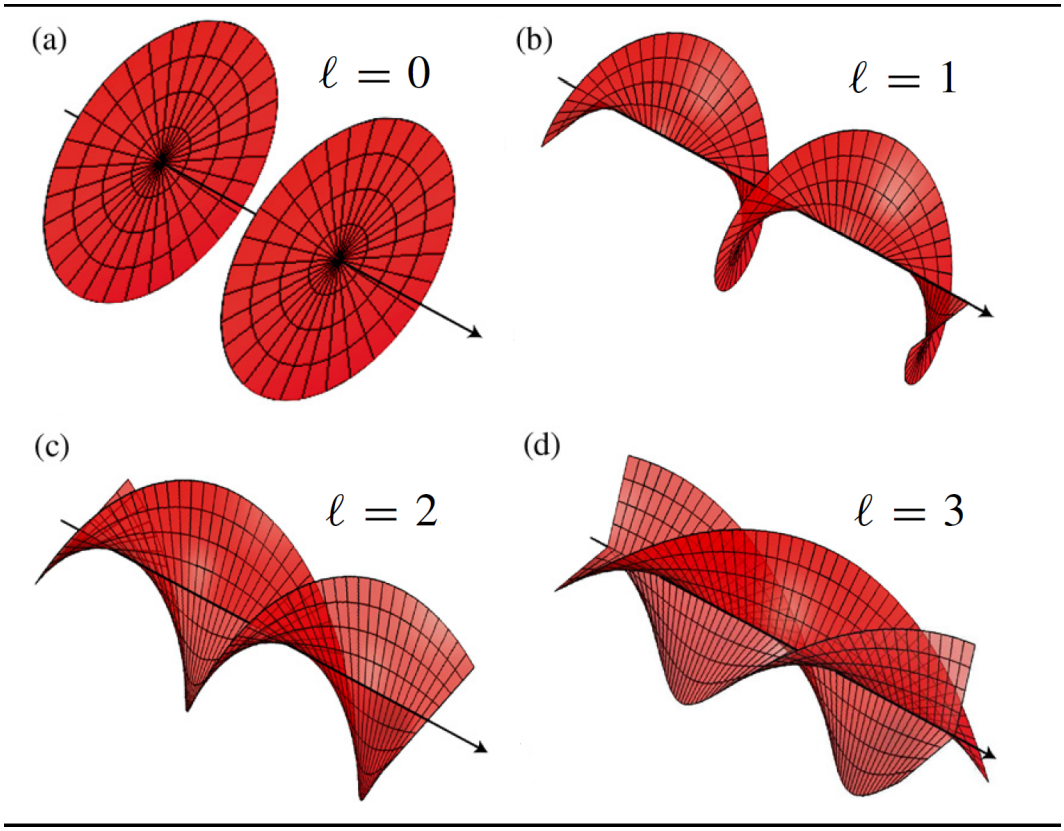

Figure 2.2: Representation of beam helical structures carrying OAM of (a) $\ell = 0$ (b) $\ell = 1$ (c) $\ell = 2$, and (d) $\ell = 3$ [7].

The second form of photonic angular momentum is associated with the helicity of the phase structure, which gives rise to the OAM of light. In other words, a light beam with helical phase fronts and an azimuthal component of the local wave vector carries OAM [7]. Figure 2.2 shows some example for beams with helical phase fronts. This type of twisted light beam has a phase singularity that gives rise to a dark spot in the center with no intensity, giving these beams their unique donut shape [8].

2.1 History of Orbital Angular Momentum

Maxwell was the first to propose that light is an electromagnetic wave, and he used a set of equations, now known as Maxwell's equations, to describe it in terms of coupled and changing electric and magnetic fields [9]. From these equations, it was clear that light, or electromagnetic waves in general, carries both energy and linear momentum. Years later, Poynting suggested that light also has angular momentum, which has a spin part associated with polarization [10]. In 1936, Beth made the first experimental observation of light's angular momentum [11]. In his experiment, circularly polarized light passed through a suspended half-wave plate. The beam polarization changed to the opposite polarization, and the half-wave birefringent plate underwent torque in transforming the angular momentum [12]. Decades later, in 1992, Allen *et al* discovered that photons in optical vortices can carry OAM independent of the beam polarization [1]. This discovery led many scientists and researchers to investigate the properties of optical OAM, leading to many applications ranging from micromachine construction to astronomical imaging [13].

2.2 Paraxial Approximation and the Wave Equation

The Helmholtz equation represents a time-independent form of the wave equation, $\nabla^2 A + k^2 A = 0$, where ∇^2 is the Laplacian and A is the wave amplitude [14]. In the paraxial approximation, which is a small-angle approximation, propagating light can be treated as a ray rather than spherical wave.

In this approximation, the angle between the wave vector and the z-axis is small, so the amplitude can be written as [15]:

$$A(\vec{r}) = u(\vec{r})e^{ikz} \tag{2.2.1}$$

and Helmholtz's equation will be:

$$(\frac{\partial^2}{\partial x^2} + \frac{\partial^2}{\partial y^2})u(\vec{r})e^{ikz} + \frac{\partial^2}{\partial z^2}u(\vec{r})e^{ikz} + k^2u(\vec{r})e^{ikz} = 0 \tag{2.2.2}$$

Applying the product role to the second term; $\frac{\partial^2}{\partial z^2}u(\vec{r})e^{ikz} = \frac{\partial^2}{\partial z^2}u(\vec{r})e^{ikz} + 2ik\frac{\partial}{\partial z}u(\vec{r})e^{ikz} - k^2u(\vec{r})e^{ikz}$, yielding:

$$\Big(\frac{\partial^2}{\partial x^2} + \frac{\partial^2}{\partial y^2}\Big)u(\vec{r})e^{ikz} + \frac{\partial^2}{\partial z^2}u(\vec{r})e^{ikz} + 2ik\frac{\partial}{\partial z}u(\vec{r})e^{ikz} = 0 \tag{2.2.3}$$

where x, y, and z are the the Cartesian coordinate, and r is the radial coordinates (and is related to the Cartesian coordinate by $r = \sqrt{x^2 + y^2}$). In the paraxial regime, u is a slowly varying function of z , so the second spatial derivative in the propagation direction ($\frac{\partial^2}{\partial z^2}u$) is neglected in comparison with the term $k\frac{\partial}{\partial z}u$. In this paraxial case, equation 2.2.3 reduces to:

$$\Big(\frac{\partial^2}{\partial x^2} + \frac{\partial^2}{\partial y^2}\Big)u(\vec{r})e^{ikz} + 2ik\frac{\partial}{\partial z}u(\vec{r})e^{ikz} = 0 \tag{2.2.4}$$

Which can be written as:

$$\nabla_\perp^2 A(\vec{r}) + 2ik\frac{\partial}{\partial z}A(\vec{r}) = 0 \tag{2.2.5}$$

In general, the polarization and the field amplitude, u, are coupled by Maxwell's equations. However, in a paraxial beam, they are separated and can be controlled separately, and the electric field of the propagated light is given by:

$$\vec{E}(\vec{r},t) = \vec{e}(\vec{r},t)u(\vec{r})e^{ikz-\omega t} \tag{2.2.6}$$

where t is time and $\vec{e}(\vec{r},t)$ is polarization [16]. The possibility that the SAM (polarization) and OAM contributions to the total angular momentum can be separated for paraxial light beams has attracted researchers' attention in the past decade because it suggests a variety of applications for twisted light [17, 18].

2.3 Orbital Angular Momentum Modes

A simple Gaussian beam is a solution to the paraxial wave equation [19]. For a beam propagating in the z direction, the time-independent part of the electric field for a Gaussian beam is given by:

$$E(r,z) = E_0\left(\frac{\omega_0}{\omega(z)}\right)\exp\left[-ik\frac{r^2}{2R(z)}\right]\exp\left[-\frac{r^2}{\omega^2(z)}\right]\exp\big[-i\psi(z)\big] \tag{2.3.1}$$

where E_0 is the electric field amplitude at the origin, $R(z)$ is the radius of curvature of the beam's wavefronts at z (given by $R(z) = z\left[1+\left(\frac{\pi\omega_0^2}{\lambda z}\right)^2\right]$, where ω_0 is the waist radius at the focus, λ is the wavelength), $\omega(z)$ is the waist radius (given by $\omega(z) = \omega_0\sqrt{1+\frac{z^2}{z_R^2}}$, where z_R is the Rayleigh range), and $\psi(z)$ is the Gaussian mode Gouy phase, which is an additional phase shift

that occurs in the beam propagation, and it is given by [20]:

$$\psi(z) = \tan^{-1}\left(\frac{z}{z_R}\right)$$

Some higher-order modes satisfy the paraxial equation: Hermite-Gaussian, Laguerre-Gaussian, Ince-Gaussian, and Bessel-Gauss beams. When considering rectangular symmetry, the solutions are Hermite-Gaussian modes, as writing the paraxial Helmholtz equation in Cartesian coordinates allows the separation in x and y [21]. When considering circular symmetry, the solutions are Laguerre-Gaussian modes, where the paraxial wave equation is written in cylindrical coordinates [22].

The complex mode of a Hermite-Gaussian is:

$$u^{HG}_{m,n}(x,y,z) = C^{HG}_{m,n}\left(\frac{1}{\omega(z)}\right)\exp\left[-ik\frac{x^2+y^2}{2R(z)}\right]\exp\left[-\frac{x^2+y^2}{\omega^2(z)}\right]$$

$$\exp\Big[-i(m+n+1)\psi(z)\Big]H_m\left(\frac{x\sqrt{2}}{\omega(z)}\right)H_n\left(\frac{y\sqrt{2}}{\omega(z)}\right) \tag{2.3.2}$$

where the mode order (m,n) refers to the x and y directions, $H_m$and H_n are Hermite polynomials, C^{HG}_{mn} is the normalization constant (defined below), and the term $(m+n+1)\psi(z)$ is the Hermite-Gaussian mode Gouy phase. H_m and $C^{HG}_{mn}$are given by [23]:

$$H_m(q) = (-1)^m e^{u^2}\frac{d^m}{du^m}\Big(e^{-q^2}\Big)$$

$$C^{HG}_{mn} = \sqrt{\tfrac{2}{\pi n!m!}}2^{-N/2}, \text{ where } N = n+m$$

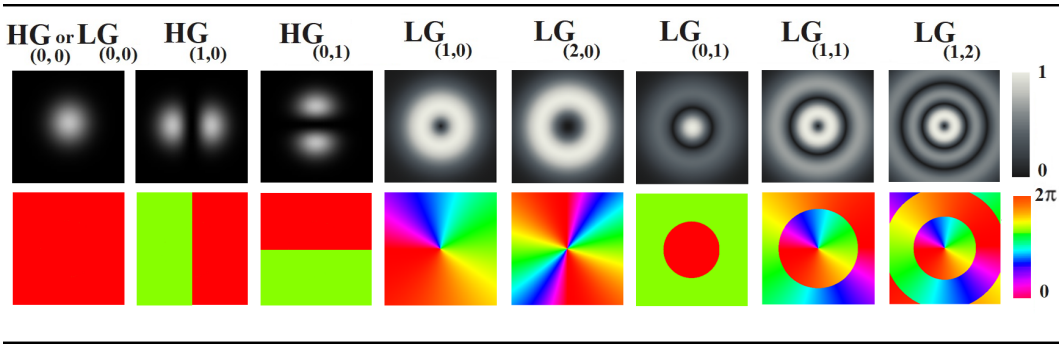

Figure 2.3: Various Hermite-Gaussian and Laguerre-Gaussian modes; normalized intensity structures (top row) and the corresponding phase profiles (bottom row).

On the other hand, the mode of a Laguerre-Gaussian is given by [7, 8]:

$$u_{\ell p}^{LG}(r,\phi,z) = C_{\ell p}^{LG}\left(\frac{1}{\omega(z)}\right)\exp\left[-ik\frac{r^2}{2R(z)}\right]\exp\left[-\frac{r^2}{\omega^2(z)}\right]\left[\frac{r\sqrt{2}}{\omega(z)}\right]^{|\ell|}$$

$$L_p^{|\ell|}\left(\frac{2r^2}{\omega^2(z)}\right)\exp[-i(2p+|\ell|+1)\psi(z)]\exp\left[-i\ell\phi\right] \tag{2.3.3}$$

where ϕ is the angular coordinate, ℓ is the azimuthal quantum number (also known as the topological charge), p is the radial quantum number, $(2p+|\ell|+1)\psi(z)$ is the Laguerre-Gaussian Gouy phase, L_n is the Laguerre polynomial, and $C_{\ell p}^{LG}$ is normalization constant:

$$L_p^{|\ell|}(x) = \frac{x^{-\ell}e^x}{n!}\frac{d^p}{dx^p}\left(x^{p+\ell}e^{-x}\right)$$

$$C_{\ell p}^{LG} = (-1)^p\sqrt{\frac{2p!}{\pi(|\ell|+p)!}}$$

The fundamental Gaussian beam is the lowest-order mode in both of Hermite-Gaussian and Laguerre-Gaussian. In other words, both u_{00}^{LG} and $u_{00}^{HG}$are the same simple Gaussian mode. Figure 2.3 shows the intensity dis-

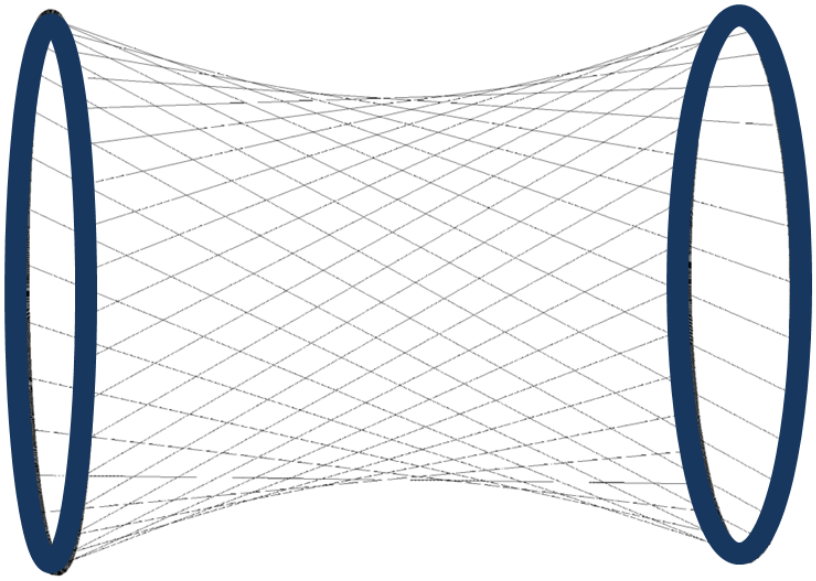

Figure 2.4: String hyperboloid helps visualize twisted light, where each string represents a photon traveling in a straight line.

tribution of several Hermite-Gaussian and Laguerre-Gaussian modes and the corresponding phase profiles.

The energy flux of a light beam can be defined by the Poynting vector (which is defined by the vector product of the electric field and the magnetic field), and it is always perpendicular to the phase front [24]. Laguerre-Gaussian modes (and other modes of twisted beams) have a helical phase term, $e^{i\ell\phi}$(where ℓ can be any integer, positive or negative). The wavefronts for such beams have a Poynting vector that is twisting around the beam axis. Allen *et al* were the first to identify that such beams carry an OAM of $\ell\hbar$ per photon [1].

An effective way to visualize a twisted beam is the string hyperboloid (see Figure 2.4). Each string represents a photon traveling in a straight line (as it should) but with skew. This geometry can be seen clearly in the work done by Berry *et al*, which calculates Poynting trajectories for Laguerre-Gauss beams. These trajectories are twisting around hyperboloidal surfaces and form a set of straight skew rays lying on hyperboloidal surfaces [25].

2.4 Generating Light with OAM

Light with OAM can be can be created artificially through a variety of methods. In the following sections, some of these methods are discussed briefly.

2.4.1 Spiral Phase Plate

The most direct way to generate a twisted beam is to pass a plane wave through a glass plate with a helical surface (a spiral phase plate) [26], as shown in Figure 2.5. The thickness of the plate increases with the azimuthal position, such that the thickness varies circumferentially around the plate but is uniform radially. The plate thickness (d) is related to the OAM value as: $d = \frac{\lambda \ell \phi}{2\pi}(n-1)$, where ϕ is the azimuthal angle, n is the refractive index of the plate, and ℓ is the topological charge of the plate [27]. The variations in optical path length generate the characteristic twisted phasefront [28, 29].

Spiral phase plates are efficient, but they are relatively expensive to make and provide no control over the radial mode. Also, a given plate only works for certain wavelengths, and they are restricted to a particular ℓ mode of the OAM of light.

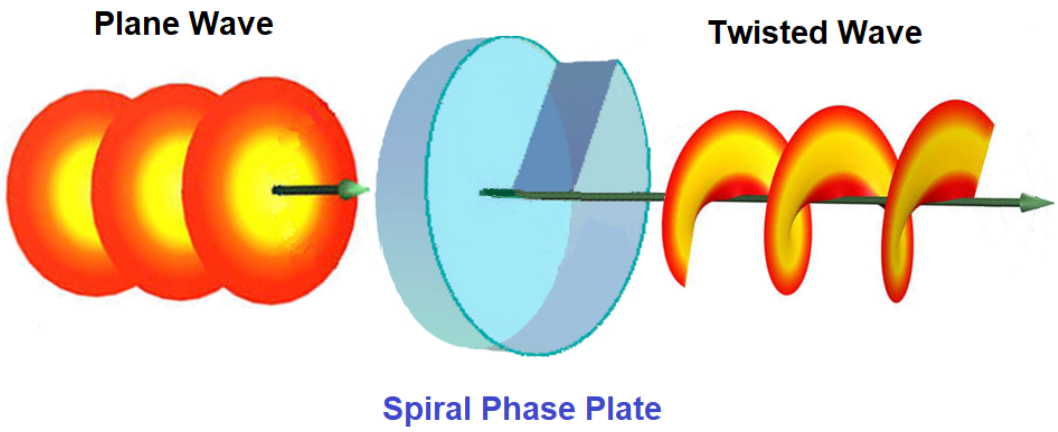

Figure 2.5: Generating a helically phased beam from a Gaussian mode by a spiral phase plate.

2.4.2 Cylindrical Mode Converters

A light beam with a helical wavefront can also be generated by converting a diagonally aligned Hermite-Gaussian beam at 45° into a Laguerre-Gaussian mode by using two cylindrical lenses [26], as shown in Figure 2.6. Diagonally aligned Hermite-Gaussian beams can be decomposed into vertical and horizontal components of a Hermite-Gaussian mode (where Hermite-Gaussian components are in phase). These Hermite-Gaussian components can combine to form a Laguerre-Gaussian beam when rephased. Therefore, due to the anisotropic focusing within the cylindrical lenses, they need to be placed at a specific distance in order to introduce a Gouy phase shift between these sets of Hermite-Gaussian modes. This is because each set of Hermite-Gaussian modes goes through a different Gouy phase shift depending on the orientation of the lens [30].

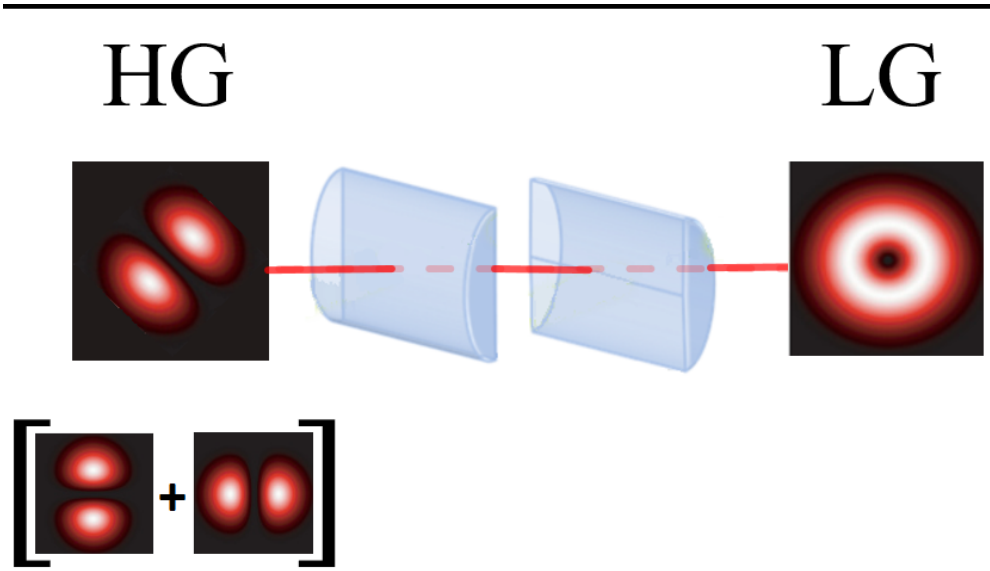

Figure 2.6: Cylindrical mode converter transforms Hermite-Gaussian mode (HG) into Laguerre-Gaussian mode (LG).

Although this method is very effective, every Laguerre-Gaussian mode needs a specific Hermite-Gaussian mode as the input, which limits the range of Laguerre-Gaussian modes that can be produced [31].

2.4.3 Computer-Generated Holograms

Probably the most convenient method of creating helical beams relies on digital holograms. Holograms are physical structures that diffract light into images. Numerically calculated holograms have been the most common method of generating twisted light. These holographic films can be displayed on a spatial light modulator (SLM). An SLM is a liquid-crystal device that has individually addressable pixels that can be programmed by computer. The design on the SLM can be modified by simply changing the image displayed on the computer. Light with OAM can be generated by displaying a forked

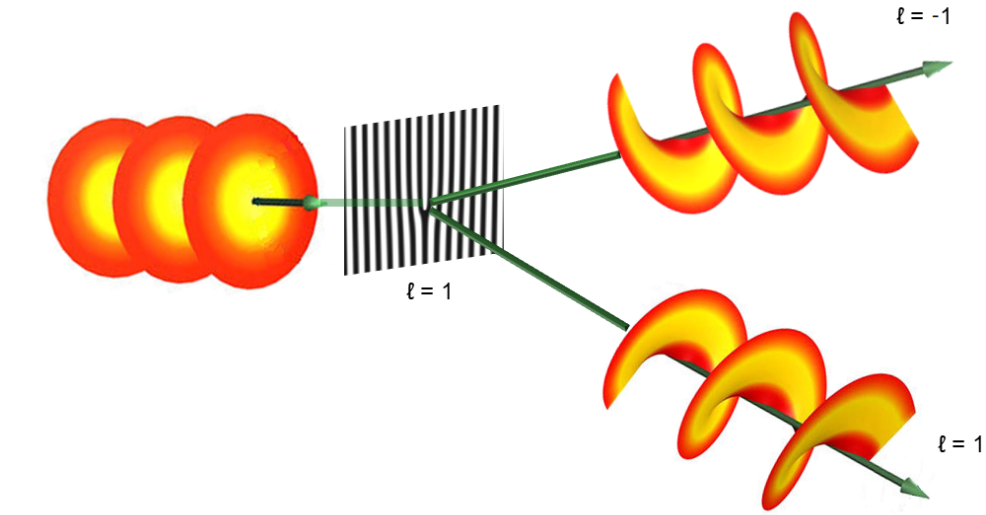

Figure 2.7: When illuminating a fork grating by a beam with a plane wavefront, it produces diffracted beams with helical wavefronts.

diffraction grating on the SLM. A normal diffraction grating consists of parallel lines, while a forked grating has a fork-like dislocation at the center. This method is simply based on diffractive optics [32, 33], and by increasing the difference between the number of lines above and under the dislocation, a higher OAM state can be generated [34]. A diffraction grating can be generated by numerically computing the intensity profile that results from interference between a tilted plane wave and a twisted wave. Then, when a plane wavefront beam shines on this grating, different beams are created, having, for example, values of ℓ = -1, 0, 1 [35]. Figure 2.7 shows a forked grating illuminated by a plane wave. By changing the displayed fork grating, a wide range of twisted light beams with different OAM states can be generated easily in the laboratory. In addition, unlike with a spiral wave plate, fork gratings are not restricted to a particular wavelength—which makes the SLM one of the

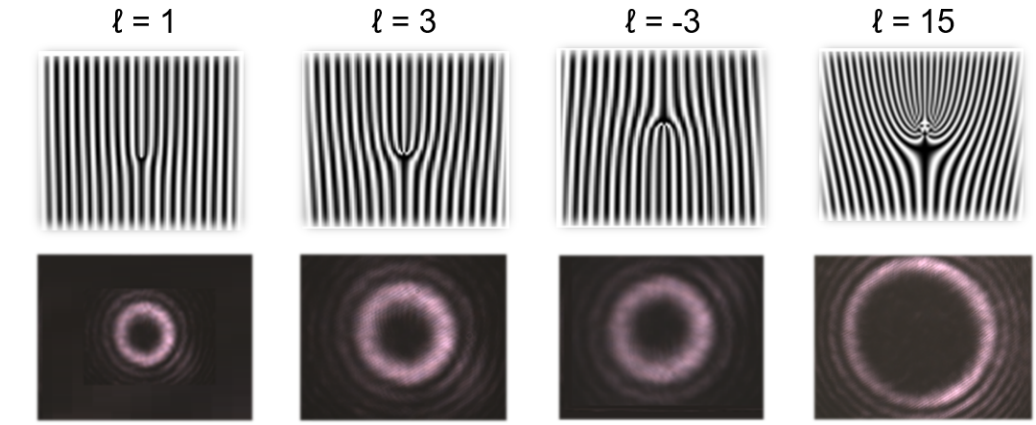

Figure 2.8: Fork diffraction gratings for $\ell = 1, 3, -3$, and 15 and the correspond generated donut modes.

most popular methods for producing twisted beams. We also can control the amplitude on a fork grating by modulating grating intensity. Figure 2.8 shows some examples of fork diffraction gratings displayed on SLM and the donut modes generated when illuminating the SLM by a plane wave (the code used to generate these fork diffraction gratings is shown in Appendix A).

2.5 Measuring OAM

Conventionally, measuring light refers to measuring its intensity. However, what makes light with OAM different from all other light beams is the fact that the phase of the wavefront is changing around the beam. Therefore, we need to find different methods to measure the value of OAM because no electronics can measure the phase directly. Some of these techniques are described in the following sections.

2.5.1 Filtering

The previous section described methods for producing twisted beams, and by the reversibility of optics, the same methods can be applied to measure the OAM state. This can be done by using a filtering tool such as single-mode fiber (SMF), which allows a specific mode to propagate through [36]. For example, if a spiral phase plate converts a plane wave into a twisted wave with topological charge $\ell = 1$, by passing this helically phased beam backwards through the same spiral phase plate, the helical phase will be decreased by 2π, and a beam with flat phase will be generated. Only photons with $\ell = 0$ will couple onto the fiber and be detected. Therefore, by detecting this plane wave, and from the spiral phase plate topological charge, one can determine the photon's original OAM state. However, any other beam with $\ell \neq 1$ passing through the spiral phase plate will not be plane wave and will not be detected. This filtering method was also used by Zeilinger's group to measure the OAM using a fork diffraction grating and SMF [37].

2.5.2 Interference

Another way to measure OAM is to interfere the beam with a reference beam. If the reference is a Gaussian beam, then the interference pattern would contain ℓ dark spokes [39, 40]. By adjusting the reference beam focus, the spokes will move one way, straighten out, and then go in the opposite direction. When the angle between the signal and reference beam is increased, these spokes join the straight-line fringes, producing a forked diffraction pattern where the number of forks determines the OAM value of the signal beam

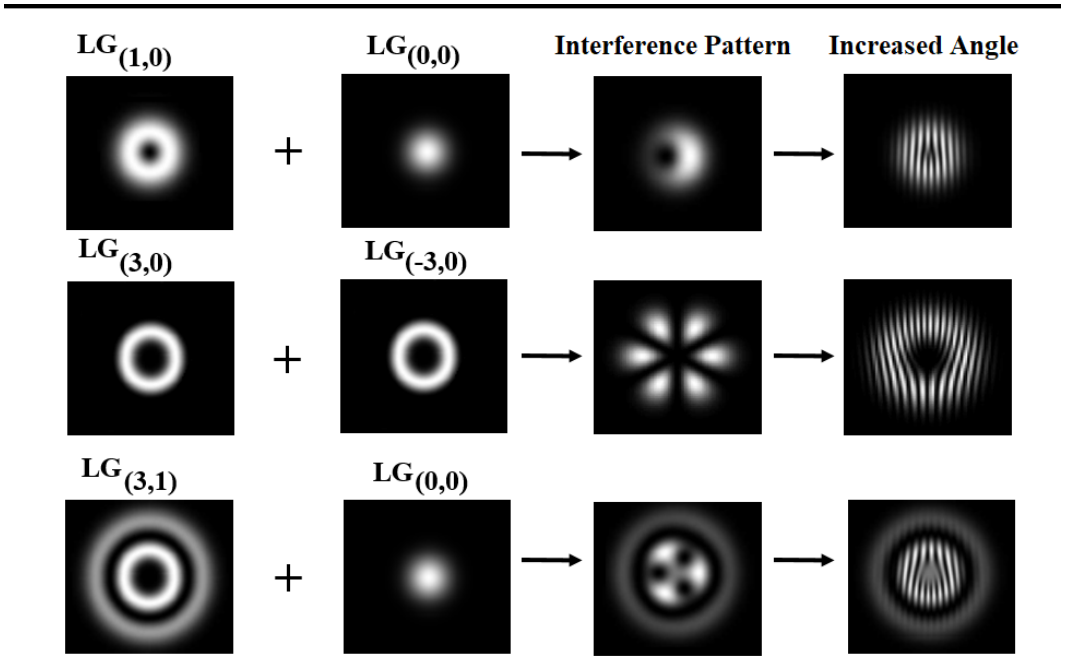

Figure 2.9: Interference between different Laguerre-Gaussian modes produces radial fringes. By increasing the angle between the two beams, a forked diffraction pattern will be formed [38].

[41]. Also, it is sometimes easier to interfere the signal beam (ℓ) with its own mirror image ($-\ell$) rather than with a plane wave. The phase difference between these two beams is $\exp(i2\ell\phi)$, so the dark spokes will be doubled in the interference pattern [38]. However, in this technique the sign of the OAM would be lost. Figure 2.9 shows interference of several Laguerre-Gaussian modes with Gaussian beam $LG_{(0,0)}$ and with its own mirror.

This method is effective for qualitative assessment of the nearest integral value of the OAM. However, DErrico *et al* proposed a more quantitative method that uses azimuthal Fourier analysis of the pattern of the interference, which allows determination of the radial and azimuthal quantum number of a twisted light beam [42].

2.5.3 Diffraction

The OAM value can also be measured by looking at diffraction patterns through a triangular (or other shapes) aperture. When light with OAM passes through the triangular aperture, it forms in the far field a diffraction pattern that looks like a triangular lattice of bright spots. The number of these spots is directly related to the value and the sign of the OAM state. For a beam with OAM = ℓ, the triangular lattice will have ℓ+1 bright spots per side. Also, for negative values of ℓ, the whole diffraction pattern flips, as shown in Figure 2.10. For this technique the phase singularity must be at the center of the triangular aperture, and the edges of the aperture must be illuminated by the inner border of the beam. [43, 44]

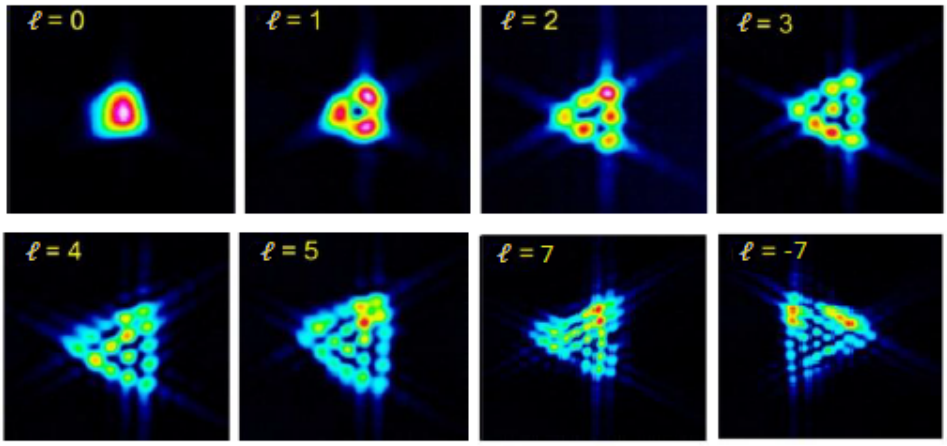

Figure 2.10: The diffraction of a twisted beam by a triangular aperture produces a triangle lattice pattern that depends on the value of ℓ and its sign. These diffraction patterns are for a beam with ℓ from 0 to 5, and for ℓ= 7 and -7. [44]

2.6 OAM Applications

The orthogonal angular momenta possibilities adds a new degree of freedom to optical technologies. This is an enabling tool that can lead to widespread applications in numerous areas of science and technology, where its use facilitates exploring in both the micro and macro scales [45]. Some examples of possible applications are explained briefly in the following sections.

2.6.1 Optical Tweezers

Optical tweezers are scientific tools that use a tightly focused laser beam to physically hold and trap microscopic dielectric materials [46]. For a highly

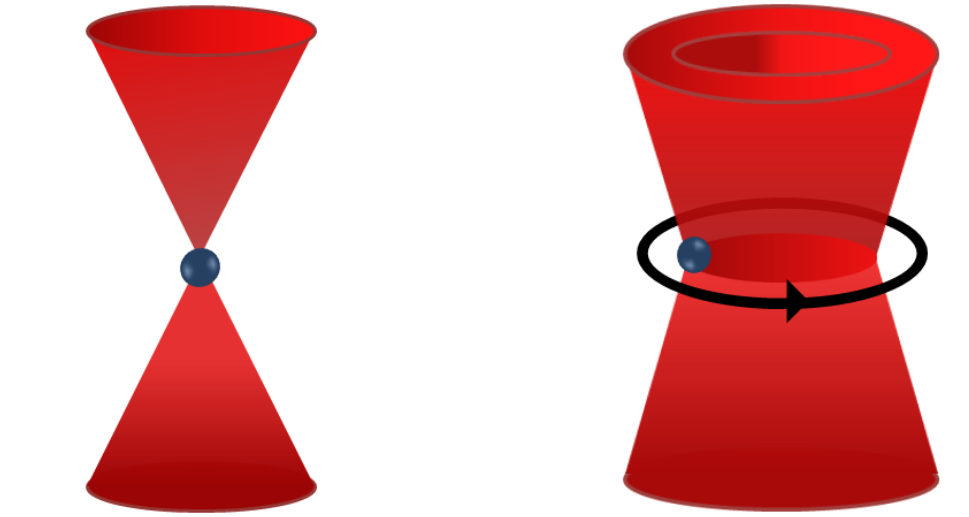

Figure 2.11: Left, a particle trapped by a focused Gaussian beam; right, a focused OAM beam traps and rotates the particle about the optical axis.

focused Gaussian beam, the beam waist has a very strong electric field gradient that attracts the dielectric particle to the region where the electric field is highest. The particle will also undergo a force due to transfer of liner momentum from the scattering or refraction of photons. These scattering and gradient forces result in the particle being trapped [47]. When adding OAM to the trapping light, the angular momentum of photons can be transferred to the trapped particles, under appropriate conditions. This transfer of angular momentum causes rotation and the associated torque is proportional proportional to the ℓ of the trapping laser [48–50]. Figure 2.11 shows a particle trapped by a focused plane wave and a particle trapped by a twisted light beam. These trapping and rotating properties have important applications in micromanipulation and in studying a variety of biological systems [51, 52].

2.6.2 Communication

Light with OAM has exciting potential for applications in both quantum and free-space communication. While the SAM of light offers only two orthogonal states corresponding to the circular polarization, $\pm\hbar$, OAM offers potentially unlimited values of ℓ states, which gives an infinite possibility of OAM values [53]. This infinite set of OAM states offers potential for high-bandwidth information encoding in optical communications. In 2004, information encoded as OAM states of light was transferred in free space [54]. Later, Willner's group demonstrated free-space propagation information transfer speeds of 2.56 Tbit/s by multiplexing 16 OAM states, and they achieved a spectral efficiency of 95.7 bit s^{-1} Hz^{-1} [55]. Willner's group also demonstrated information transfer in optical fiber and some other scenarios [56]. In fiber-optic communications, they used four OAM modes at a single wavelength and reached 400 Gbits/s data transmission; they also reached 1.6 Tbits/s using two OAM modes over 10 wavelengths [57]. However, OAM modes are not eigenmodes of commercial multimode optical fiber, and they would not be propagated at all through single-mode fiber; therefore, custom fiber is required to support OAM modes directly [58].

Moreover, atmospheric turbulence creates aberrations affecting the phase structure, and consequently the OAM purity, when signals propagate through space. Therefore, some researchers are studying the influence of atmospheric turbulence on OAM communication in an effort to minimize these effects [59].

2.6.3 Imaging

Light with OAM might also be used in imaging to explore various physical and biological properties of matter [60], and it has potential not only at very small scales, such as in nanostructures and cells, but also at very large scales, such as in astronomy.

Light with a helical wavefront has been used for a superresolution imaging technique known as stimulated emission depletion microscopy (STED), a fluorescence microscopy method able to overcome the diffraction-limited resolution of confocal microscopes [61]. This technique was first described in theory by Stephan Hell in 1994 [62]. Resolution enhancement involves using pairs of synchronized laser pulses consisting of an excitation laser pulse and a depletion laser pulse that carries OAM. The first laser pulse is used to excite the fluorescence dye molecules and produces an ordinary diffraction-limited focus. This pulse is followed by the depletion laser pulse, or STED laser, which is red-shifted in frequency to the dye emission spectrum [63]. Due to the donut shape of the STED beam, only the fluorescence from molecules at the edge of the excitation focus is reduced by stimulated emission, and in the center of the optical vortex the fluorescence remains unaffected and can be collected on a photodetector [64]. Figure 2.12 compares STED and confocal images of the same sample cell.

Twisted light has been used in imaging not only the micro regime, but also at macro scales such as those of stars and planets. The optical vortex coronagraph is a high-contrast imaging system that relies on light with OAM and allows detection of faint objects near very bright objects. For example,

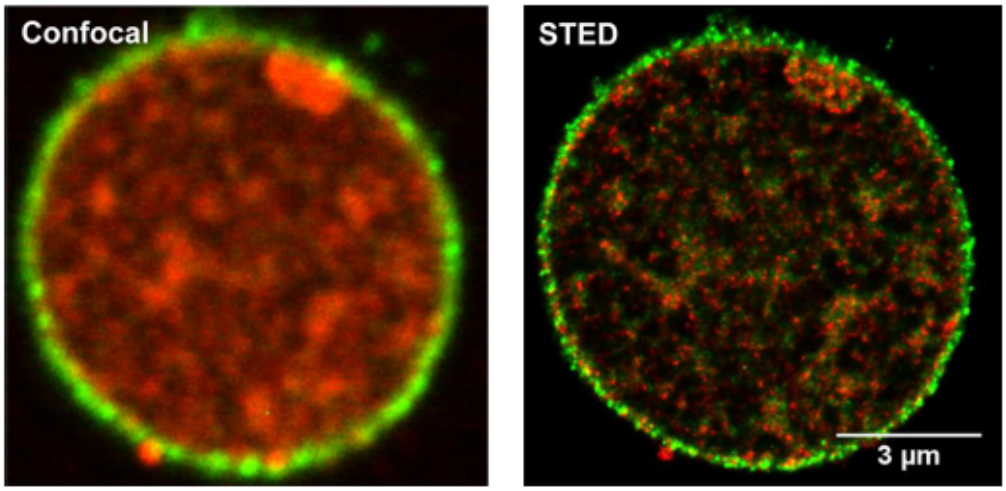

Figure 2.12: A confocal image of a sample cell (left) and a higher-resolution STED image of the same cell (right). [64].

using an optical vortex coronagraph in telescopes has allowed astronomers to view the solar corona or detect exoplanets orbiting distant stars [65–67].

The basic operating principle of the optical vortex coronagraph when imaging a bright star and a fainter companion object involves placing a spiral phase plate at the telescope's focal plane. The bright star is centered on the telescope axis so that its light passes through the spiral phase plate and generates an optical vortex that is focused to a donut shape instead of a circular spot, while an off-axis, dimmer object would be focused to a single spot. A Lyot mask is placed to block the ring of the brighter star and allow direct imaging of the dimmer object [69]. Figure 2.13 shows an example of an image produced by the Subaru Telescope using the optical vortex coronagraph technique for a young star called κ Andromedae and a planetary-mass companion. The left side of the figure shows that the companion is partially hidden by the glare from the star. At right, imaging using the optical vortex coronagraph

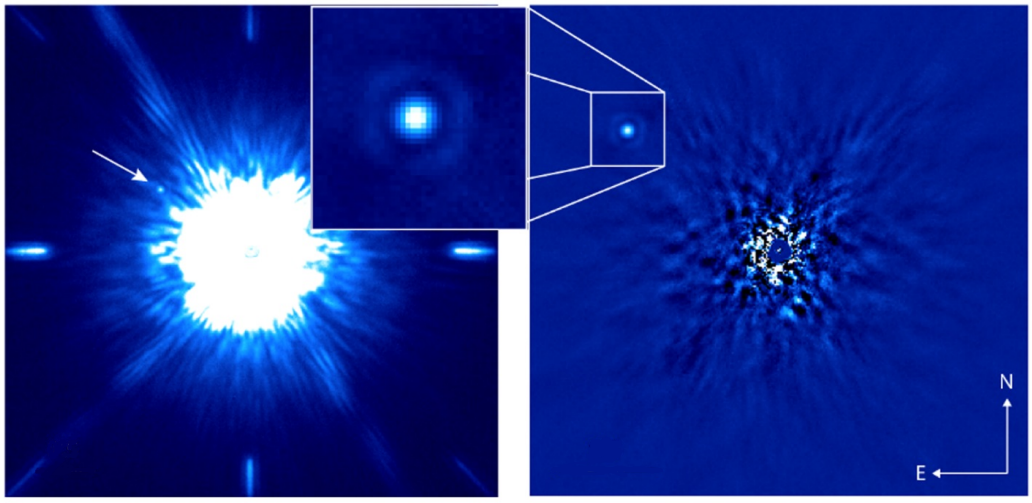

Figure 2.13: Subaru Telescope images of the young star κ Andromedae, as obtained on November 12, 2016. The planetary-mass companion is hardly visible in the conventional image (left), but is clearly detected when using the optical vortex coronagraph technique (right) [68].

method reduces the star's glare significantly, which renders the companion object detectable [68].

2.7 Conclusion

In this chapter, I have presented an introduction to OAM with a brief history and mathematical derivation. Also, an overview of a variety of methods used to generate twisted light was given, including spiral phase plates, cylindrical mode converters, and computer-generated holograms. In addition, some methods used to detect and distinguish different OAM states were discussed briefly. Finally, a discussion of possible applications for light with OAM was presented. In the following chapters, I will discuss in detail the way that twisted light interacts with matter and how such light could act differently in

this interaction. First, we explore the fundamentals of light-matter interaction in the next chapter.

Chapter 3

Light-Matter Interaction

In the previous chapter we provided an overview of twisted waves and how they differ from plane waves. In other words, we have covered the *light* part; now it is appropriate to cover the *matter* part. In this chapter, we discuss the optical properties of semiconductor quantum dot nanostructures and the fundamentals of light-matter interaction.

3.1 Atomic Structure

The study of matter and what it is made up of has been attracting scientists' attention for centuries. In fact, the idea that matter consists of indivisible units (atoms) appeared in many ancient cultures during the fifth century [70]. However, one of the earliest fundamental models to describe the atom was proposed by Niels Bohr in 1913 [71]. In this model, a small nucleus (with a positive charge) is surrounded by electrons (negatively charged) that revolve around the nucleus in circular orbits in a manner similar to that of planets

orbiting the sun [72]. Although the Bohr model is significant (it explains the Rydberg formula for the hydrogen atomic spectrum), it is no longer considered a valid model because it fails to explain the Zeeman effect and cannot predict the spectra of larger atoms [73].

Since the Bohr model, observations (of black body radiation and the photoelectric effect, for example) have shown how light waves could behave like particles. The de Broglie hypothesis, which states that particles could also behave like waves, introduced the idea that electrons behave with wave and particle properties at the same time (*i.e.*, wave-particle duality). Because of this concept, the classical mechanical model was replaced by the theory of quantum mechanics [74].

Rather than placing the electron in a certain orbit around the nucleus, the quantum mechanical approach describes an area in space around the nucleus of an atom, known as the atomic orbital, and expresses the electron's behavior by the wavefunction, ψ. This function allows us to determine the probability (rather than certainty) of finding electrons at certain energy levels within an atom. Each electron in an atom can be defined by four quantum numbers (n, l, m, and m_s).

The principal quantum number, n, defines the energy of the electron and the orbital size. It can have positive integer values, and orbitals with the same value of n are in the same "shell." The angular momentum quantum number, l, describes the orbital shape with a specific principal quantum number (this is not the azimuthal quantum number, ℓ, discussed in Chapter 2). l can be any positive integer number ranging from 0 to $n-1$, and it divides the shells into "subshells." The magnetic quantum number, m, describes the orientation of a

specific orbital in space. Each subshell has $2l+1$ orbitals, and the orbitals in a given subshell have the same energy, n, but different orientations in space, m. Finally, the spin quantum number, m_s, defines the spinning direction of the electron. It can be $+\frac{1}{2}$ or $-\frac{1}{2}$. Each subshell may be occupied by two electrons, one of them with a spin of $+\frac{1}{2}$ and the other with a spin of $-\frac{1}{2}$ [75].

Although Bohr proposed a model for the hydrogen atom that explained the spectrum for a simple hydrogen-like atom, to study the details of the structure we need to solve the time-independent Schrödinger equation [76]:

$$\hat{H}|\psi\rangle = E|\psi\rangle \tag{3.1.1}$$

where E is a constant and equivalent to the total energy of the system, and $\hat{H}$ is the Hamiltonian operator that defines the total energy of the system. This Hamiltonian is given by $T+V$, where T is the kinetic energy equal to $p^2/2m_e$ and V is the potential energy defined by the Coulomb potential given by: $-Ze^2/4\pi\epsilon_0 r$, where p is the momentum, m_e is the mass of the electron, Z is the charge of the nucleus (Z=1 for hydrogen), e is the charge of the electron, and ϵ_0 is the vacuum permittivity. By using $p = -i\hbar\nabla$, the Hamiltonian can be written as:

$$\hat{H} = -\frac{\hbar^2}{2m_e}\nabla^2 - \frac{Ze^2}{4\pi\epsilon_0 r} \tag{3.1.2}$$

Using the reduced mass $m_e \to \mu$, where $\mu = \frac{m_e m_p}{m_e+m_p}$ and m_p is the hydrogen nucleus mass (a proton mass), applying the Hamiltonian to the Schrödinger equation 3.1.1 gives us:

$$\nabla^2\psi(\vec{r}) + \frac{2\mu}{\hbar^2}\left(E + \frac{Ze^2}{4\pi\epsilon_0 r}\right)\psi(\vec{r}) = 0 \tag{3.1.3}$$

which can be solved in spherical coordinates by writing the Laplacian in spherical coordinates as [77]:

$$\nabla^2 \rightarrow \frac{1}{r^2}\frac{\partial}{\partial r}\left(r^2\frac{\partial}{\partial r}\right) + \frac{1}{r^2\sin\theta}\frac{\partial}{\partial\theta}\left(\sin\theta\frac{\partial}{\partial\theta}\right) + \frac{1}{r^2\sin^2\theta}\frac{\partial^2}{\partial\phi^2} \tag{3.1.4}$$

The wavefunction for hydrogen can be found by solving equation 3.1.3 where the radial variable and angular variable are separable, and the solution is given by:

$$\psi_{nlm}(r,\theta,\phi) = R_{nl}(r)Y_{lm}(\theta,\phi) \tag{3.1.5}$$

where $R_{nl}(r)$ is the radial wavefunction and $Y_{lm}(\theta,\phi)$ is the spherical harmonics, and they are given by [72]:

$$R_{nl}(r) = \sqrt{\frac{(n-l-1)!}{2n(n+1)!^3}}\left(\frac{2Z}{na_0}\right)^{3/2} e^{-\frac{Zr}{na_0}}\left(\frac{2Zr}{na_0}\right)^l L_{n+l}^{2l+1}\left(\frac{2Zr}{na_0}\right) \tag{3.1.6}$$

$$Y_{lm}(\theta,\phi) = (-1)^m\sqrt{\frac{(2l+1)}{4\pi}\frac{(l-m)!}{(l+m)!}}P_l^m(\cos\theta)e^{im\phi} \tag{3.1.7}$$

where L_{n+l}^{2l+1} is the Laguerre polynomial, a_0 is the Bohr radius equal to $4\pi\epsilon_0\hbar^2/m_e e^2$, and $P_l^m(\cos\theta)$ is the associated Legendre polynomial. Figure 3.1 illustrates spherical polar plots for the first few spherical harmonics.

3.2 Atomic Transition

Typically, an atom exists in a stable configuration that corresponds to the lowest energy level. When each electron is in the lowest possible energy state, the whole atom will be in ground state. An atomic transition can take

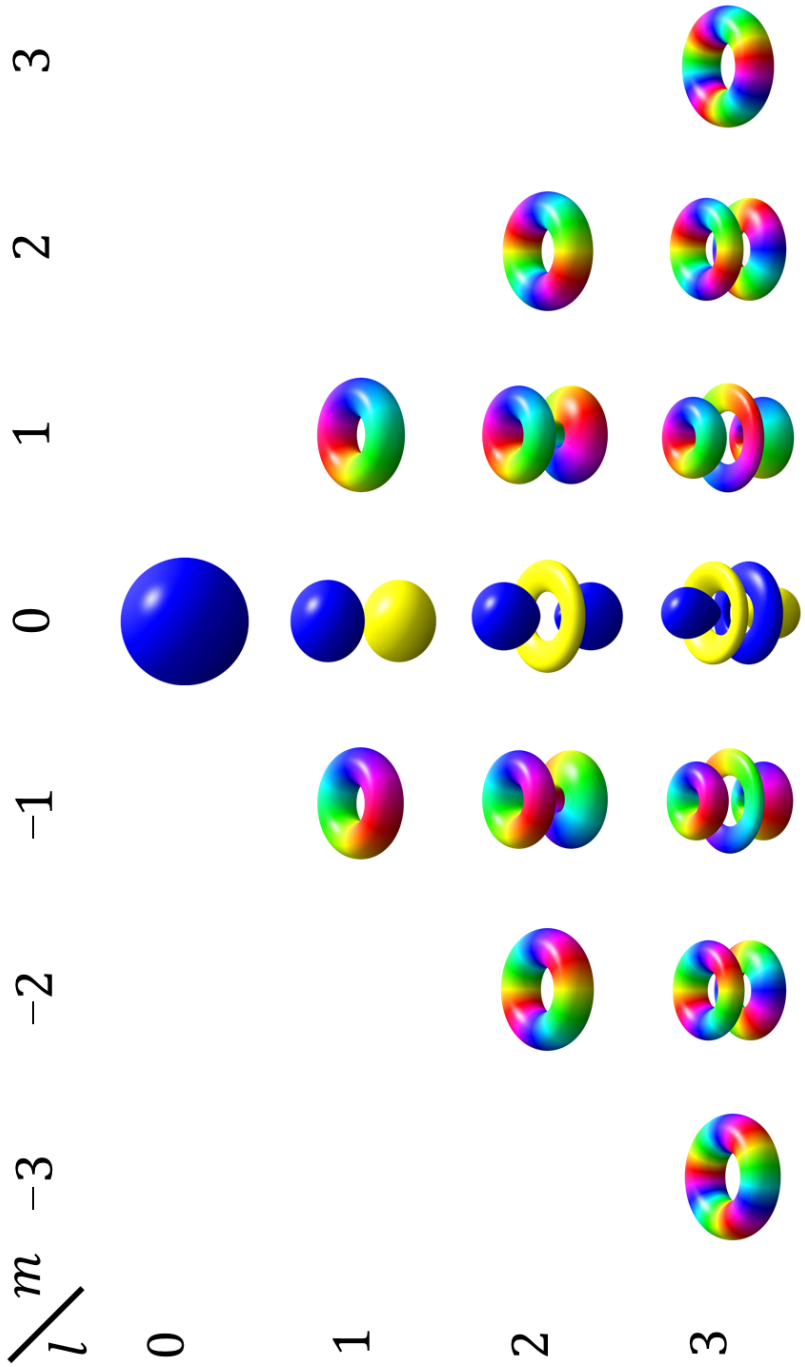

Figure 3.1: Visual representations for spherical harmonics with angular momentum quantum number $l = 0, 1, 2$, and 3 and magnetic quantum number m from $-l$ to $+l$ [78].

place if some sort of energy pumps into the atom and changes its configuration from ground state to excited state. For example, a photon can interact with an electron bound to an atom and excite it to a higher-energy state. However, the atom can only absorb photons of certain energies because the atom can only have certain energies, and this process appears discontinuous as the electron jumps from one energy level to another (therefore it is called a quantum jump). In other words, only if the photon has an energy that equals the difference between the two energy states (E_1 for the ground state and E_2 for the excited state), a photon of angular frequency, ω, is absorbed when the atom jumps between two quantized energy states, E_1 and E_2, that satisfy:

$$E_2 - E_1 = \hbar\omega \tag{3.2.1}$$

If an electron occupies a level higher than its ground-state level, the atom is temporarily excited. The atom in the excited state is unstable, and it eventually returns back to the ground state and a photon is emitted in the process. Figure 3.2 illustrates the atomic transitions induced by absorbing a photon.

Generally, the transition rate (or the probability of transition per unit time) between two states (i for the initial state, f for the final state) is proportional to the strength of the coupling between the initial and final states. This coupling is known as the matrix element for the transition. This transition rate can be calculated using Fermi's golden rule [79, 80], which is given by:

$$W_{i\to f} = \frac{2\pi}{\hbar}|M_{if}|^2 g(E) \tag{3.2.2}$$

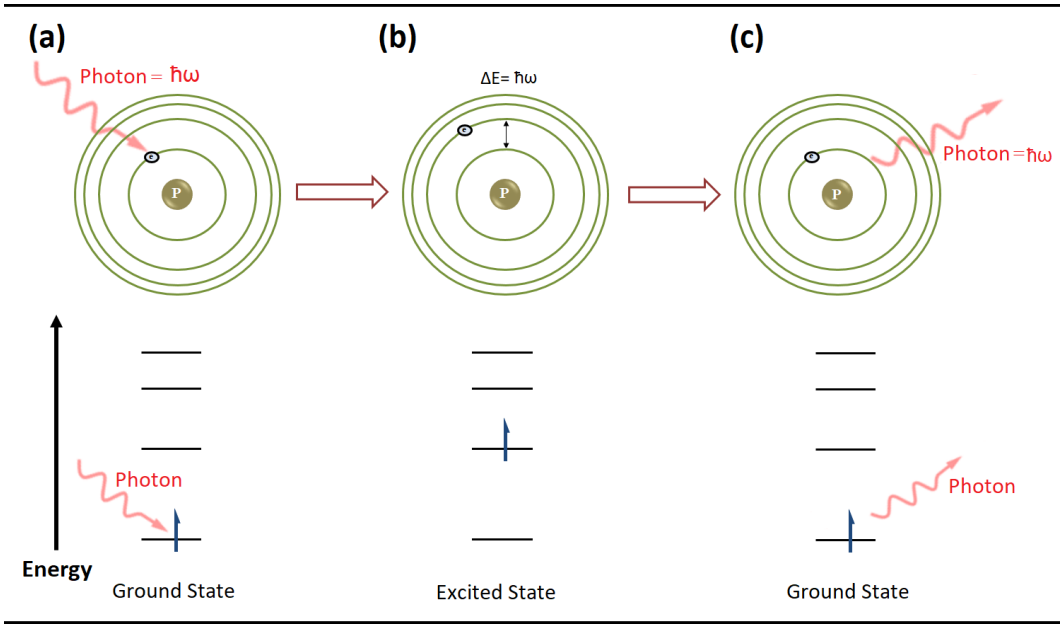

Figure 3.2: Optically induced atomic transition. (a) Photon with energy of $\hbar\omega$ is interacting with the atom. (b) The electron absorbs the photon and reaches a higher energy level because the photon has the same energy needed to reach the excited state. (c) Photon with energy of $\hbar\omega$ is emitted when the electron relaxes to ground level.

where M_{if} is the matrix element and $g(E)$ is the density of states. The density of states defines the actual occupancy of electrons in the initial state or the available in the final state. Moreover, the matrix element can be written as an integral where the interaction that causes the transition is expressed as a perturbation caused by the light, H, which operates on the wavefunction of the initial state as follows:

$$M_{if} = \langle f|H|i\rangle = \int \psi_f^*(r)H(r)\psi_i(r)d^3r \tag{3.2.3}$$

where $\psi_i(r)$ is the wavefunction of the initial state and $\psi_f(r)$ is the wavefunction of the final state [71].

A semiclassical picture of light-atom interaction is appropriate to use here. In this approach, the atoms are described quantum-mechanically while the light is treated classically. In an electric dipole transition, the perturbation, H, to the atom is produced by the interaction between the light electric field, $\mathcal{E}_0$, and the atom electric dipole, P, which gives:

$$H = -\mathbf{P}.\boldsymbol{\mathcal{E}_0} \tag{3.2.4}$$

where P is defined as:

$$\mathbf{P} = \sum_i q_i \mathbf{r_i} \tag{3.2.5}$$

where q_i is the charge at position $\mathbf{r_i}$ with respect to the origin centered at the nucleus. In the case of a single-electron atom, P is given by:

$$\mathbf{P} = -e\mathbf{r} \tag{3.2.6}$$

where e is the charge of the electron and $\mathbf{r}$ is the radial position of the electron with respect to the proton. Therefore, H can be written as:

$$H = e(x\mathcal{E}_x + y\mathcal{E}_y + z\mathcal{E}_z) \tag{3.2.7}$$

where $\mathcal{E}_x$, $\mathcal{E}_y$, and $\mathcal{E}_z$ are the components of the field amplitude along the x, y, and z axis, respectively. However, since atoms are small compared to the light wavelength, the amplitude of the electric field does not change significantly over atomic dimensions. Therefore, $\mathcal{E}_x$, $\mathcal{E}_y$, and $\mathcal{E}_z$ can be considered constants, and μ_{if} can be defined as the electric dipole moment of the transition given by:

$$\mu_{if} = -e\big(\langle f|x|i\rangle\hat{x} + \langle f|y|i\rangle\hat{y} + \langle f|z|i\rangle\hat{z}\big) \tag{3.2.8}$$

The integrals in equation 3.2.3 can be written as:

$$M_{if} = -\mu_{if}.\mathcal{E}_0 \tag{3.2.9}$$

This electric-dipole matrix element can be calculated not just for hydrogen atom but also for any atoms with known wavefunctions. If the calculated matrix element is zero (or extremely small), then the electric-dipole transition rate is zero; in other words, the transition is forbidden and it does not satisfy the selection rules. The same is true if the calculated matrix element has a finite value, in which case the transition is allowed.

3.3 Selection Rules

In light-matter interaction, the photon transfers not only its energy to the atom, but also its angular momentum. Therefore, the selection rules governing transitions between electronic energy levels are based on conservation of both energy and angular momentum. The angular momentum considered in the selection rules is the one associated with circularly polarized light (with SAM). Each photon can have SAM of $+\hbar$ for left-handed or $-\hbar$ for right-handed circularly polarized light. However, the linear momentum of photons is usually neglected in their interaction with matter [81]. This can be understood using simple analysis by comparing between the photon linear momentum and the electron's. Using the relationship $\omega = ck$, and defining the photon energy as: $E = \hbar\omega$, allows us to express the energy as: $E = c\hbar k$. Then we can calculate the photon momentum, p_λ, using the relationship: $E = cp_\lambda$, which gives us the photon linear momentum in terms of the wave number: $p_\lambda = \hbar k$. Recalling that the wave number is related to the wavelength as: $k = 2\pi/\lambda$, the photon momentum can be given by $p_\lambda = h/\lambda$, which is in the order of 10^{-28} Kg m/s. On the other hand, the electron momentum can be calculated using the lattice constant a (for example, for GaAs $a = 5.65\mathring{A}$), which is related to the wave number by: $k = \pi/a$. Therefore, we can calculate the electron momentum using the relation: $p_e = \hbar\pi/a$, and the resultant momentum is in the order of 10^{-24} Kg m/s, which indicate that the light field changes only very little within the crystal and therefore can be neglected.

The selection rules for electric-dipole transitions of a single electron in a hydrogen-like atom are shown in Table 3.1. Assuming that the initial-state

wavefunction is defined with the quantum numbers n, l, m, and m_s, and that the final-state wavefunction is defined with the quantum numbers: n', l', m', and m'_s, the selection rules obtained are:

- Since the electric-dipole operator is proportional to r (an odd function) and Legendre polynomials have definite parity (either odd or even), the parity must change.
- Since the spherical harmonic functions have parity $(-1)^l$, l must differ from l' by ± 1, and when it does not change (*i.e.* $\Delta l = 0$), the transition is forbidden.
- Since circularly polarized photons carry angular momenta of $+\hbar$ or $-\hbar$ along the z-axis, m must differ from m' by ± 1 (*i.e.* one unit of $\hbar$) to conserve angular momentum; for linearly polarized light along the z-axis, the photons carry no z-component of momentum and therefore the quantum number, m, does not change: in this case $m = m'$ (*i.e.* $\Delta m = 0$).
- Since the photon does not interact with the electron spin, the spin quantum numbers should not change in the transition, and $m_s = m'_s$ (*i.e.* $\Delta m_s = 0$).

The OAM of light has a history predating Allen *et al.* While most atomic transitions are dipolar, there are some higher-order transitions (for example, quadrupole transitions) where the emitted photon carries angular momentum of multiple units of $\hbar$ [82]. Chapter 4 will discus in detail the theory of optical transitions induced by light that carries OAM and the possibility of activating transitions with an angular momentum change larger than one unit of $\hbar$. How-

Quantum number	Selection rule	Polarization
l	$\Delta l = \pm 1$	
m	$\Delta m = +1$	Circular: left-handed (+)
	$\Delta m = -1$	Circular: right-handed (−)
	$\Delta m = 0$	Linear ∥ z
s	$\Delta m_s = 0$	

Table 3.1: Electric-dipole selection rules. The direction of the applied electromagnetic field is defined by the z-axis. The circular polarization sign is for absorption, and it is reversed for emission.

ever, we will first discuss the electronic structure and the optical properties of the nanostructures that we use to study this theory.

3.4 Semiconductor Quantum Dots

Quantum dots (QDs) are semiconductor nanoparticles usually made up of group IV atoms (such as C, Si and Ge) or a combination of groups II to VI (*e.g.* CdSe, CdTe and ZnS), III to V (*e.g.* GaP, GaAs and InN), or IV to VI (*e.g.* PbSe, PbS and SnTe). Their size is typically on the order of several nanometers in diameter. On such a scale, the electrons and holes are confined in all three spatial dimensions and known as zero-dimensional nanostructures, or artificial atoms [83]. The electronic structure and optical properties of QDs can be modified by varying the size of the particle (which can be controlled during fabrication), which can help to exploit valuable properties, particularly the size-dependent band gap. This gives rise to numerous interesting opportunities for device applications, such as solar cells [84–86], transistors [87–89], and optoelectronic devices [90–92].

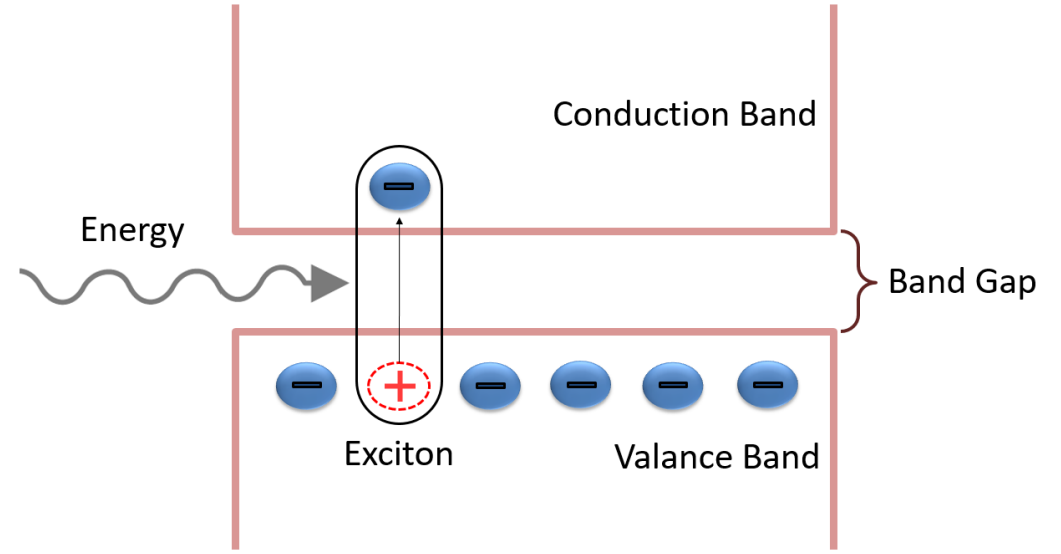

Figure 3.3: When an electron is excited from the valance band to the conduction band, leaving a hole in the valance band, a bound state of the pair (an exciton) is created.

3.4.1 Electronic Structure

Semiconductors, as the term suggests, are materials with conductivity in between that of a conductor and an insulator. The electronic structures associated with such materials are organized in bands: the valence band is a collection of the electron occupied individual orbitals, and the conduction band is a collection of the unoccupied levels. Semiconductors also have a small but non-zero band gap that defines the minimum energy required to excite an electron from the valence band to the conduction band [93].

When an electron is excited to the conduction band by applying some external energy (such as heat or photons), a hole with a positive charge is generated at the valence band. The properties of the hole are similar to those of an electron but with positive charge, and both are considered charge car-

riers. Also, a bound state of an electron-hole pair (bound by Coloumb force attraction) can be formed, known as an exciton (Figure 3.3). This bound state can be treated as a hydrogen-like atom, so the interaction between them can be described by a similar Hamiltonian [94]:

$$\hat{H} = -\frac{\hbar^2}{2M}\nabla_e^2 - \frac{\hbar^2}{2\mu}\nabla_h^2 - \frac{e^2}{\epsilon|r_e - r_h|} \tag{3.4.1}$$

where M is the total mass and μ is the reduced mass given by:

$$M = m_e^* + m_h^*$$

$$\mu = \frac{m_e^* m_h^*}{(m_e^* + m_h^*)}$$

where m_e^* and m_h^* are the effective masses of the electron and hole, respectively. The effective mass is the mass that a electron seems to have when responding to forces, since the movement of particles in the solid state is different from their motion in a vacuum. The effective mass approximation allows us to treat electron motion through a solid as a particle with definite position and momentum.

In excitons, the distance between the electron and the hole is known as the Bohr radius of the exciton, and it is usually a few nanometers. It can be calculated for a particular material system by solving the Hamiltonian in a similar way as we do with a hydrogen atom, but it would differ from a hydrogen atom because of the difference in the effective mass of the electron

Group	Compound	E_g (eV)	m_e^*/m_0	m_h^*/m_0	a_{ex} (nm)	Reference
II-VI	CdS	2.43	0.25	0.6	5.8	[96]
	CdSe	2.87	0.12	0.9	5.3	[97]
	CdTe	1.5	0.09	0.8	7.3	[98]
III-VI	InP	1.35	0.073	0.45	15	[99]
	InAs	0.354	0.023	0.57	34	[100]
	InSb	0.17	0.012	0.44	65.6	[101]
IV-VI	PbS	0.42	0.087	0.083	21	[102]
	PbSe	0.28	0.047	0.041	55	[103]
	PbTe	0.32	0.034	0.032	104	[104]

Table 3.2: Bulk band gap (E_g) at 300 K and material properties for various semiconductors.

and hole, and it is given by:

$$a_{ex} = a_0 \epsilon \frac{m_0}{\mu} \tag{3.4.2}$$

where the Bohr radius of a hydrogen atom $a_0 = 053\mathring{A}$, and m_0 is the free electron mass [95]. Table 3.2 lists characteristic material properties and Bohr radii for the excitons of some semiconductors.

If the size of a semiconductor becomes comparable to or smaller than the exciton radius, then quantum confinement arises and the properties get altered [44]. For example, table 3.4.1 shows the exciton radius for some materials, and materials with larger exciton radius are more likely to be in strong confinement regime. Depending on the dimension of the confinement, there are three kinds of confined nanostructure: quantum well (two dimensions or 2D), quantum wire (1D), and quantum dot (0D). In the confined direction, carriers cannot propagate freely whereas in other directions the carriers can have effectively infinite extent [105]. For example, in a quantum well, the material size

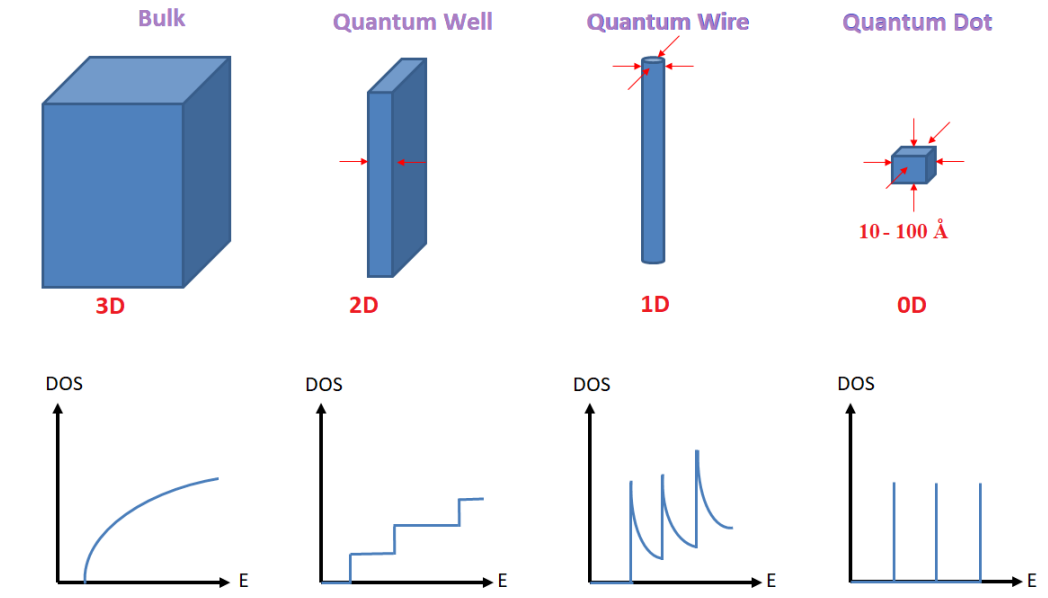

Figure 3.4: Reduction of the dimensionality of a semiconductor system from bulk (3D) to quantum dot (0D) and the corresponding electronic density of states for each system.

is restricted in one dimension and the charge carriers can extend in the other two directions without limit. Similarly in a QD, the material size is reduced in all directions, and the charge carriers cannot propagate freely in any direction. Because of these confinements, the electronic density of states changes drastically between systems of different dimensionalities [106] (see Figure 3.4).

Exciton confinement in a QD can be seen as a particle in a box system because the charge carriers cannot leave the particle of the semiconductor because of a strong potential well. In a one-dimensional system, a box with a length of L has zero potential energy inside the box while the wall has an infinitely large potential energy. This infinitely large force prevents the particle from escaping the box. By solving the Schrödinger equation for the system,

we can find the eigenenergies as a function of the charge carrier effective mass (m^*) and the box length (L):

$$E_n = \frac{n^2\hbar^2\pi^2}{2m^*L^2} = \frac{n^2h^2}{8m^*L^2} \tag{3.4.3}$$

However, this one-dimensional system is not the best model to represent QDs since the box is three-dimensional and spherical in shape. A more accurate model is the one developed by Brus [107], where the nanostructure is a sphere with radius R, the interior has a zero potential energy, and the potential energy outside the nanostructure is infinite such that the surface of the nanostructure defines the walls of the box. Using the exciton Hamiltonian 3.4.1 and solving the Schrödinger equation numerically to get the eigenenergies of QDs, we have:

$$\Delta E = E_{gap} + \frac{h^2}{8R^2}[\frac{n_e^2}{m_e^*} + \frac{n_h^2}{m_h^*}] \tag{3.4.4}$$

where E_{gap} is the energy of the band gap of the semiconductor, n_e and n_h is the principal quantum numbers for the electron and the hole respectively (where for the lowest energy level $n_e = n_h = 1$). From the previous equation, we can see that the energy is inversely proportional to the QD size.

3.4.2 Optical Properties

Although excitons can be treated as hydrogen-like atoms, unlike atoms, the excitons have a finite lifetime. After a certain time (usually on the order of nanoseconds depends on the strength of the exciton binding energy) the electron and hole recombine (exciton recombination) and emit a photon [108]. This procedure of photoexcitation, relaxation, recombination of the hole and

electron, and emission of the photon is known as photoluminescence. The photoluminescence spectrum can be obtained by measuring the number of emitted photons as a function of energy. Moreover, the frequency range of emitted light can be determined by the band gap in a QD [109]. Therefore, the photon frequency is also inversely proportional to the QD size: as the size of the QD decreases, the emitted photon frequency increases. Hence, varying the QD size can cause emission of different colors even when the QDs are made from the same material [110]. In other words, both absorption and photoluminescence can be modified by varying the QD size during synthesis. Figure 3.5 shows CdSe/ZnS QDs with different sizes excited at 350 nm and the measured fluorescence emission spectra [111].

3.4.3 Colloidal PbS QD Synthesis

Lead sulfide (PbS) was one of the earliest materials to be used as a semiconductor [112]. Colloidal PbS QDs are inexpensive to make and easy to maintain at room temperature. The samples used in this study were synthesized by a method similar to that described by Hines and Scholes [113]. In a typical fabrication, a mixture of lead oxide (PbO) and oleic acid (OA) dissolved in octadecene (ODE) would be heated at $120°C$ for two hours (decreasing the amount of OA decreases the QD size). Then ODE and bis (trimethylsilyl) sulfide (TMS) solution (TMS/ODE) is rapidly injected into the Pb precursor mixture at $135°C$ (increasing the injection temperature decreases the QD size). The rapid injection of TMS/ODE solution into the Pb precursor mixture changes the color of the mixture from clear to dark brown. The reaction would be stopped after 20 to 30 seconds by removing the mixture from heat

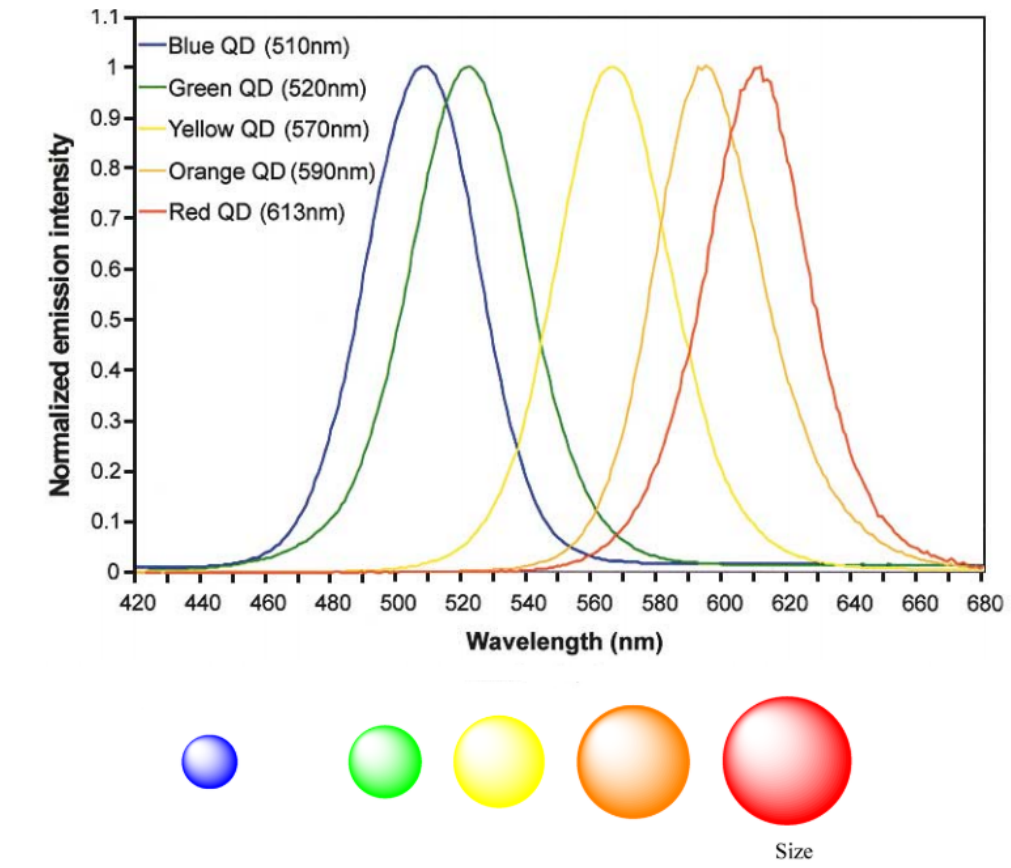

Figure 3.5: Size-dependent photoluminescence spectra of CdSe/ZnS QDs [111]. The width of the peaks indicates structural homogeneity; narrower the peak indicates higher uniformity of dot size.

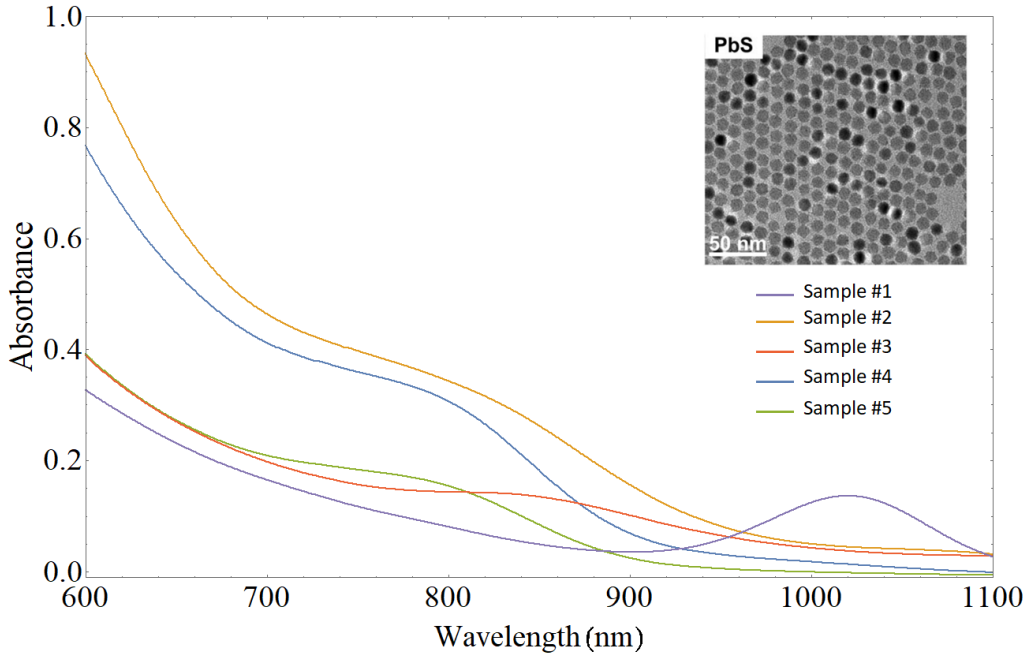

Figure 3.6: Absorption spectra for several QD samples synthesized using the same technique but with different reaction times. Inset shows a typical transmission electron microscopy image of colloidal PbS nanocrystals [95].

and placing it in an ice-water bath; increasing the reaction time results in larger QDs. Finally, the QDs are isolated by precipitating with distilled acetone, centrifuging, and then dissolving the mixture in toluene. This process is usually repeated 2 or 3 times, and after that the QDs can be dissolved in a minimal amount of toluene. Figure 3.6 shows the absorption spectrum for some QD samples made by Geoff Diederich (with different sizes) that were synthesized by this method.

3.5 Conclusion

In this chapter, we presented the fundamentals of light-matter interaction, explaining atomic structure, the mechanism of optically induced atomic transition, and selection rules governing transitions between electronic energy states. We also discussed the electronic structure and optical properties of the semiconductor QDs. Finally, we briefly explained how the colloidal PbS QDs used in this study were synthesized. In the following chapter, we explore the theory of electronic transitions induced by twisted light in semiconductor QDs and the corresponding changes in the selection rules.

Chapter 4

Twisted Light and Matter

To untangle the relative roles of orbital angular momentum and spin angular momentum, few experiments have already explored the angular momentum exchange between light and matter [114, 115]. While twisted light has been used in tools such as optical tweezers that can rotate microscopic objects [48, 116], it has not been clear whether this additional angular momentum could make any changes to the atomic state of bound electrons. This subject has been debated over the past two decades [117–130], and first experiments [131–133] have not observed transfer of OAM. Recent spectroscopic experiments investigated the interaction of matter with twisted light and demonstrated the transfer of OAM to the valence electron of a trapped ion [134], although another atomic spectroscopy experiment showed that the light's OAM does not affect the electric dipole transition, which appears insensitive to the OAM [135]. While a single trapped ion was used in the first experiment to detect the transfer of OAM, an ensemble of atoms were used in the second one. However, in the latter experiment, rubidium vapors were used, and

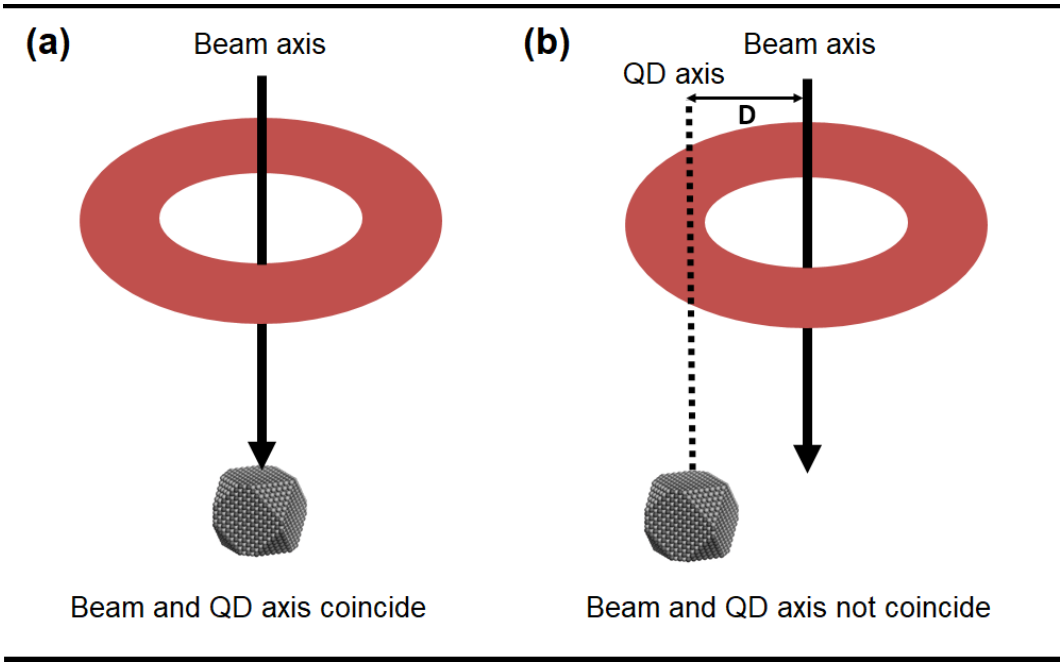

Figure 4.1: (a) Axis of the twisted light beam and the quantum dots coincide. (b) Quantum dot axis is displaced with respect to the twisted light beam axis which can be expressed as superposition of centered beams with different values of OAM.

to date no one has investigated the effect of a photon's OAM on solid-state material.

In this chapter, we briefly discuss the theory of optical electronic transition induced by light that carries OAM in semiconductor QDs and the corresponding selection rule. Then we review the extended theory of a more realistic case of the interaction of a twisted beam with QDs when the symmetry axis of the beam and the axis of the nanostructure do not coincide. This is important because it represents true experimental situations in which each nanostructure sees a light beam that is displaced by a different distance relative to itself [136]. Figure 4.1 compares cases in which the beam and the QD axes do and do not coincide.

It is well known that in semiconductor nanostructures, transitions between different electronic states can be induced optically. This optical response has been investigated extensively for its valuable applications in solar cells, quantum computing, and other areas. While plane waves or Gaussian laser beams have mostly been used to excite QDs, little work has been done investigating the interaction of twisted light with these nanostructures. Because the transfer of spin angular momentum from photons to material is essential to light-matter interaction [137,138], we investigate the effect of light OAM when interacting with QDs.

4.1 Coincident Beam and QD Axes

First we derive the electronic transitions induced by light with OAM in semiconductor QDs and the corresponding selection rule when the axes of the light beam and nanostructures coincide. Twisted light carries an OAM of $\hbar\ell$ per photon, and the field has a phase of $exp(i\ell\theta)$. Such a beam can be described, for example, as a Laguerre-Gaussian or Bessel beam. For the Laguerre-Gaussian modes, the the time-independent part of the electric field can be written as:

$$F(\mathbf{r}) = \left[\frac{C_p^{|\ell|}}{w_0}\left(\frac{r\sqrt{2}}{w_0}\right)^{|\ell|} e^{-\frac{r^2}{w_0^2}} L_p^{|\ell|}\left(\frac{2r^2}{w_0^2}\right)\right] e^{-i\ell\theta} = J_{p,\ell}(r)e^{-i\ell\theta} \tag{4.1.1}$$

where w_0 is the beam waist, r is the radial position ($r = \sqrt{x^2+y^2}$), $L_p^{|\ell|}$ is the Laguerre polynomial, and $C_p^{|\ell|}$ is the normalization constant.

Mathematically, a Bessel mode is one of the most convenient ways to describe twisted light. However, Bessel mode cannot be generated as it is unbounded and would require an infinite amount of energy. For this propagation-invariant beam, also called a "nondiffracting" beam, paraxial approximation is not needed (as it is for Laguerre-Gaussian), and it is a solution of the Helmholtz equation in cylindrical coordinates given by [139, 140]:

$$F_\ell(\mathbf{r}) = J_\ell(k_\perp r)e^{i\ell\theta} \tag{4.1.2}$$

where $J_\ell(k_r r)$ is an ℓth-order Bessel function of the first kind, and $k_\perp$ is the magnitude of the wave vector perpendicular to the direction of propagation (which defines the waist of the beam, $\frac{1}{k_\perp} \simeq w_o$). The wavelength, λ, and the frequency, ω, are related to the wave vector parallel (k_z) and perpendicular ($k_\perp$) components as [141]:

$$\lambda = \frac{2\pi}{\sqrt{k_z^2 + k_\perp^2}}$$

$$\omega = c\sqrt{k_z^2 + k_\perp^2}$$

For $k_\perp = 0$ the beam mode reduces to a plane wave propagating in the z direction.

In the Coulomb gauge (also known as the transverse gauge), the vector potential has both longitudinal and transverse components. However, under typical experimental conditions, the transverse component is the dominant one, *i.e.*, $k_z \gg k_\perp$. Therefore, the vector potential for a Bessel beam traveling

in the z direction would be [142]:

$$\mathbf{A}_\ell(\mathbf{r},t) = \epsilon_\sigma F_\ell(\mathbf{r}) e^{i(k_z z - \omega t)} + c.c$$

$$\mathbf{A}_\ell(\mathbf{r},t) = \mathbf{A}_\ell^{(+)}(\mathbf{r},t) + \mathbf{A}_\ell^{(-)}(\mathbf{r},t) \tag{4.1.3}$$

where $\epsilon_\sigma = (\hat{x} + i\sigma\hat{y})/\sqrt{2}$ with $\sigma = \pm 1$ being the polarization vector for circular polarization [119].

On the other hand, the electronic states in semiconductor nanostructures can be defined by the product of an envelope function, $\Phi(r,\theta)Z(z)$, a microscopic cell-periodic function, $u_b(r)$, and a spin part, ζ:

$$\psi_b(\mathbf{r}) = [\Phi(r,\theta)Z(z)]u_b(\mathbf{r})\zeta \tag{4.1.4}$$

where b is the index for the band (for example, the conduction or valence band). We also assume that the envelope function, $\Phi(r,\theta)Z(z)$, is separable into the vertical (z) and in-plane (r,θ) motions. We chose cylindrical coordinate because the geometry of the incoming beam set an axis that makes the structure sees a cylindrical symmetry (which makes sense to use cylindrical bases). Also, for the first order approximation we can assume that there is no z-dependence since this shows the essential OAM-interaction. The solution for the corresponding electron was derived by Fock [143] and Darwin [144] and later calculated in more detail by Dingle [145]. Thus the eigenfunction is given by:

$$\Phi_{nm}(r,\theta) = R_{nm}(r,\theta)e^{i\theta m} \tag{4.1.5}$$

where:

$$R_{nm}(r,\theta) = \frac{(-1)^n}{\sqrt{2\pi}\iota}\sqrt{\frac{n!}{(n+|m|)!}}e^{\frac{-r^2}{4\iota^2}}(\frac{r}{\sqrt{2}\iota})^{|m|}L_n^{|m|}(\frac{r^2}{2\iota^2}) \tag{4.1.6}$$

and ι is a characteristic confinement length for electrons, n is the radial quantum number (which defines the number of nodes in the radial wavefunction), m is the angular momentum quantum number, and $L_n^{|m|}(x)$ is the Laguerre polynomial [146].

To determine the optical response, the transition matrix elements induced by the light-matter Hamiltonian between single-particle states need to be calculated from:

$$H_\ell = -\frac{1}{2m_e^*}(\mathbf{p} - q\mathbf{A}_\ell(\mathbf{r},t))^2 \tag{4.1.7}$$

where $q = -e$ (the charge of the electron), and p is the momentum of the electron ($p = -i\hbar\nabla$). However, we need to use the minimal-coupling interaction for only the lowest order of the vector potential, which is given by:

$$H_\ell = -\frac{q}{m_e^*}\mathbf{A}_\ell(r,t).\mathbf{p} \tag{4.1.8}$$

The physics of the interaction is obtained from the matrix element of H_ℓ, which, for light absorption $v \to c$, is given by:

$$\langle c\alpha'|H_\ell^{(+)}|v\alpha\rangle = -\frac{q}{m_e^*}\langle\psi_{c\alpha'}|\mathbf{A}_\ell(\mathbf{r},t).\mathbf{p}|\psi_{v\alpha}\rangle \tag{4.1.9}$$

$$\langle c\alpha'|H_\ell^{(+)}|v\alpha\rangle = i\hbar\frac{q}{m_e^*}\int\psi_{c\alpha'}^*(\mathbf{r})\mathbf{A}_\ell(\mathbf{r},t).\nabla\psi_{v\alpha}(\mathbf{r})d^3r \tag{4.1.10}$$

where α is a collective index that includes all quantum numbers used to sim-

plify the notation. It also contains the angular quantum number, m, that appears in equation 4.1.6 ($e^{im\theta}$). By substituting the value of ψ from equation 4.1.4 into the previous equation and using the relationship, $\nabla.(\mathbf{AB}) = (\nabla\mathbf{A}).\mathbf{B} + \mathbf{A}(\nabla.\mathbf{B})$, we obtain:

$$\langle c\alpha'|H_\ell^{(+)}|v\alpha\rangle = i\hbar\frac{q}{m_e^*}\Bigg[\int \Phi_{c\alpha}^*(\mathbf{r})Z^*(z)u_c^*(\mathbf{r})\zeta^*$$

$$\times\mathbf{A}_\ell(\mathbf{r},t).\Big[\nabla\Phi_{v\alpha}(\mathbf{r})Z(z)u_v(\mathbf{r}) + \Phi_{v\alpha}(\mathbf{r})\nabla Z(z)u_v(\mathbf{r}) + \Phi_{v\alpha}(\mathbf{r})Z(z)\nabla u_v(\mathbf{r})\Big]\zeta d^3r\Bigg] \tag{4.1.11}$$

Applying the dot product and arranging the equation gives:

$$\langle c\alpha'|H_\ell^{(+)}|v\alpha\rangle = i\hbar\frac{q}{m_e^*}\int u_c^*(\mathbf{r})u_v(\mathbf{r})\mathbf{A}_\ell(\mathbf{r},t).[\Phi_{c\alpha}^*(\mathbf{r})\nabla\Phi_{v\alpha}(\mathbf{r})]|Z(z)|^2\zeta^*\zeta d^3r$$

$$+i\hbar\frac{q}{m_e^*}\int \Phi_{c\alpha}^*(\mathbf{r})\Phi_{v\alpha}(\mathbf{r})u_c^*(\mathbf{r})u_v(\mathbf{r})\mathbf{A}_\ell(\mathbf{r},t).[Z^*(z)\nabla Z(z)]\zeta^*\zeta d^3r$$

$$+i\hbar\frac{q}{m_e^*}\int \Phi_{c\alpha}^*(\mathbf{r})\Phi_{v\alpha}(\mathbf{r})\mathbf{A}_\ell(\mathbf{r},t).[u_c^*(\mathbf{r})\nabla u_v(\mathbf{r})]|Z(z)|^2\zeta^*\zeta d^3r \tag{4.1.12}$$

Because we are investigating optical transitions, we may focus our attention on the interband transitions, where $c \neq v$. Also, as a result of the orthogonality of the microscopic function in a cell ($\int u_c^*(\mathbf{r})u_v(\mathbf{r})d^3r = \delta_{c.v}$), only the final term in the previous equation is not zero for interband transitions, which gives:

$$\langle c\alpha'|H_\ell^{(+)}|v\alpha\rangle = i\hbar\frac{q}{m_e^*}\int \Phi_{c\alpha}^*(\mathbf{r})\Phi_{v\alpha}(\mathbf{r})\mathbf{A}_\ell(\mathbf{r},t).[u_c^*(\mathbf{r})\nabla u_v(\mathbf{r})]|Z(z)|^2\zeta^*\zeta d^3r \tag{4.1.13}$$

In addition, in a unit cell (with a lattice constant, a), the envelope function and the vector potential can be considered constant because they are varying

slowly, and the microscopic function, $u(\mathbf{r})$, is considered periodic over unit cells. Therefore, we can separate the integral into an intracell integral and an intercell sum [81], which gives:

$$\langle c\alpha'|H_\ell^{(+)}|v\alpha\rangle = \frac{-q}{m_e^*}\left[\int u_c^*(\mathbf{r})(-i\hbar\nabla)u_v(\mathbf{r})\zeta^*\zeta d^3r\right]$$

$$.\left[\sum_i \Phi_{c\alpha}^*(\mathbf{r_i})\Phi_{v\alpha}(\mathbf{r_i})|Z(z_i)|^2\mathbf{A}_\ell(\mathbf{r_i},\mathbf{t})\right] \tag{4.1.14}$$

Taking the continuum limit transforms the sum over cells ($\sum$) to an intercell integral ($\frac{1}{a^3}\int$). Also, by defining the matrix element, $a^3\mathbf{p}_{cv} = \int_0^{a^3} u_c^*(r)$ $(-i\hbar\nabla)u_v(r)d^3r$, substituting the positive part of the vector potential, $\mathbf{A}_\ell^{(+)}(\mathbf{r},t)$, (which corresponds to light absorption) from equation 4.1.3, and finally assuming that the optical wavelength is much larger than the nanostructure diameter (so that $e^{ikz} \simeq 1$), we get:

$$\langle c\alpha'|H_\ell^{(+)}|v\alpha\rangle = \frac{-q}{m_e^*}e^{-i\omega t}(\epsilon_\sigma.\mathbf{p}_{cv})\int e^{-i\ell\theta}e^{im\theta}e^{-im'\theta}d^3r\int\zeta'\zeta d^3r$$

$$\int J_\ell(r)R_{c\alpha'}^*(r)R_{v\alpha}(r)d^3r\int|Z(z)|^2d^3r \tag{4.1.15}$$

where d^3r in cylindrical coordinate is given by $d\theta dzrdr$. Also, due to the orthogonality of the spin function, ζ, the exponential function, and the vertical part of the envelop function, $Z(z)$, the integrals in the final equation can be reduced to:

$$\int_0^\infty \zeta'\zeta d^3r = \delta\zeta', \zeta$$

$$\int_{\pi}^{-\pi} e^{-i\ell\theta} e^{-i(m'-m)\theta} d\theta = 2\pi\delta_{l,(m'-m)}$$

$$\int_0^{\infty} |Z(z)|^2 dz = 1$$

Then, the matrix element can be written as:

$$\langle c\alpha'|H_\ell^{(+)}|v\alpha\rangle = \frac{-2\pi q}{m_e^*} e^{-i\omega t}(\epsilon_\sigma . \mathbf{p}_{cv})\delta_{l,(m'-m)}\delta\zeta', \zeta \int_0^{\infty} J_\ell(r) R^*_{c\alpha'}(r) R_{v\alpha}(r) r dr \tag{4.1.16}$$

The same can be done for emission ($c \to v$) of light: by using $\mathbf{A}_\ell^{(-)}(\mathbf{r}, t)$, the matrix element of the light-matter interaction is given by [147]:

$$\langle v\alpha'|H_\ell^{(-)}|c\alpha\rangle = \frac{-2\pi q}{m_e^*} e^{-i\omega t}({\epsilon_\sigma}^* . \mathbf{p}_{vc})\delta_{\ell,(m-m')}\delta\zeta', \zeta \int_0^{\infty} J_\ell(r) R^*_{v\alpha'}(r) R_{c\alpha}(r) r dr \tag{4.1.17}$$

The selection rule for the conservation of the z projection of the orbital angular momentum of the electron and the light appears in the past two equations, where ℓ corresponds to the light OAM and m is the z component of the electron's orbital angular momentum. The delta functions that appear in equations 4.1.16 and 4.1.17 indicates that, the only allowed transitions are when $m' - m = \ell$ for absorption, and $m - m' = \ell$ for emission. In other words the only allowed transitions are the one connecting the states m and m' that differ by ℓ.

More simplification and analysis can be achieved by applying specific $J_\ell(r)$ functions (using either Bessel mode or Laguerre-Gaussian mode) and the radial functions, $R_{v\alpha}(r)$ and $R_{c\alpha'}(r)$.

4.1.1 Analysis

To study twisted-light-induced optical transitions we first need to specify the initial and final states for the transition. We use equation 4.1.6 for both the valance and conduction bands ($R_{vnm}(r)$ and $R_{cn'm'}(r)$) Furthermore, by transforming coordinates to $x = r^2/(2\iota^2)$, the radial functions for valance and conduction bands are given by:

$$R_{nm}(r) = \frac{(-1)^n}{\sqrt{2\pi}\iota}\sqrt{\frac{n!}{(n+|m|)!}}e^{-x/2}L_n^{|m|}(x)x^{|m|/2} \tag{4.1.18}$$

$$R_{n'm'}(r) = \frac{(-1)^{n'}}{\sqrt{2\pi}\iota}\sqrt{\frac{n'!}{(n'+|m'|)!}}e^{-x/2}L_{n'}^{|m'|}(x)x^{|m'|/2} \tag{4.1.19}$$

We also need to define the beam parameters, for example, ℓ for a Bessel beam or p, ℓ for a Laguerre-Gaussian beam. We use the Laguerre-Gaussian mode from equation 4.1.1, $J_{p,\ell}(r)$, because the Laguerre polynomials that appear in the radial function allow more simplification based on their orthogonality. By defining $w_0 = 4\iota^2/\beta$ and transforming coordinates to $x = r^2/(2\iota^2)$, we get:

$$J_{p,\ell}(r) = \frac{C_p^{|\ell|}}{w_0}\big(\beta x\big)^{|\ell|/2}e^{-x\beta/2}L_p^{|\ell|}\big(\beta x\big) \tag{4.1.20}$$

Once we define the radial functions and choose the twisted beam mode, we can then insert these expressions in equation 4.1.16, which gives:

$$\langle c\alpha'|H_\ell^{(+)}|v\alpha\rangle = \frac{-q}{m_e^*}e^{-i\omega t}(\epsilon_\sigma.\mathbf{p}_{cv})\delta_{\ell,(m'-m)}\delta\zeta',\zeta\frac{C_p^{|\ell|}}{w_0}(-1)^{n+n'}\beta^{|\ell|/2}$$

$$\times\sqrt{\frac{n!n'!}{(n+|m|)!(n'+m')!}}\int_0^\infty e^{-x(1+\beta/2)}L_p^{|\ell|}(\beta x)L_n^{|m|}(x)L_{n'}^{|m'|}(x)x^{(|m'|+|m|+|\ell|)/2}dx \tag{4.1.21}$$

When considering a QD in its ground state, all electrons will be in the valence band, and an electron's transition rate from the valence band to the conduction band can be found by applying the electron radial wavefunction in its initial state, $R_{00}(r)$, and final state, $R_{n',m'}(r)$, in equation 4.1.21, where $L_0^\ell(x) = 1$:

$$\langle c\alpha'|H_\ell^{(+)}|v\alpha\rangle = \frac{-q}{m_e^*}e^{-i\omega t}(\epsilon_\sigma.\mathbf{p}_{cv})\delta_{\ell,m'}\delta\zeta',\zeta\frac{C_p^{|\ell|}}{w_0}(-1)^{n'}\beta^{|\ell|/2}\sqrt{\frac{n'!}{(n'+|m'|)!}}$$

$$\times\int_0^\infty e^{-x(1+\beta/2)}L_p^{|\ell|}(\beta x)L_{n'}^{|m'|}(x)x^{(|m'|+|\ell|)/2}dx \tag{4.1.22}$$

Due to the delta function $\delta_{\ell,m'}$, m' must be equal to ℓ for allowed transitions, which gives:

$$\langle c\alpha'|H_\ell^{(+)}|v\alpha\rangle = \frac{-q}{m_e^*}e^{-i\omega t}(\epsilon_\sigma.\mathbf{p}_{cv})\delta_{\ell,m'}\delta\zeta',\zeta\frac{C_p^{|\ell|}}{w_0}(-1)^{n'}\beta^{|\ell|/2}\sqrt{\frac{n'!}{(n'+|\ell|)!}}$$

$$\times\int_0^\infty e^{-x(1+\beta/2)}L_p^{|\ell|}(\beta x)L_{n'}^{|\ell|}(x)x^{|\ell|}dx \tag{4.1.23}$$

To simplify the notation, we define $f(\beta)$ as:

$$f(\beta) = \beta^{|\ell|/2}\int_0^\infty e^{-x(1+\beta/2)}L_p^{|\ell|}(\beta x)L_n^{|\ell|}(x)x^{|\ell|}dx$$

yielding:

$$\langle c\alpha'|H_\ell^{(+)}|v\alpha\rangle = \frac{-q}{m_e^*}e^{-i\omega t}(\epsilon.\mathbf{p}_{cv})\delta_{\ell,m'}\delta\zeta', \zeta\frac{C_p^{|\ell|}}{w_0}(-1)^{n'}\sqrt{\frac{n'!}{(n'+|\ell|)!}}f(\beta) \tag{4.1.24}$$

For minimum beam waist size ($\simeq$ 500 nm; depends on the wavelength) and QDs of 10 to 200 nm, β is very small and in the range of $0.001 < \beta < 0.6$ [147]. Therefore, we can neglect the higher order and need only to keep the lowest order in β.

We also can rewrite $L_p^{|\ell|}(\beta x)$ by using the relationship [148] assuming that $\ell \geq 0$:

$$L_b^a(cx) = \sum_{i=0}^{\infty}\begin{pmatrix} a+b \\ b-i \end{pmatrix} c^i(1-c)^{b-i}L_i^a(x)$$

which for small c (*i.e.*, β) can be written as:

$$L_b^a(cx) \simeq \begin{pmatrix} a+b \\ b \end{pmatrix}(1-bc)L_0^a(x) + \begin{pmatrix} a+b \\ b-1 \end{pmatrix} cL_1^a(x) \tag{4.1.25}$$

which gives:

$$L_p^\ell(\beta x) = \frac{(\ell+p)!}{p!\ell!}(1-p\beta)L_0^\ell(x) + \frac{(\ell+p)!}{(p-1)!(\ell+1)!}\beta L_1^\ell(x) \tag{4.1.26}$$

Substituting the value of $L_p^\ell(\beta x)$ in $f(\beta)$, the integral: $\int_0^\infty x^\ell e^{-x}xL_0^\ell(x)L_n^\ell(x)dx$ can be simplified by using the relationship, $x = (1+\ell)L_0^\ell(x) - L_1^\ell(x)$, and since $L_0^\ell(x) = 1$, this makes: $xL_0^\ell(x)L_n^\ell(x) = [(1+\ell)L_0^\ell(x) - L_1^\ell(x)]L_n^\ell(x)$. Therefore, $f(\beta)$ can be reduced by using the previous relationship and the

Laguerre polynomial orthogonality relationship, given by:

$$\int_0^\infty e^{-x}x^a L_b^a(x)L_c^a(x)dx = \frac{(b+a)!}{b!}\delta_{bc}$$

We get:

$$f(\beta) = \beta^{\ell/2}\frac{(\ell+p)!}{p!}\delta_{0n'} + \beta\frac{(\ell+p)!}{p!}\left(p+\frac{\ell+1}{2}\right)(\delta_{1n'}-\delta_{0n'})$$

For a plane wave, ℓ and $p=0$, so in this case $f(\beta) = \delta_{0n'} + \beta/2\delta_{1n'} - \beta/2\delta_{0n'}$, which for small β, we use the first term only. The transitions induced by twisted wave, $H_{\ell,p}$, and plane wave, $H_{0,0}$, can be found from:

$$\langle c\alpha'|H_{\ell,p}|v\alpha\rangle = \frac{-q}{m_e^*}e^{-i\omega t}(\epsilon.\mathbf{p}_{cv})\delta_{\ell,m'}\delta\zeta', \zeta\frac{C_p^\ell}{w_0}(-1)^{n'}\sqrt{\frac{n'!}{(n'+\ell)!}}\beta^{\ell/2}\frac{(\ell+p)!}{p!}\delta_{0n'} \tag{4.1.27}$$

$$\langle c\alpha'|H_{0,0}|v\alpha\rangle = \frac{-q}{m_e^*}e^{-i\omega t}(\epsilon.\mathbf{p}_{cv})\delta_{\ell,m'}\delta\zeta', \zeta\frac{C_0^0}{w_0}(-1)^{n'}\delta_{0n'} \tag{4.1.28}$$

Therefore, when comparing the transitions induced by twisted waves and plane waves, we get:

$$\frac{H_{\ell,p}}{H_{0,0}} = \frac{C_p^\ell}{C_0^0}\sqrt{\frac{n'!}{(n'+\ell)!}}\beta^{\ell/2}\frac{(\ell+p)!}{p!} \tag{4.1.29}$$

Since β depends exponentially on $\ell/2$, we can see that for small QDs (*i.e.*, small β), the higher the OAM of the light beam (*i.e.*, ℓ value), the weaker the transition becomes. Moreover, the strength of the transition induced by twisted wave (with $\ell \neq 0$) is weaker than the one induced by plane wave ($\ell = 0$).

4.2 Displaced Beam and QD Axes

When considering experimental situations, studying a twisted beam aligned to a single QD is not realistic. Instead, illuminating an ensemble of nanostructures, where each particle sees a displaced light beam, is more often the case. Therefore, we consider the case of the nanoparticle whose axis is displaced with respect to the twisted light axis. We can then use the resultant selection rules to predict the transition rate for an ensemble of QDs. This is crucial because the OAM of a light beam depends on the choice of reference axis [17].

4.2.1 Displacement of the Light Beam

Although the displacement of a twisted beam does not change its OAM, for an individual photon with respect to the initial axis, it does change the OAM state of the photon associated with the reference axis [149]. In other words, a single OAM state of an individual photon converts to a superposition of several OAM modes in a displaced frame [150].

If the light carries an OAM of zero (a Gaussian beam), it can be seen as a superposition of several OAM states in a displaced frame with some nonzero OAM states. For example, when considering a Gaussian beam with amplitude E_0 and beam waist ω_0, the spatial mode of electric field is given by:

$$E_s(x, y) = E_0 \exp \frac{-(x^2 + y^2)}{\omega_0^2} \tag{4.2.1}$$

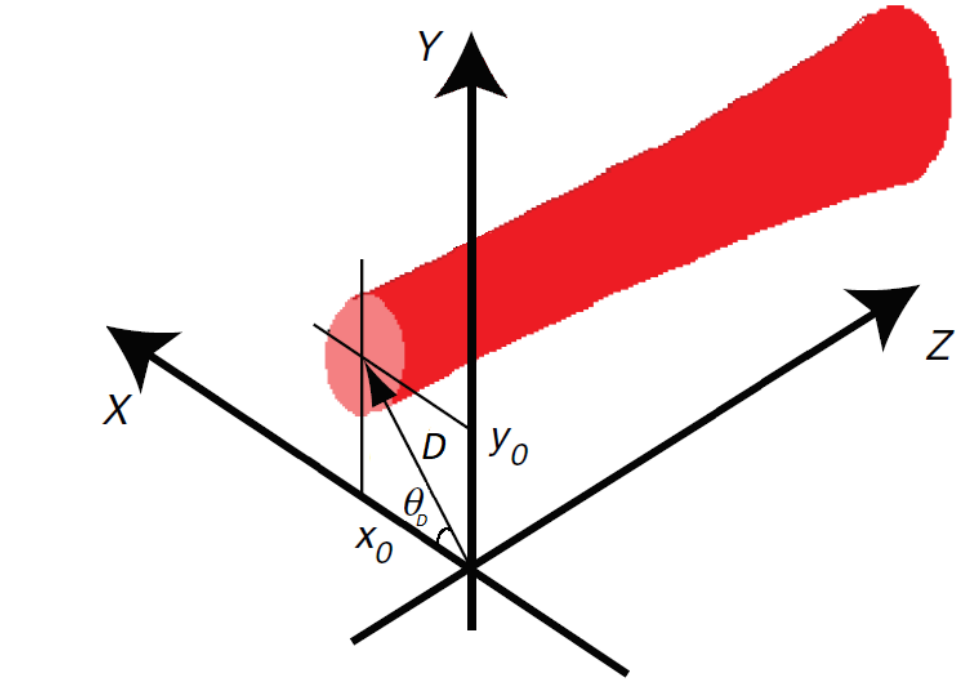

Figure 4.2: Displaced Gaussian beam with optical axis parallel to the z-axis. [151]

If the beam optical axis is originally parallel to the z-axis and displaced by x_0 and y_0 (as shown in Figure 4.2), then the displaced Gaussian beam in the coordinate frame can be written as:

$$E_s(x,y) = E_0 \exp\left(- \frac{(x-x_0)^2 + (y-y_0)^2}{\omega_0^2} \right) \tag{4.2.2}$$

where in polar coordinates, x_0 and y_0 can be written as $x_0 = D\cos\theta_D$ and $y_0 = D\sin\theta_D$. Also, transferring the Cartesian coordinates to the polar coordinates can be obtained from $x = r\cos\theta$ and $y = r\sin\theta$. In addition, using the trigonometric relationships, $\cos\alpha\cos\beta = \frac{1}{2}[\cos(\alpha-\beta) + \cos(\alpha+\beta)]$ and $\sin\alpha\sin\beta = \frac{1}{2}[\cos(\alpha-\beta) - \cos(\alpha+\beta)]$, we can simplify the electric field distribution and write it as:

$$E_s(r,\theta) = E_0 \exp\left(- \frac{r^2 + D^2}{\omega_0^2} \right) \exp\left(\frac{2rD\cos(\theta - \theta_D)}{\omega_0^2} \right) \tag{4.2.3}$$

By decomposing the second exponent, we obtain:

$$E_s(r,\theta) = E_0 \exp\left(- \frac{r^2 + D^2}{\omega_0^2} \right) \sum_{s=-\infty}^{\infty} J_s\left(\frac{2rD}{\omega_0^2} \right) \exp\left[is(\theta - \theta_D) \right] \tag{4.2.4}$$

where J_s is a Bessel function of order s [152]. The final expression shows that the displaced Gaussian beam is seen as a superposition of Bessel-Gauss beams with the azimuthal phase dependence $\exp(is\theta)$ [153], where each Bessel-Gauss mode is an alternative to Laguerre-Gaussian mode, and they can be interconverted [151].

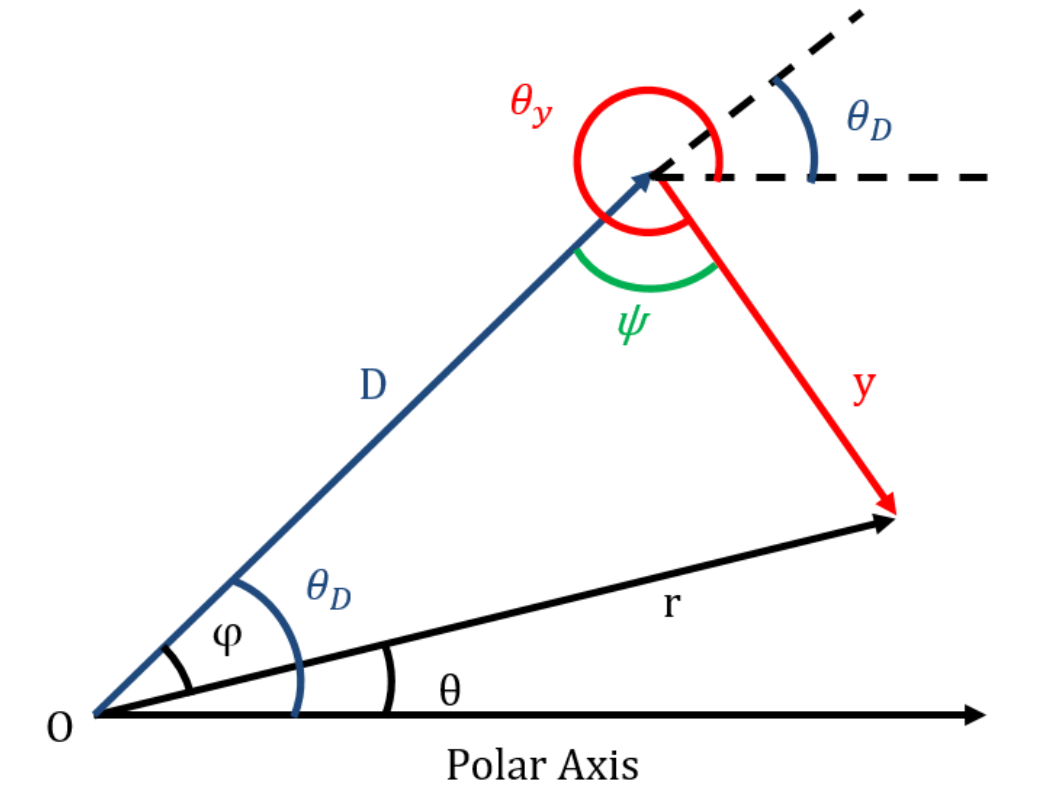

Figure 4.3: Quantum dot and twisted light relative positions. The quantum dot is placed at O and the twisted light beam is displaced by **D**.

4.2.2 QDs and Off-Center Twisted Beams

We followed the calculation presented by Quinteiro *et al* [136], starting considering a QD placed at the origin, and a twisted beam with its optical axis parallel to the z-axis at distance D, as shown in Figure 4.3. Using a Bessel beam allows additional simplification (explained below), so the Bessel mode $F_\ell(\mathbf{y})$ at **D** is defined as:

$$F_\ell(\mathbf{y}) = J_\ell(k_\perp y)e^{i\ell\theta_y} \tag{4.2.5}$$

From Figure 4.3, the angle $\theta_y = \theta_D + \psi + \pi$. Recalling that $e^{i\pi} = \cos(\pi) + i\sin(\pi) = (-1)$, the term, $e^{i\ell\theta_y}$, can be written as:

$$F_\ell(\mathbf{y}) = J_\ell(k_\perp y)(-1)^\ell e^{i\ell\psi} e^{i\ell\theta_D} \tag{4.2.6}$$

Using the properties of the Bessel function from [154], we can rewrite the term $J_\ell(k_\perp y)e^{i\ell\psi}$ as:

$$J_\ell(k_\perp \mathbf{y})e^{i\ell\psi} = \sum_{s=-\infty}^{\infty} J_{\ell+s}(k_\perp D)J_s(k_\perp r)e^{is\phi} \tag{4.2.7}$$

Substituting the value of $J_\ell(k_\perp y)e^{i\ell\psi}$ in $F_\ell(\mathbf{y})$ gives us:

$$F_\ell(\mathbf{y}) = (-1)^\ell \sum_{s=-\infty}^{\infty} J_{\ell+s}(k_\perp D)J_s(k_\perp r)e^{is(\theta_D-\theta)}e^{i\ell\theta_D}$$

where $\phi = \theta_D - \theta$. By using the relationship $J_a = (-1)^{-a}J_{-a}$ [154], we can write $F_\ell(\mathbf{y})$ as:

$$F_\ell(\mathbf{y}) = (-1)^\ell \sum_{s=-\infty}^{\infty} (-1)^{-s} J_{\ell-s}(k_\perp D)e^{i\theta_D(\ell-s)}J_s(k_\perp r)e^{is\theta}$$

Defining $F_s(\mathbf{r}) = J_s(k_\perp r)e^{is\theta}$ and $F_{\ell-s}(\mathbf{D}) = J_{\ell-s}(k_\perp D)e^{i\theta_D(\ell-s)}$ allows us to write $F_\ell(\mathbf{y})$ in terms of centered coordinates $F(\mathbf{r})$ as:

$$F_\ell(\mathbf{y}) = \sum_{s=-\infty}^{\infty} (-1)^{\ell-s} F_{\ell-s}(\mathbf{D})F_s(\mathbf{r}) \tag{4.2.8}$$

which gives a superposition of twisted light beams, each having a different OAM.

In this case, the vector potential centered at distance D can be written as:

$$\mathbf{A}_\ell(\mathbf{y},t) = \epsilon_\sigma F_\ell(\mathbf{y}) e^{i(k_z z-\omega t)} + c.c.$$

$$\mathbf{A}_\ell(\mathbf{y},t) = \epsilon_\sigma \sum_{s=-\infty}^{\infty} (-1)^{\ell-s} F_{\ell-s}(\mathbf{D}) F_s(\mathbf{r}) e^{i(k_z z-\omega t)} + c.c. \tag{4.2.9}$$

which can be simplified by defining $\mathbf{A}_s^{(+)}(\mathbf{r},t) = \epsilon_\sigma F_s(\mathbf{r}) e^{i(k_z z-\omega t)}$ and $\mathbf{A}_s^{(-)}(\mathbf{r},t) = \epsilon_\sigma^* F_s^*(\mathbf{r}) e^{-i(k_z z-\omega t)}$, which gives us:

$$\mathbf{A}_\ell(\mathbf{y},\mathbf{t}) = \sum_{s=-\infty}^{\infty} (-1)^{\ell-s} F_{\ell-s}(\mathbf{D}) \mathbf{A}_s^{(+)}(\mathbf{r},t) + \sum_{s=-\infty}^{\infty} (-1)^{\ell-s} F_{\ell-s}^*(\mathbf{D}) \mathbf{A}_s^{(-)}(\mathbf{r},t) \tag{4.2.10}$$

where the term $F_{\ell-s}(\mathbf{D})$ is the weight function for the summation. Figure 4.4 illustrates the weights squared $|F_{\ell-s}(D)|^2$ corresponding to the decomposed twisted beam at D in terms of twisted light beams passing through the origin O.

Once again the physics of the interaction can be determined from the matrix elements for coupling with the Hamiltonian:

$$h_\ell = -\frac{q}{m_e^*} \mathbf{A}_\ell(\mathbf{y},t).\mathbf{p}$$

By substituting the vector potential calculated in 4.2.10, we get:

$$h_\ell = \sum_{s=-\infty}^{\infty} (-1)^{\ell-s} F_{\ell-s}(\mathbf{D}) \Big[-\frac{q}{m_e^*} \mathbf{A}_s^{(+)}(r,t).\mathbf{p} \Big]$$

$$+ \sum_{s=-\infty}^{\infty} (-1)^{\ell-s} F_{\ell-s}^*(\mathbf{D}) \Big[-\frac{q}{m_e^*} \mathbf{A}_s^{(-)}(r,t).\mathbf{p} \Big] \tag{4.2.11}$$

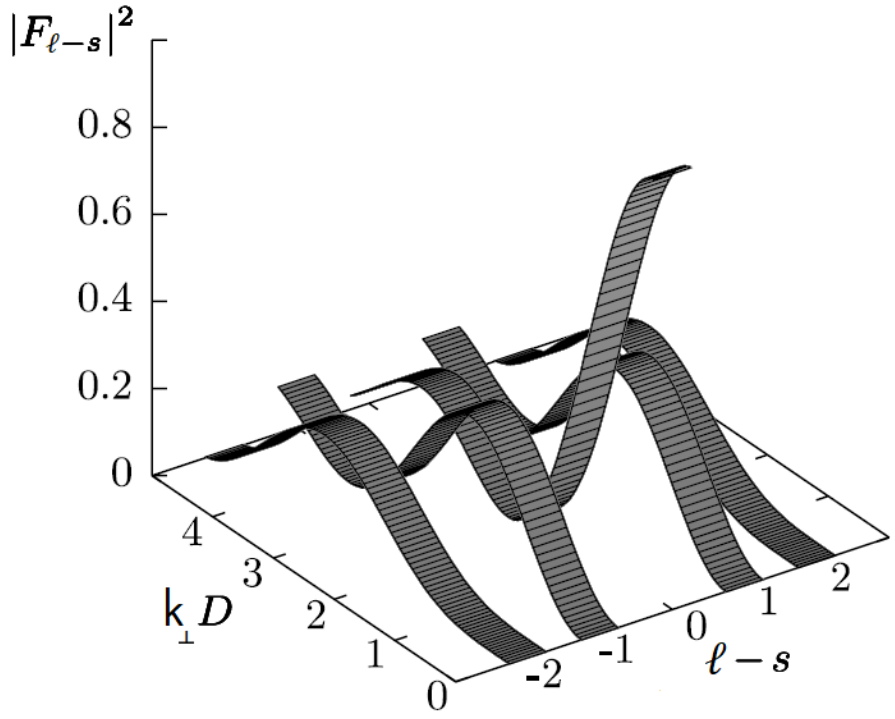

Figure 4.4: Weights corresponding to the decomposed twisted beam at D in terms of twisted beams passing through the origin O [136].

By using the calculated Hamiltonian for the coincident case (given in equation 4.1.8), we get:

$$h_\ell = \sum_{s=-\infty}^{\infty} (-1)^{\ell-s} F_{\ell-s}(\mathbf{D}) H_s^{(+)} + \sum_{s=-\infty}^{\infty} (-1)^{\ell-s} F_{\ell-s}^*(\mathbf{D}) H_s^{(-)}$$

$$h_\ell = h_\ell^{(+)} + h_\ell^{(-)} \tag{4.2.12}$$

The matrix elements of the Hamiltonian can be written as:

$$\langle c\alpha' | h_\ell^{(+)} | v\alpha \rangle = \sum_{s=-\infty}^{\infty} (-1)^{\ell-s} F_{\ell-s}(\mathbf{D}) \langle c\alpha' | H_s^{(+)} | v\alpha \rangle \tag{4.2.13}$$

$$\langle v\alpha' | h_\ell^{(-)} | c\alpha \rangle = \sum_{s=-\infty}^{\infty} (-1)^{\ell-s} F_{\ell-s}^*(\mathbf{D}) \langle v\alpha' | H_s^{(-)} | c\alpha \rangle \tag{4.2.14}$$

Applying the matrix elements calculated for the coincident case, equations 4.1.16 and 4.1.17, and the delta function, $\delta_{s,(m'-m)}$ and $\delta_{s,(m-m')}$, in these matrix elements solves the sums. This is because all sum elements vanish except when $s = m' - m$ for absorption and $s = m - m'$ for emission, which gives us:

$$\langle c\alpha' | h_\ell^{(+)} | v\alpha \rangle = (-1)^{\ell-(m'-m)} F_{\ell-(m'-m)}(\mathbf{D}) \langle c\alpha' | H_{m'-m}^{(+)} | v\alpha \rangle \tag{4.2.15}$$

$$\langle v\alpha' | h_\ell^{(-)} | c\alpha \rangle = (-1)^{\ell-(m-m')} F_{\ell-(m-m')}^*(\mathbf{D}) \langle v\alpha' | H_{(m-m')}^{(-)} | c\alpha \rangle \tag{4.2.16}$$

Thus, the matrix element when the QDs and the twisted light do not coincide for absorption ($v \to c$) is given by:

$$\langle c\alpha'|h_\ell^{(+)}|v\alpha\rangle = -\frac{2\pi q}{m_e^*}e^{-i\omega t}(\epsilon_\sigma.\mathbf{p}_{cv})F_{\ell-(m'-m)}(\mathbf{D})(-1)^{\ell-(m'-m)}$$

$$\times\int_0^\infty drrJ_{m'-m}(k_\perp r)R^*_{c\alpha'}(r)R_{v\alpha}(r) \tag{4.2.17}$$

The same can be done for emission ($c \to v$), and the matrix element is given by [136]:

$$\langle v\alpha'|h_\ell^{(-)}|c\alpha\rangle = -\frac{2\pi q}{m_e^*}e^{-i\omega t}(\epsilon^*_\sigma.\mathbf{p}_{vc})F^*_{\ell-(m-m')}(\mathbf{D})(-1)^{\ell-(m-m')}$$

$$\times\int_0^\infty drrJ_{m-m'}(k_\perp r)R^*_{v\alpha'}(r)R_{c\alpha}(r) \tag{4.2.18}$$

These matrix elements are function of $\mathbf{D}$, which indicates that for different displacement, different transition will be induced.

4.2.3 Analysis

To understand how twisted light interacts with a displaced QD, we need to determine the transition rate, $|\langle v\alpha'|h_\ell^{(+)}|c\alpha\rangle|^2$, which can be calculated using Fermi's golden rule. In order to calculate this numerically, we need to consider specific radial wavefunction, and for simplification we can use the radial wavefunction of a quantum ring. This should give us a good idea of OAM-interaction effect since this is what we are primarily interested in. The radial wavefunction for quantum ring is given by: $R(r) = \sqrt{\frac{2}{r_0 d}}\sin[\frac{\pi}{d}(r - r_0 + d/2)]$ where r_0 is the radius and d is the width of the ring and $R(r) = 0$ outside the ring. The quantum number indices in $R(r)$ are unnecessary, therefore, the

integral in the matrix element can be solved, and it is given by:

$$\int_0^\infty drrJ_{m'-m}(k_\perp r)R^*_{c\alpha'}(r)R_{v\alpha}(r) = \int_0^\infty drrJ_{m'-m}(k_\perp r)|R(r)|^2 = J_{m'-m}(k_\perp r_0) \tag{4.2.19}$$

Applying that to the matrix element, $\langle v\alpha'|h_\ell^{(+)}|c\alpha\rangle$, we get:

$$\langle v\alpha'|h_\ell^{(+)}|c\alpha\rangle = -(-1)^{\ell-(m'-m)}\frac{2\pi q}{m_e^*}e^{-i\omega t}(\epsilon_\sigma.\mathbf{p}_{cv})F_{\ell-(m'-m)}(\mathbf{D})J_{m'-m}(k_\perp r_0) \tag{4.2.20}$$

Therefore, we can determine the transition rate from:

$$|\langle v\alpha'|h_\ell^{(+)}|c\alpha\rangle|^2 = \kappa[F_{\ell-(m'-m)}(\mathbf{D})J_{m'-m}(k_\perp r_0)]^2 \tag{4.2.21}$$

where $\kappa = -(-1)^{\ell-(m'-m)}\frac{2\pi q}{m_e^*}e^{-i\omega t}(\epsilon_\sigma.\mathbf{p}_{cv})$. In other words, the transition rate is proportional to:

$$\text{Transition Rate} \propto \left[J_{\ell-(m'-m)}(k_\perp D)J_{m'-m}(k_\perp r_0)\right]^2 \tag{4.2.22}$$

This means that the probability of the transition is defined by the displacement between the beam axis and the nanostructure axis (D), the difference between the angular momentum quantum numbers ($m'-m$), and the ratio of the QD size to the beam waist ($k_\perp^{-1}$).

For example, for a twisted light beam with $\ell = 1$ and zero displacement (where the beam and the QD coincide, as shown in Figure 4.5a), the term $J_{\ell-(m'-m)}(k_\perp D) = 0$ unless $\ell-(m'-m) = 0$ (since $J_0(0) = 1$); in other words, $\ell = m'-m = 1$. Therefore, the only allowed transition is that which connects states varying by one unit of OAM. However, even when the other transitions

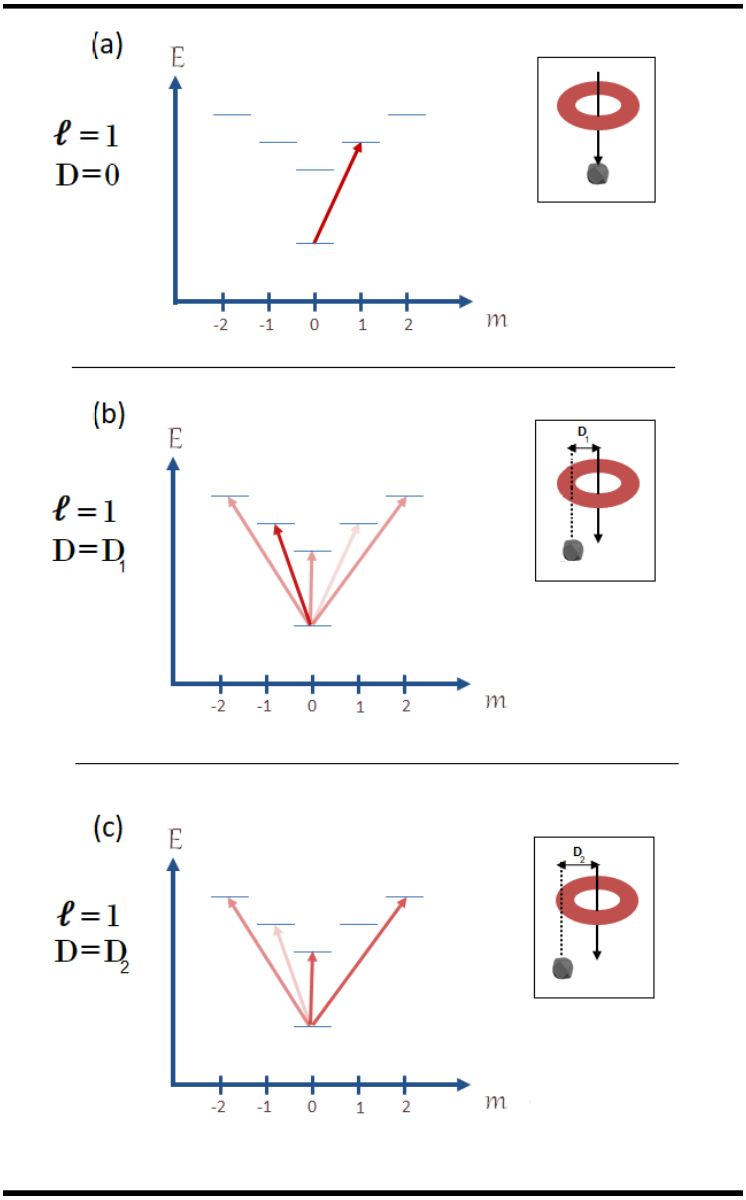

Figure 4.5: Possible transitions between a valence band and a conduction band in a QD induced by twisted light with OAM $\ell = 1$. (a) The centered beam induces only a transition between states with an angular momentum difference of $m - m = 1$. (b) The off-center beam activates several transitions with different strengths. (c) The transition with an angular momentum difference of $m - m = 1$ becomes negligible for a certain distance between the beam axis and the QD axis, D. Intensity gradient represents the strength of the transition; darker arrows represent higher transition rates.

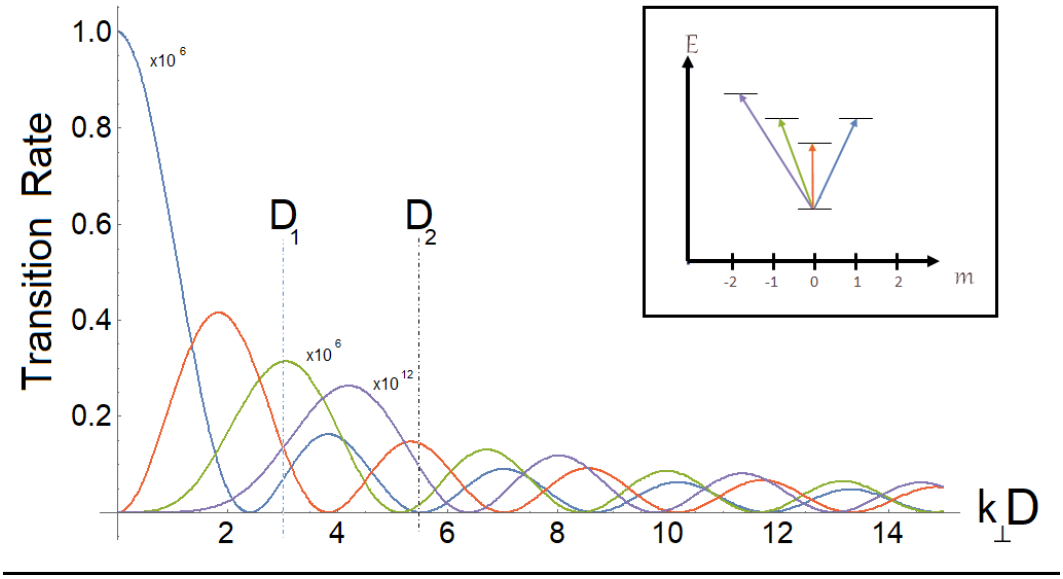

Figure 4.6: Transition rate for a beam with OAM of $\ell = 1$, and beam waist of 1 μm for different displacements, D, between the QD and the beam. Some transition are in different scales, so for visibility we multiply them by the factor shown next to the curve. The transition from $m = 0$ to $m' = 0$ is the strongest, and for smaller beam waist the curves will have the same shape but the scaling factor will be smaller and the strength of the transition rate will get closer to the transition from $m = 0$ to $m' = 0$. Dashed lines correspond to the distances, D_1 and D_2, represented in Figure 4.5.

(with $m' - m \neq 1$) are forbidden in the centered case, they start to show up once the displacement increases ($D \neq 0$, *e.g.*, D_1 shown in Figure 4.5b). This apparent violation of conservation of OAM can be justified by recalling that the off-center beam can be expressed as superposition of centered beams with different values of OAM.

Another implication worth noting is that at some displacements, (*e.g.*, D_2 shown in Figure 4.5c), some electronic transitions will not be allowed because the distance from beam center is a zero of the Bessel function, while a probability for other transitions still exists.

For example, let us consider a twisted light beam with OAM of $\ell = 1$ and a beam waist of 1 μm; we can evaluate the transition rate for different values of D using equation 4.2.22. As shown in Figure 4.6, some transition are in different scales, so for visibility we multiply them by scaling factor to show their trend. At zero displacement the only allowed transition is that connecting valence to conduction states that vary by $\pm$ one unit of orbital angular momentum. When the displacement increases, other transitions start to appear. In addition, if the beam waist size gets smaller, then the curves represented in the figure will look the same, but the scaling factor will get smaller. This is due to the fact that for smaller beam waist, the slopes from the electric field (or the electric field gradient) will be higher, which leads to more absorption in the quadrupole transition.

Spatial distribution of QDs

Lastly, to quantitatively investigate the effect of the twisted light on the absorption spectrum, let us assume that an ensemble of PbS QDs with a size of 4 nm is illuminated with light with a beam waist of 1 μm and with an OAM of $\ell = 0$ and $\ell = 1$, respectively. The absorption spectrum in Figure 4.7 shows a strong peak (at 1,000 nm) for electronic transitions from $m = 0$ to $m' = 0$ for $\ell = 0$. On the other hand, for a light beam with an OAM of $\ell = 1$, the absorption spectrum shows that for the same transition, $(0 \rightarrow 0)$, the absorption intensity is almost identical to the one induced by a plane wave. It also shows another peak (at 750 nm) for transitions from $m = 0$ to $m' = 1$, 10^{-6} orders of magnitude smaller than transitions from $m = 0$ to $m' = 0$. This suggests that the effect of the OAM of the light is very weak.

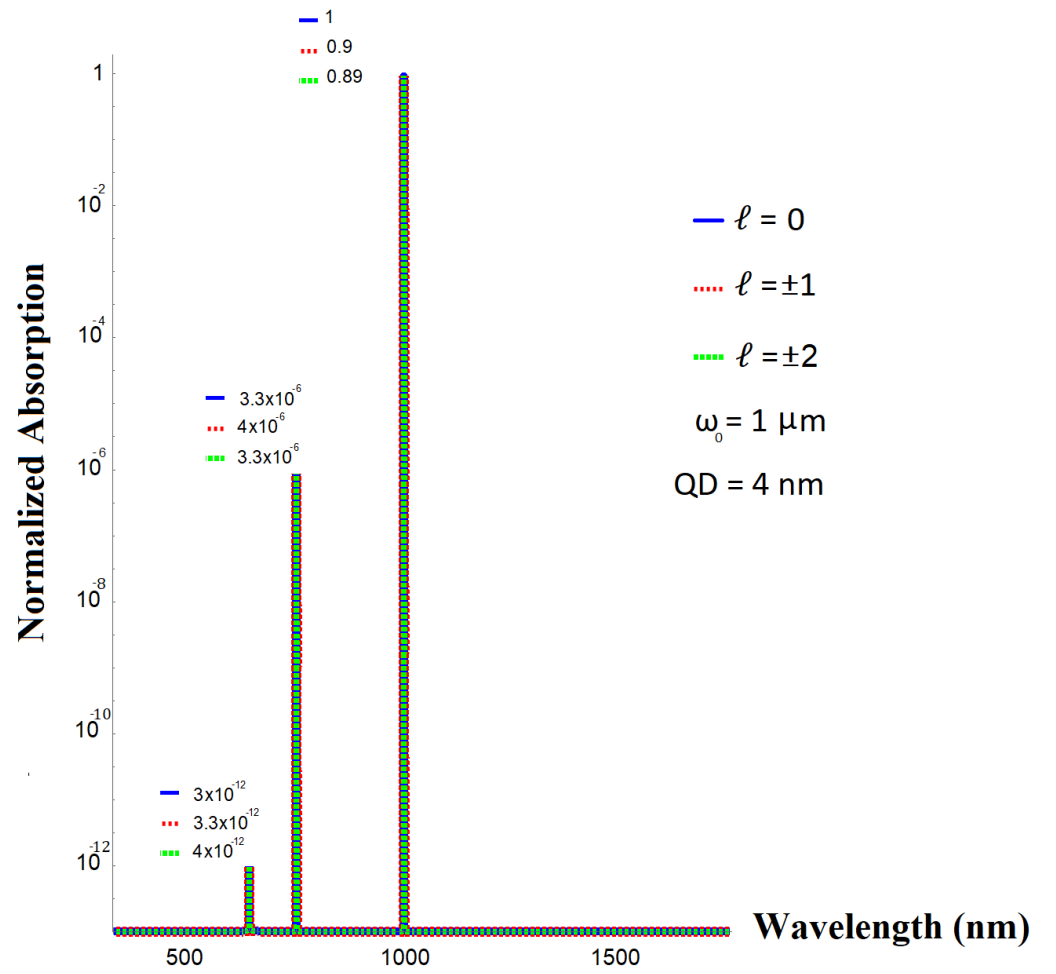

Figure 4.7: 4 nm QDs absorption spectrum when excited by plane wave of $\ell = 0$ and a twisted beam with $\ell = 1$. The transition from $m = 0$ to $m' = 1$ is 10^{-6} orders of magnitude smaller than the transition from $m = 0$ to $m' = 0$.

In addition, since the strength of the transition induced by twisted light depends on the ratio of QD size to the waist of the beam, the calculations show that the transition strength can be increased by decreasing the beam waist. For example, figure 4.8 shows the strength of the transitions induced by twisted light with $\ell = 1$ when illuminating an ensemble of QDs with a size of 4 nm and a beam waist of 100 nm and 10 nm, respectively. For a beam waist of 100 nm, the transition form $m = 0$ to $m' = 1$ is 10^{-4} orders of magnitude smaller than transitions from $m = 0$ to $m' = 0$, and it becomes comparable to those from $m = 0$ to $m' = 0$ if the beam waist is on the order of 10 nm. However, the spatial extent of focused OAM beam is governed by diffraction, therefore, getting the beam waist down to 10 nm is not possible for a free-space beam. One method to get the beam waist to be in order of 100 nm proposed by Heeres *et al* is using a plasmonic metallic nanoscale resonant antenna. Illuminating the nanoscale antenna with twisted light allows a much larger wave vectors to be obtained, which leads to overcome the restriction of free-space propagating wave vectors (which is governed by diffraction limit of $k_{max} = 2\pi/\lambda$) [155].

Moreover, when considering an ensemble with different QD sizes, the resonance energies might overlap and obscure the OAM shifts. Therefore, since this effect is very small for QDs with the same size, we should not expect to see an OAM shift when relying on inhomogeneous QD ensembles. In fact, the variation in QD size creates broadening in the resonance energies, which might be even larger than the laser's bandwidth, as shown in Figure 4.9.

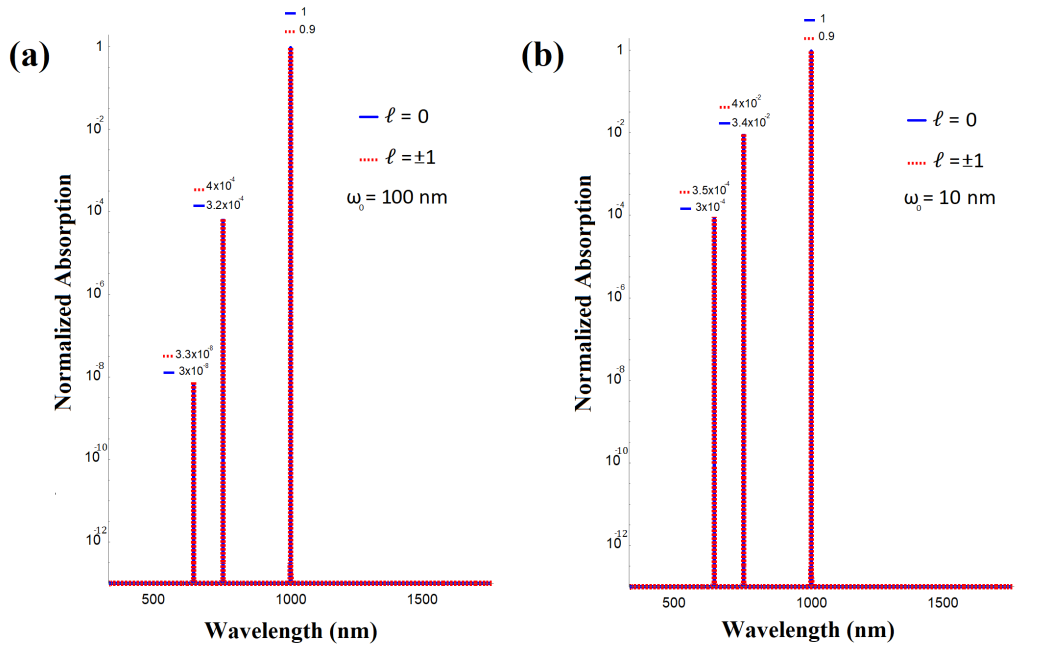

Figure 4.8: The effect of decreasing the beam waist on the strength of the transitions induced by twisted light with $\ell = 1$ when illuminating an ensemble of QDs with a size of 4 nm when the beam waist, ω_0, is (a) 100 nm and (b) 10 nm. For $\omega_0 = 100$ nm the transition from $m = 0$ to $m' = 1$ is 10^{-4} orders of magnitude smaller than the transition from $m = 0$ to $m' = 0$, and for $\omega_0 = 10$ nm, the transition from $m = 0$ to $m' = 1$ is 10^{-2} orders of magnitude smaller than the transition from $m = 0$ to $m' = 0$

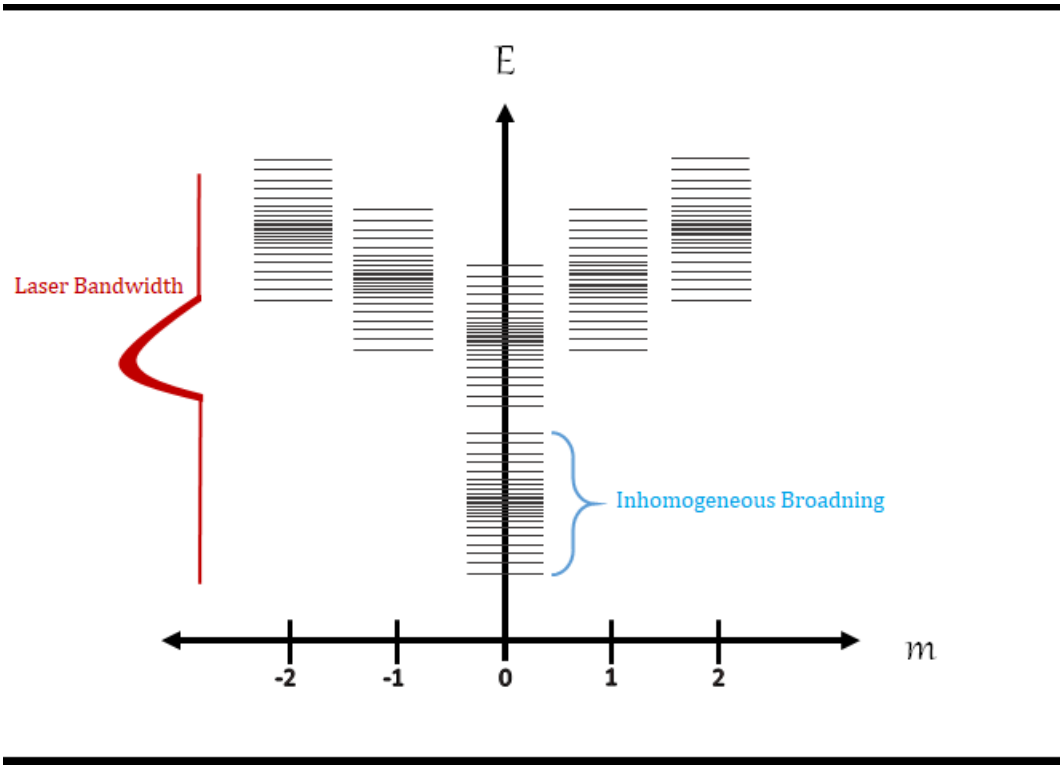

Figure 4.9: Inhomogeneous broadening due to variation in QD size causes an overlap of energy levels larger than the laser bandwidth.

4.3 Conclusion

In this chapter, the theory of optical transitions in semiconductor QDs induced by light beams with OAM was presented. We also explored the calculation of the transition matrix element. These calculations show that for a QD center on the excitation beam the beam parameters such as OAM quantum number, and beam waist determine the electron's excited state. They also show that the transition induced by twisted light is much weaker than the value of the transition using plane wave light.

We investigated the effect that twisted light has on the QD when the symmetry axes of the twisted light and the QD do not coincide. Writing the off-center beam as a superposition of beams with different OAM values centered at the position of the nanostructure allows us to determine the possible transitions in terms of the centered case given in [147]. The calculations also show that the transition between states is a function of the distance between the beam axis and the nanostructure, and the strength of the transition depends on the ratio of QD size to the waist of the beam.

In the next chapter, we will examine this theory experimentally, by illuminating QDs with light that has controllable OAM and then measuring the spectrum of the transmitted light. We then compare absorption spectra for several OAM values and look for OAM dependence. The experimental details are presented in the following chapter.

Chapter 5

OAM Resolved Spectroscopy

5.1 Analyzing the Absorption Spectrum

In this experiment we attempt to measure OAM transfer from light to an ensemble of semiconductor QDs. To achieve this, we illuminate QDs with light that has controllable OAM and then measure the spectrum of the transmitted light. We compare absorption spectra for several OAM values and look for OAM dependence.

5.1.1 Experimental Setup

Light with helical wavefronts was generated by shining a Ti:sapphire pulsed laser (center wavelength: ∼800 nm, bandwidth: 30 nm, pulse duration: ∼100 fs, polarization: linear S-polarized) on a spatial light modulator (Cambridge Correlators SDE1024 SLM) that displayed a forked diffraction grating. A 90:10 beam splitter put 90% of the light into the signal beam and 10% into a reference beam. The signal beam was focused onto the sample

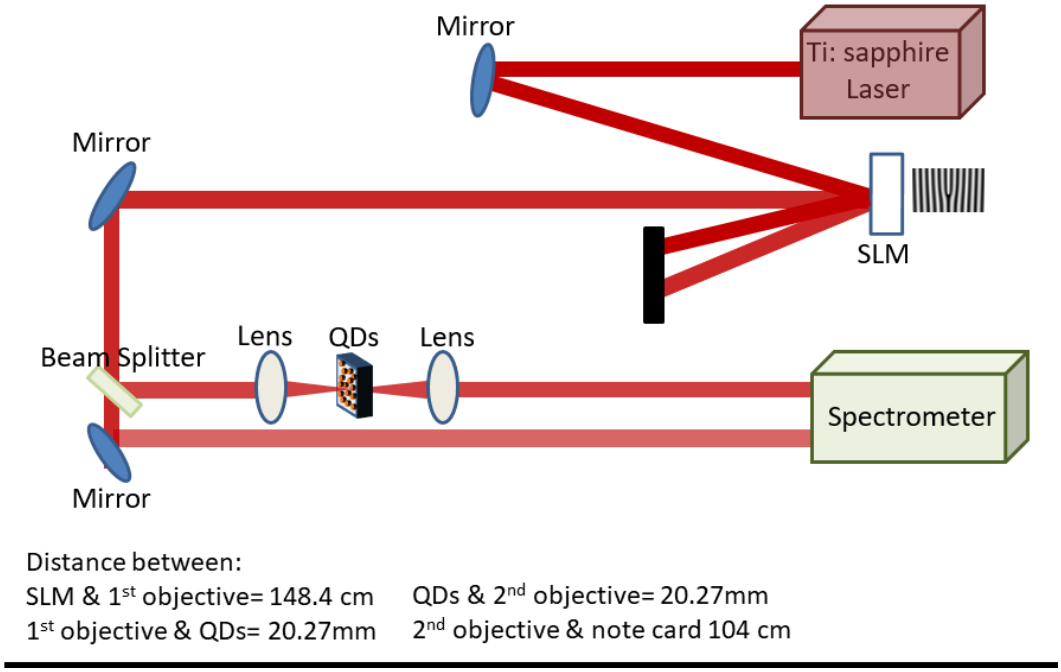

Figure 5.1: Experimental setup for measuring OAM coupling from light to a QD ensemble.

with a long-working-distance microscope objective lens (34 mm, NA = 0.28). Another objective lens (working distance = 30.5 mm and NA = 0.26) was used to recollimate the beam after it passed through the QD sample. The beams were detected by a spectrometer with a multimode optical fiber input. The experimental setup is shown in Figure 5.1.

Spatial Chirp Correction

Femtosecond pulses have a large bandwidth, which could create a dispersion problem when generating twisted light. Because the techniques used to generate monochromatic twisted light might not always be suitable, generating twisted light with broadband lasers has been receiving increased atten-

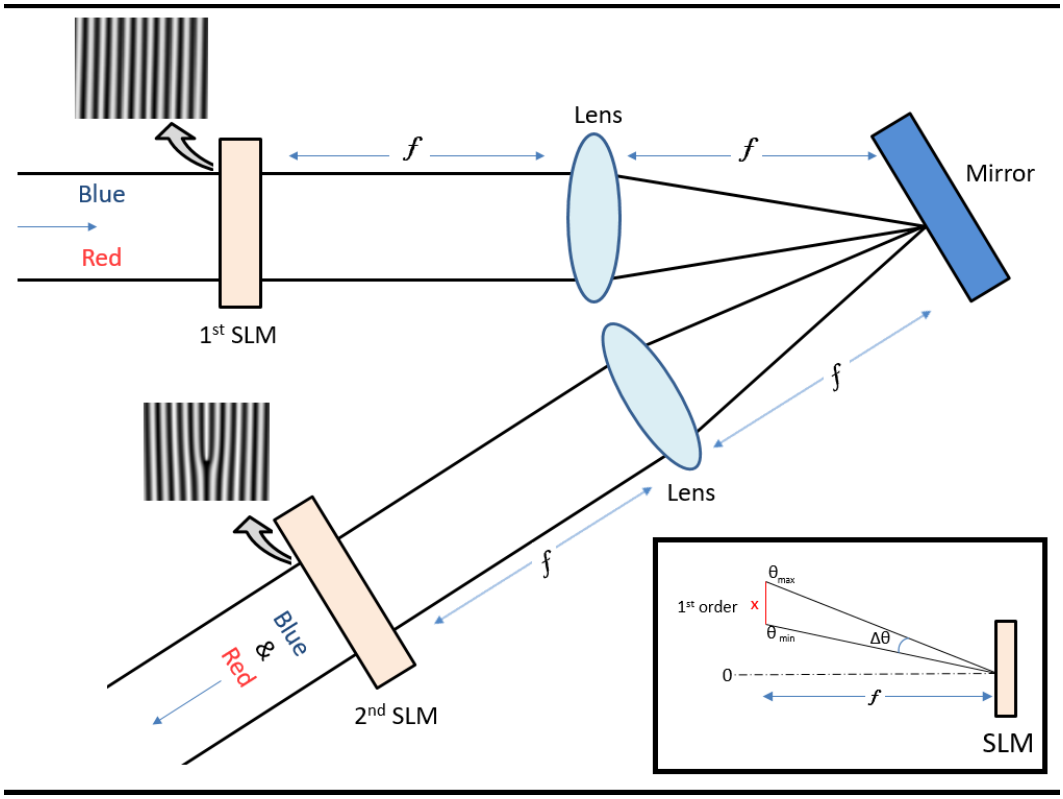

Figure 5.2: Illustration of the $4f$ setup. Ultrafast pulses propagate from left to right and travel through the following optical elements: an SLM that displays a diffraction grating, two lenses that have equal focal lengths of f, and a second SLM that displays a fork grating. Inset: geometric detail for calculating angular dispersion.

tion [156–158]. We attempted to apply the $4f$ technique used in [159, 160] to compensate for any spatial dispersion. For this technique, a fork diffraction grating is used to generate a twisted beam, and a second grating is used to correct the spatial chirp. Figure 5.2 illustrates the $4f$ setup that we built. However, one disadvantage of using this setup is the low intensity of the resultant beam. This is mainly because the beam is passing through two gratings, and we only use the first order of the diffracted beams. Therefore, instead of using a normal grating we used a blazed diffraction grating, which maximizes grating efficiency in a desired diffraction order while minimizing the power in the other orders (more detail about generating these different types of gratings is given in Appendix A).

Because different wavelengths diffract differently, we calculated the diffraction angle, θ, for both maximum and minimum wavelengths in our laser bandwidth using the diffraction relationship:

$$n\lambda = d\sin(\theta) \tag{5.1.1}$$

where $n = 1$ for the first diffraction order, λ is the wavelength, and d is the separation of grating lines. This separation distance can be found by dividing the SLM width by the number of lines in the grating:

$$d = \frac{\text{total SLM width}}{\text{number of lines in grating}} = \frac{1.3 \text{ cm}}{200} = 65000 \text{ nm}$$

Using this distance, the maximum wavelength, λ_{max}= 820 nm, and the minimum wavelength λ_{min}= 790 nm, we obtain from equation 5.1.1 the diffraction angles: $\theta_{max} = 0.723°$ and $\theta_{min} = 0.696°$; thus $\Delta\theta = 0.027°$. For f=30 cm and

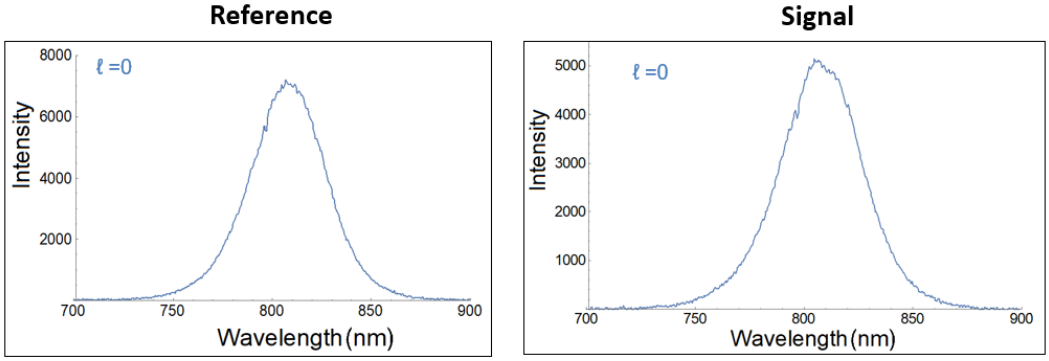

Figure 5.3: The measured spectra for the reference beam and signal beam for OAM of $\ell = 0$.

by using a simple geometric analysis, we can calculate the distance x which defines the angular dispersion (see inset in Figure 5.2):

$$x = \tan(\Delta\theta) \times f = 0.14\text{mm}$$

which was much smaller than the beam diameter used in this experiment (*i.e.* 7 mm) and can be ignored. Therefore, based on the previous calculation, as well as by comparing the beam modes with and without the $4f$ setup, we discovered that the spatial dispersion was not extreme and can be corrected using simple imaging. In other words, we imaged the SLM onto the sample with the first microscope objective, and then we imaged the sample onto the detector with the second objective.

5.1.2 Method

First, spectra for beams with different OAM values ($\ell = 0$, 1, 3, 4, 5, 10, and 15) were acquired for both reference and signal beams, *i.e.*, the spectrum

of the laser through air and through the QDs. Figure 5.3 shows an example of two measured spectra for $\ell = 0$ through air and through QDs. We then calculated the differential absorption between the two cases:

$$\text{Differential absorption} = \frac{\text{Reference-Signal}}{\text{Reference}} \tag{5.1.2}$$

The differential absorption for $\ell = 0$ and the comparison with the QD absolute absorption (which was obtained with the spectrophotometer) is shown in Figure 5.4. In this case, we expect the calculated differential absorption and the QD absorption to be the same (since $\ell = 0$, which is essentially a plane wave).

We observed that the beam coupling into the spectrometer was critical and difficult to maintain as the mode of the twisted light was changed. We explored several techniques for optimizing this coupling, as discussed in the next section.

5.1.3 Coupling with the Spectrometer

First Detection Technique

First, we sent the transmitted beam to a note card and then measured the scattered light from the card. The distance between the sample and the card was calculated so that the light from the sample would be imaged onto the card. This technique was the most uniform in beam-spectrometer coupling. Even when we moved to higher twisted beam modes (*e.g.*, $\ell = 15$), the coupling was the same. However, a problem with this method was the very low intensity

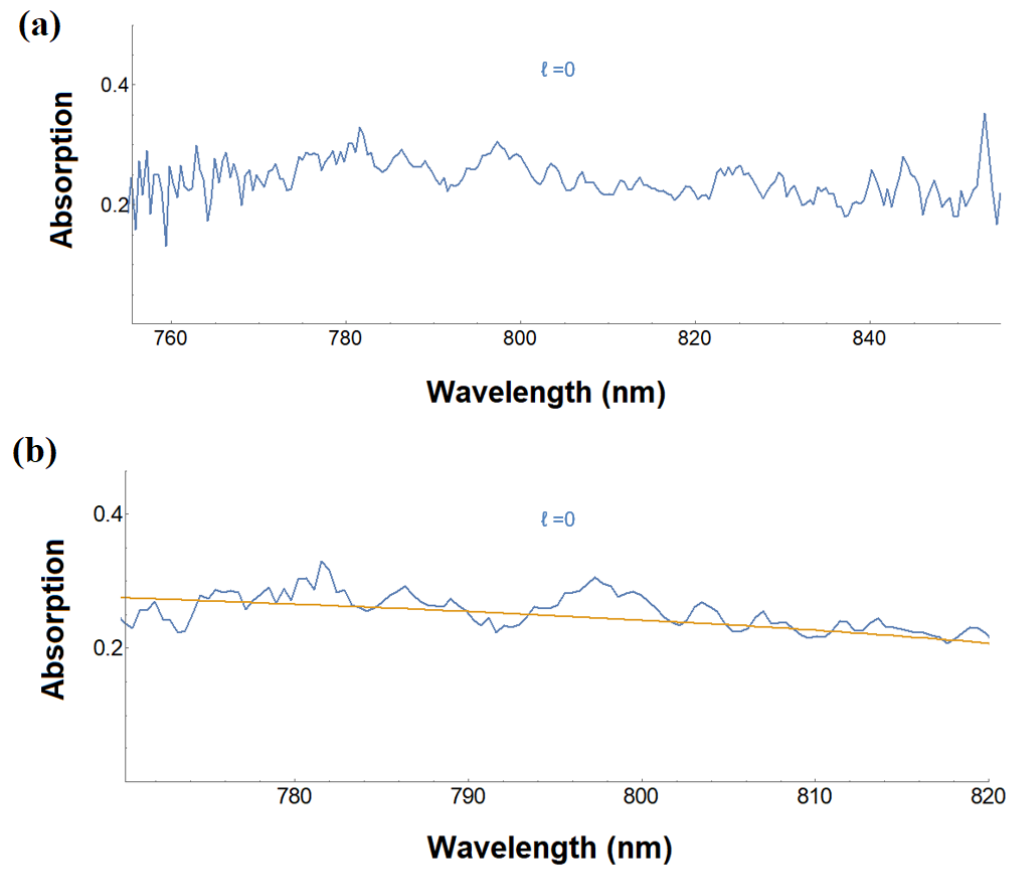

Figure 5.4: (a) The differential absorption for $\ell = 0$ obtained using Ti:sapphire laser coupled into the spectrometer, and (b) comparison between the obtained spectrum with the QD absolute absorption spectrum acquired with the spectrophotometer.

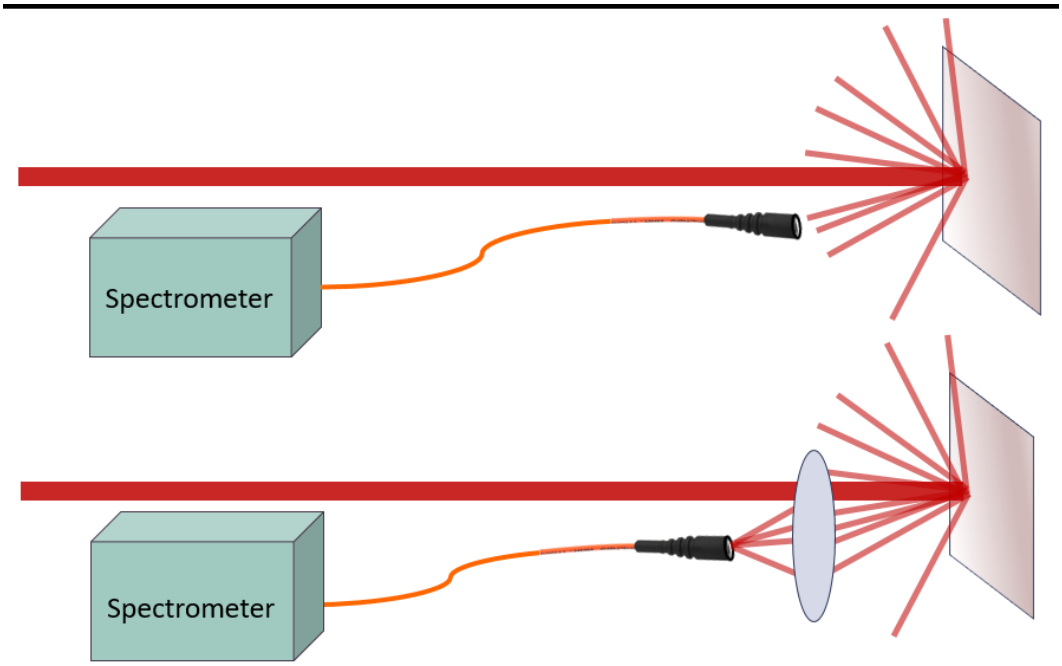

Figure 5.5: Detection techniques used for optimizing the beam coupling onto the spectrometer.

of the detected light. The signal-to-noise ratio was consequently very low, and we could not see changes in the absorption spectra with changing the value of the OAM.

Second Detection Technique

Our second method also measured the scattered light from a card, but this time we used a lens with a short focal length (f= 2.5 cm) to focus more of the scattered light onto the optical fiber. This method increased the signal significantly, and the signal-to-noise ratio was much higher. A problem with this detection technique was that the coupling onto the spectrometer becomes inefficient at higher OAM modes, and the latest results showed a

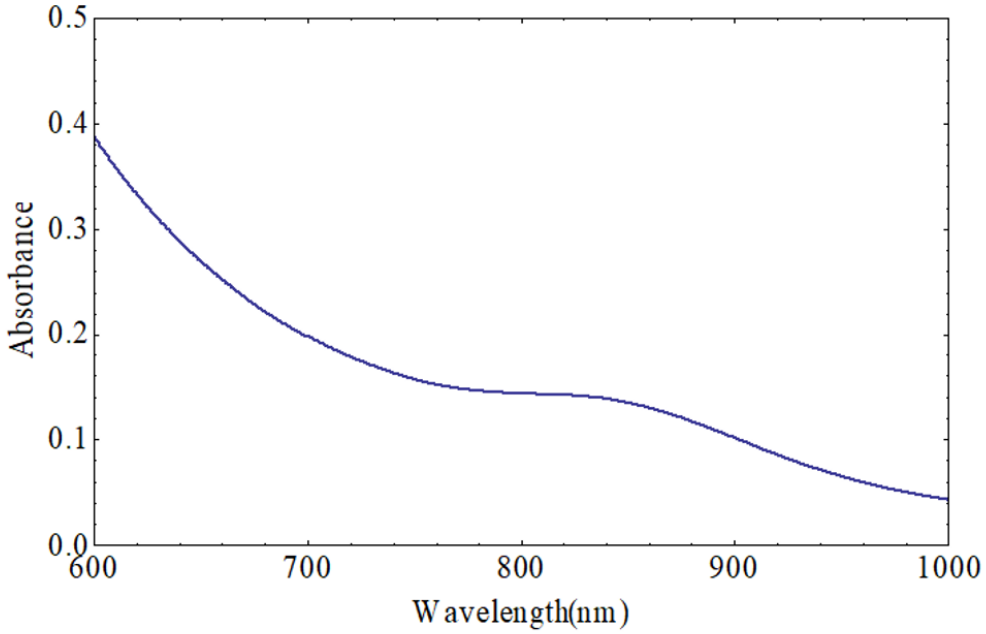

Figure 5.6: PbS quantum dot absolute absorption spectrum acquired with the spectrophotometer shows strong absorption at 800 nm (which is the peak wavelength for the Ti:sapphire pulsed laser). The broad peak indicates the sample inhomogeneity.

strong OAM dependence—not from changes in the absorption spectrum, but from beam-mode-induced changes in the total amount of detected light. Figure 5.5 illustrates these detection methods.

We also tried different method to optimize the beam coupling into the spectrometer. We tried to send the beam directly to the spectrometer without attaching the optical fiber. We also tried to attach a lens directly into the fiber. However, in both technique the coupling was not optimal, and changing the beam mode was affecting the beam coupling significantly.

5.1.4 QD Sample

A PbS QD (colloidal PbS in hexane) film was prepared by dip coating on glass substrates. Figure 5.6 shows the absorption spectrum for the QD sample used in this experiment.

The size of the QDs used in this experiment ranged from 2 nm to 5 nm. Because the ratio of the QD radius to the beam waist is critical, we varied the beam diameter coming into the objective and then calculated and measured experimentally the beam waist at the focus.

Calculating the Beam Waist

It is well known that when focusing Gaussian beams, the bigger the beam the tighter the focus—or the smaller the beam waist. For this experiment, a small beam waist was desirable.

To calculate the beam waist at the sample ($2\omega_0$, where ω_0 is the radius) we needed to use: the laser peak wavelength λ= 800 nm, the objective focal length at f= 20 mm, and the beam diameter (D) coming into the focusing objective. Finally, we applied all these measurements to the following equations:

$$2\omega_0 = \frac{4\lambda}{\pi}\frac{f}{D} \tag{5.1.3}$$

For example, for a beam diameter of 7 mm (before the objective lens), the beam waist at the focus was 2.91 μm, and for a beam diameter of 5 mm, the beam waist was 4.07 μm.

However, we needed to consider in this configuration the objective lens entrance pupil. For example, the focusing objective we used in this experi-

ment had entrance pupil of 10 mm, but when changing the mode of the beam to higher OAM values, the beam diameter could exceed that of the objective entrance. Therefore, we chose to work with smaller beam diameters to increase the possible OAM values that would have diameters smaller than that of the objective entrance. In particular, the diameter of the beam used in this experiment (D) was 3 mm, thus, the beam waist, $2\omega_0$, was 6.79 μm.

Measuring the Beam Waist

The QDs were mounted on a three-axis translation stage. X and Y translation stages helped us scan the sample to choose different spots for analysis. The Z axis allowed us to move the sample closer to or farther from the first objective to minimize the spot size on the sample. Scattered light from the QDs was also imaged by a lens onto a CCD (not shown in Figure 5.1). By adjusting the sample distance from the objective, we could minimize the beam spot size such that the QD sample was always at the beam waist.

To measure the beam waist at the focus, we started with a Gaussian beam ($\ell = 0$), and the beam diameter coming into the focusing objective was 3 mm. A note card was then placed at the sample position to maximize the scattered light for better imaging. Then, we placed a lens with focal length of $f = 2.54$ cm close to the note card at a distance $d_0 = 3.4$ cm, and the CCD was placed at distance, d_i. We first calculated d_i using the thin-lens equation given by:

$$\frac{1}{f} = \frac{1}{d_0} + \frac{1}{d_i} \tag{5.1.4}$$

By solving the previous equation for d_i, the image distance from the lens (where

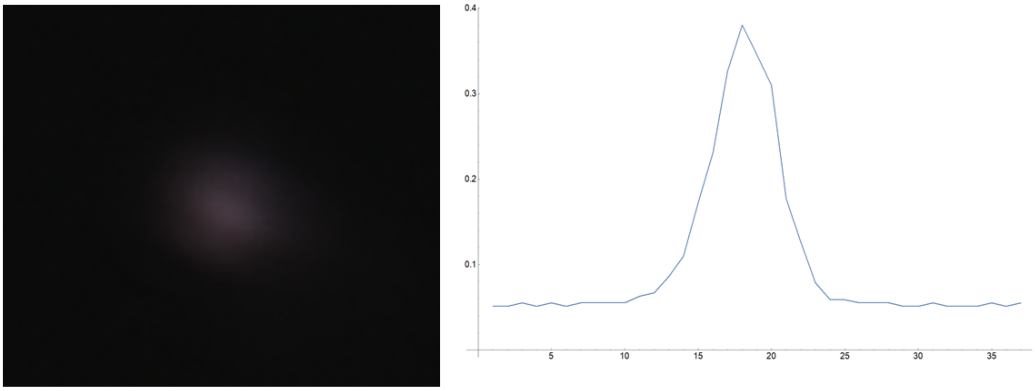

Figure 5.7: Image of the beam waist at the sample and the corresponding Gaussian profile. Note: OD filter was placed to reduce the intensity to avoid saturation.

the CCD should be placed) was $d_i = 10$ cm. Therefore, the magnification (M) can be found by calculating d_i/d_o, which in this case results in $M = 2.95$.

The image of the beam spot at the focus was then processed by Mathematica to calculate the image size from the number of pixels across the image. By taking a cross section and plotting it, we get a Gaussian-like profile and then calculate the full width at half maximum (FWHM) from that. In this case, FWHM = 6.35 pixels, and the CCD pixel spacing was 3.2 μm. Therefore, the size of the beam at the focus is:

$$\omega_o = \frac{\text{pixel spacing}}{M}\text{FWHM} \tag{5.1.5}$$

We measured a beam waist $\omega_0 = 6.89$ μm, which agrees with our previous calculation. Figure 5.7 shows the beam waist image and the corresponding Gaussian profile used to calculate the number of pixels across the beam diameter.

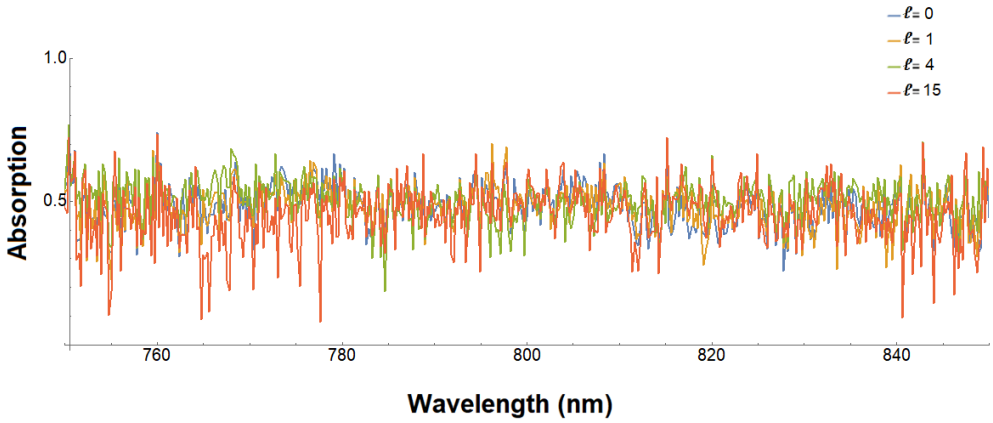

Figure 5.8: Differential absorption for beams for $\ell = 0, 1, 4$, and 15. No OAM-dependence in the absorption spectra was noted with the first detection technique.

5.1.5 Data

When using the first detection technique (no lens between card and spectrometer), the signal-to-noise ratio was low (in this case, S/N = 8). The differential absorption for a few different OAM modes (ℓ = 0, 1, 4, 15) with the QDs are provided in Figure 5.8.

Using the second detecting technique (lens placed between card and spectrometer), we still did not see differences in the absorption spectra. We plotted the differential absorption for different OAM modes (ℓ = 1, 3, 4, 5, and 10) and compared them to the case with no OAM (l = 0). The differential absorption for different OAM values found with this technique are given in Figure 5.9.

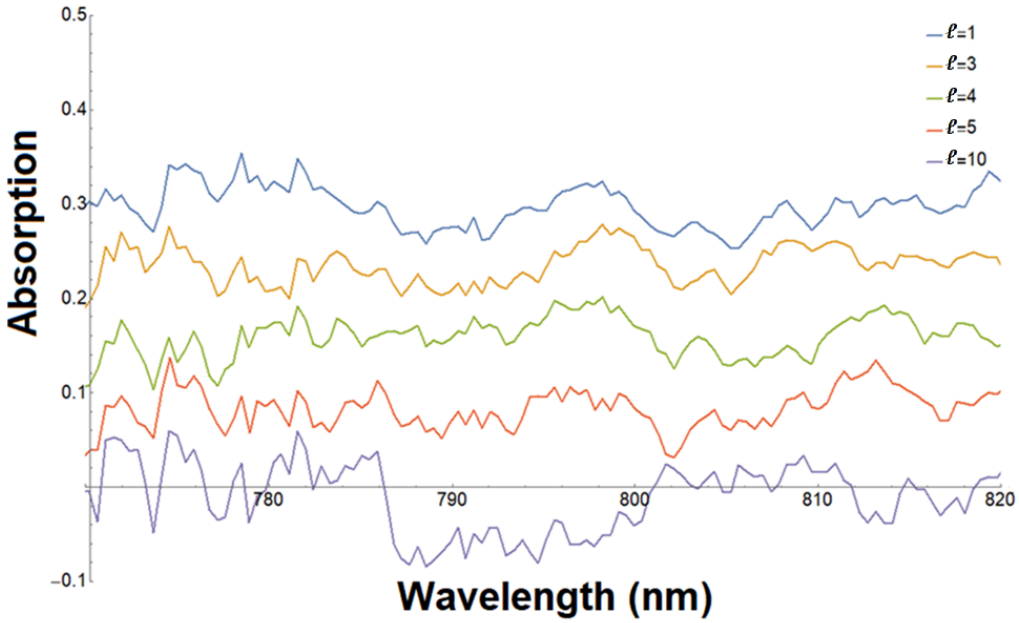

Figure 5.9: Differential absorption for beams for $\ell = 1, 3, 4, 5$, and 10 using the second detection technique. We observed an overall decrease in detected light with increasing ℓ because of poorer coupling into the spectrometer.

Data Analysis

We tried various data analysis methods to see if there were any changes in the spectrum that could be connected to having OAM in the light. We first looked for any changes in both the standard deviation and the mean when changing the ℓ value. We also attempted to fit the differential absorption to a line with different tilt and look for horizontal changes with different OAMs, but still did not see any OAM effect in the absorption spectra.

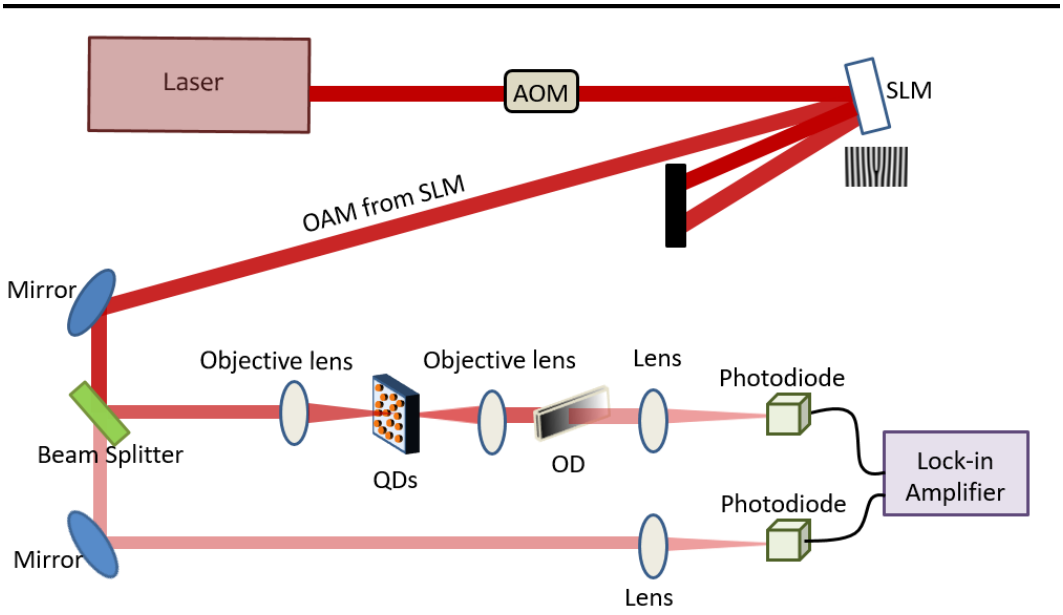

Figure 5.10: Experimental setup for measuring total absorption.

5.2 Measuring Total Absorption

We also took a different approach to look for OAM dependence. Since the width of the spectral feature is set by the QD dispersion and it is bigger than the laser bandwidth, then what we are looking for is a change (increase or decrease) in the total absorption. Therefore, by measuring and comparing the absorption for different OAM values, we might determine the OAM dependence.

To measure the total absorption, the beam was modulated sinusoidally at 10 kHz by an Acousto-Optic Modulator (AOM), ISOMET 1205C-2 and 222A-2 driver. Both the signal and reference beams were measured with photodiodes and then sent to a lock-in amplifier (SR810). A continuous OD filter was placed on the signal beam path to balance the intensity in each path,

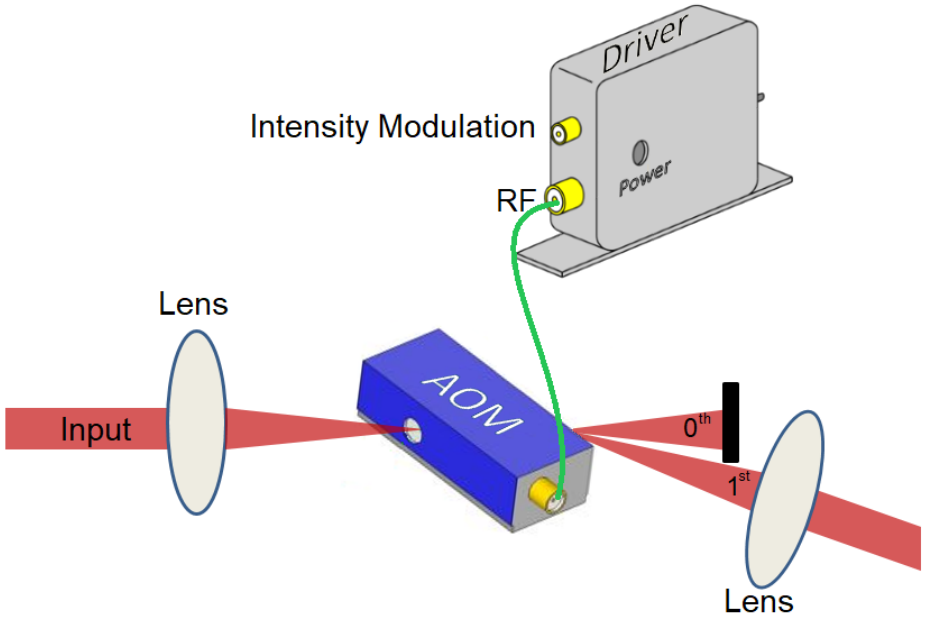

Figure 5.11: An acoustic wave is generated in the crystal by applying a RF drive signal. Consequently, the AOM diffracts part of the incident laser light into a single output order.

enabling sensitive differential measurements. The setup for measuring the total absorption is shown in figure 5.10.

AOM Alignment

The AOM device controls the laser beam intensity or modulation by using the acousto-optic effect to diffract and shift the frequency of light [161]. A radio frequency (RF) drive applies a signal to a lead molybdate ($PbMoO_4$) crystal which in turn generates an acoustic wave. This sound wave in the crystal causes changes in the refractive index, which diffracts the incident light. The AOM is designed to diffract a high proportion of the incident laser beam into a single output order (see Figure 5.11). The performance is optimized by

the orientation and precise positioning of the AOM. Since most AOM devices operate in the Bragg regime, the incident angle performance is maximized at particular incidence angle known as Bragg angle. Therefore, by mounting the AOM on a rotation stage, we can control the output beam intensity by changing the input beam incident angle. In addition, to increase modulation rates, the beam needs to be focused at the AOM.

5.2.1 Calibration

Determining the total absorption for light with different OAMs can be achieved by comparing the signal beam that passes through the QDs to its reference beam. However, since the beam splitter reflects 90% of the laser light, additional steps are needed to produce a meaningful comparison. First, we started without the QD sample (so there is no absorption from the QDs) and with a Gaussian beam $\ell = 0$. In this configuration, we want the difference between the two beams to be as close as possible to zero; to achieve this, we placed an OD filter in the signal beam to reduce the amount of light collected by the photodiode. The minimum amplitude for the difference between the two beams was about 5 microvolts (with approximately 1-microvolt electronics noise).

5.2.2 Data

We observed that increasing the OAM value increased the difference between the signal and reference beams, and we believe this was due to the signal beam being clipped by the objective at higher OAM values. To correct

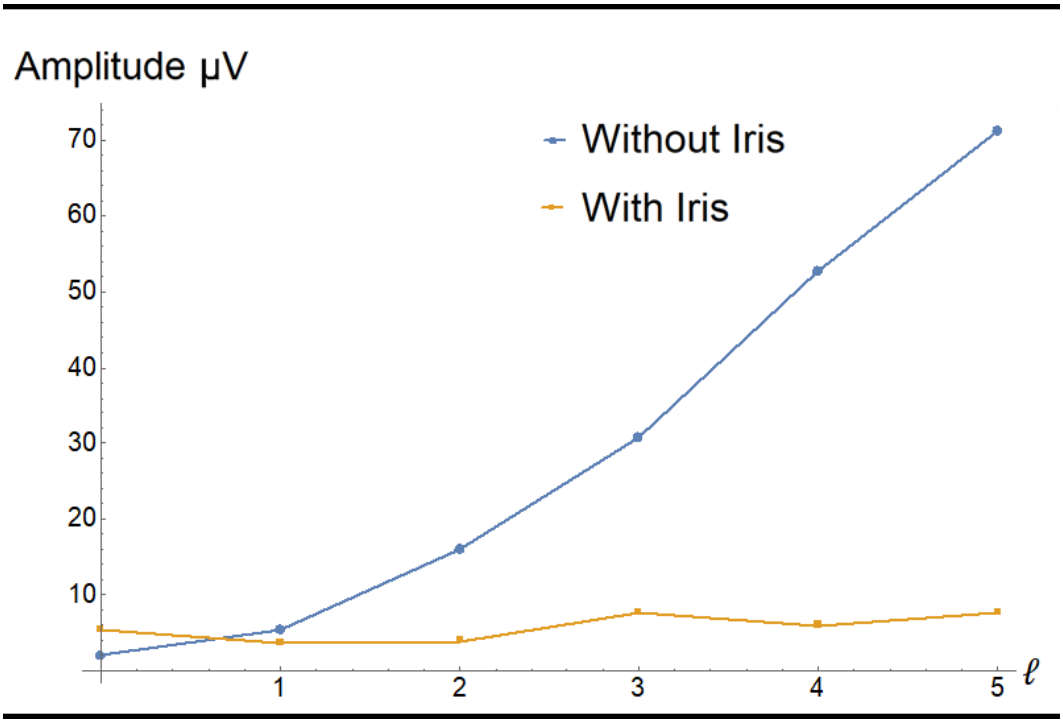

Figure 5.12: Amplitude of the difference between the signal beam and the reference beam for different OAM values before and after adding the iris. Before adding the iris, the beam was clipping on the objective and therefore the difference between the two beam was incresing with increasing the ℓ value. After adding the iris, the comparison between the two beams is more accurate.

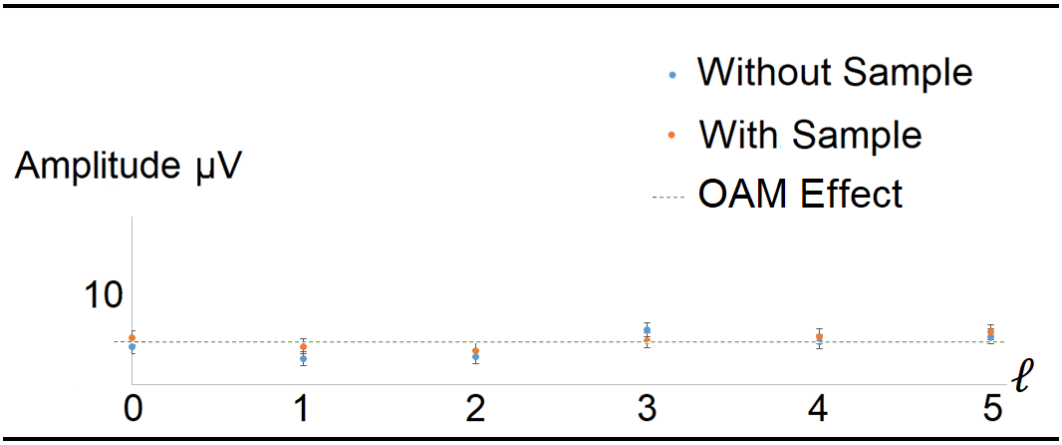

Figure 5.13: The average amplitude (of the difference between the signal and reference beams) for different OAM values for three different spots in the sample, and a comparison with the measured amplitude before inserting the sample. The dotted line indicate that the OAM has no effect on the total absorption when considering the the electronic noise error.

this, we placed an iris on the reference beam path to block some of the beam at higher OAMs. We chose $\ell = 5$ as our highest OAM value, and at that value we adjusted the iris to minimize the difference between the two beams. Figure 5.12 shows the difference between the two beams (without sample) for different OAM values before and after adding the iris.

After minimizing the differences between the signal and reference beams for a range of OAM values, we inserted the QD sample and repeated the steps (because the sample absorbs some of the light, we needed to adjust the OD filter). We started with a Gaussian beam and adjusted the continuous OD filter until the amplitude of the difference was minimized. Then we measured the amplitude for different OAM values at three different spots on the sample. We calculated the average amplitude on these three spots and compare that to the amplitude between the different between the signal beam and the reference beam without the sample (see Figure 5.13).

The observed amplitudes with and without the QD sample were varying with changing the beam mode by $1 - 1.8$ microvolts. In other words, the amplitudes of the difference between the signal and reference beams for different OAM were extremely close to each other, and they were almost identical when considering the 1-microvolt noise. This suggests that the OAM of light had no effect on total absorption.

5.3 Discussion

We predicted that the effect of the OAM of the light is very weak on the absorption spectrum of a QD ensemble when considering homogeneous QDs. Therefore, we would not expect to see an OAM shift when relying on inhomogeneous QD ensembles. In other words, the lack of homogeneity in the sample plays a significant role in measurement; the QD size ranged from 2 to 5 nm in diameter. In addition to the variation in the QD size, the distribution of the QDs in our sample is very random, and this is important since the distance between each QD and the center of the beam is a major contributor to the transition rate. Therefore, even when fixing the distance between the QD and the beam center, the QD size remains inhomogeneous.

Another limiting experimental factor may be related to the beam size at the sample. The beam waist in this measurement was about 7 μm. Smaller beam waists can be achieved by expanding the beam before the objective, but this was limited by the objective entrance pupil. Because of the ratio of the QD size to the beam waist, there is a possibility that each QD sees the beam as a tilted plane wave, which is similar to having no OAM but at a tilted angle.

5.4 Conclusion

We tried various methods to detect OAM transfer from the light to the QDs. We first acquired absorption spectra for the QDs using beams with different OAM values and analyzed the spectra by calculating the differential absorption. We used two different techniques to acquire these spectra, and we did not observe OAM dependence in the differential absorption spectra.

We also measured the total absorption for the QDs when illuminating them with twisted light. However, we did not observe any significant changes in the total absorption when we changed the OAM value.

We predicted that the OAM dependence would be very small when considering illuminating a homogeneous QD ensemble, and it would be very unlikely to detect an OAM shift when relying on inhomogeneous QD ensembles. In other words, the fact that we could not observe OAM dependence in the absorption spectrum is consistent with our predictions.

Chapter 6

Conclusion and Next Steps

In 1992 Allen *et al* realized that helically phased light beams carry orbital angular momentum. Since then, researchers have continued to find ways to use this new degree of freedom for a variety of applications. Consequently, the way twisted light interacts with solid-state matter has become an area of growing interest.

The primary goal of this research is to study light-matter interaction using light that carries OAM. We theoretically investigate the transfer of OAM from light to an ensemble of semiconductor-based QDs, calculating the transition matrix elements for the light-matter interaction and determining the corresponding selection rules. We started with determining the optical ransition induced by twisted light and the QD when the light beam and nanostructures axis coincide. Then we investigated a more realistic case of the interaction of twisted beam with QDs when the symmetry axis of the beam and the axis of the nanostructure do not coincide since in QDs ensemble each QD sees a light beam that is displaced by a different distance relative to itself. These

calculations show that for a displaced beam the transition between states is a function of the distance between the center of the beam and the nanostructure, and the rate of the transition depends on the QD size relative to that of the beam waist.

We also examine the light-matter interaction experimentally using an ensemble of colloidal PbS QDs via two different approaches. First, we measure the absorption spectrum by illuminating the QDs with light that has controllable OAM and compare the absorption spectra for several OAM values. We also measure and compare the total absorption for several OAM values to search for OAM dependence. Our measurements of the spectra and total absorption does not reveal transfer of orbital angular momentum to the nanostructure target.

We may not have been able to measure the transfer of OAM from the twisted light beam to the nanostructures because of experimental limitations including, inhomogeneous size of the QDs, and the ratio of the beam waist to the QD size. We believe that the sample inhomogeneity plays a major role in our null results because the optical transition depends on the size of the nanostructure. In fact, due to the fact that the off-center beam can be ssen as a superposition of beams with different value of OAM, our theoretical calculation predicted that the transition from $m = 0$ to $m' = 1$ was 10^{-6} order of magnitude smaller than the transition from $m = 0$ to $m' = 0$. In other words, we predicted that (for homogeneous QDs ensemble) to be able to detected the transfer of OAM from the light to the QDs we would need to measure the absorption to 10^{-6}, therefore, we were not expecting to be able to detect that transfer with inhomogeneous QDs ensemble.

If OAM is involved in light-matter interaction, the nonvertical transitions (*e.g.* $m = 0$ and $m' = 1$) would be much weaker than the vertical ones (*e.g.* $m = 0$ and $m' = 0$) when considering illuminating QDs ensemble. Therefore, optimizing the experiment to measure OAM transfer would require making adjustments to both the sample and the laser beam to increase sensitivity. For the sample, we need a more homogeneous QD target. While colloidal PbS QDs are easy to synthesize, they have a range of sizes varying from 2 to 5 nm. Because absorption depends on QD diameter, a more consistent size should improve the signal. By fixing the QD size, we could reduce the factors affecting the transition strength as well as resolve other factors, such as the distance between each QD and the beam center. One approach would be to image the radial direction of the sample onto a detector to spatially resolve the interaction. In this case, we would be looking at specific QDs that are at a certain distance from the beam center.

In addition to using QDs with a more consistent size, the ratio of the QD size to beam waist should also be adjusted. To increase the ratio of the QD size to beam waist we would need to decreased the beam waist (since incresing the QD size could affect the confinement). The waist of the beam used in this measurement was about 7 μm, and a smaller beam waist would certainly enhance the possibility of detecting OAM dependence. For example for a beam waist of 100 nm the strength of the transition rate can be enhanced by 10^2 order of magnitude for transition from $m = 0$ to $m' = 1$.

Finally, in this experiment, the laser beam loses a significant amount of power before detection. The spatial light modulator diffracts the beam into several diffraction orders, and only one diffracted light beam is used while

the other orders have to be blocked. In addition, the most efficient detection technique used for optimizing the beam coupling onto the spectrometer was measuring the scattered light from a note card, resulting in significant power loss. As a result of these experimental aspects, the signal-to-noise ratio in this experiment is very low. Increasing the power in the incident beam could improve the ratio.

Although we did not observe OAM dependence experimentally, we believe that the OAM should be involved in light-matter interaction and it might be impossible to detect this transfer of OAM when considering an inhomogeneous ensemble of nanoparticles. In the end, we can say that the orbital angular momentum of light has taught us to think differently about light while we await the new uses of twisted light yet to be discovered.

Bibliography

[1] L. Allen, M. W. Beijersbergen, R. Spreeuw, and J. Woerdman, "Orbital angular momentum of light and the transformation of Laguerre-Gaussian laser modes," *Physical Review A*, vol. 45, no. 11, p. 8185, 1992.

[2] A. Einstein, "Über einen die erzeugung und verwandlung des lichtes betreffenden heuristischen gesichtspunkt," *Annalen der Physik*, vol. 322, no. 6, pp. 132–148, 1905.

[3] L. Mandel and E. Wolf, *Optical coherence and quantum optics*. Cambridge University Press, 1995.

[4] J. W. Simmons and M. J. Guttmann, *States, waves, and photons: A modern introduction to light*. Addison-Wesley, 1970.

[5] K. Y. Bliokh, F. Rodríguez-Fortuño, F. Nori, and A. V. Zayats, "Spin–orbit interactions of light," *Nature Photonics*, vol. 9, no. 12, p. 796, 2015.

[6] Wikipedia contributors, "Circular polarization — Wikipedia, the free encyclopedia," 2019. [Online; accessed 26-February-2019].

[7] A. M. Yao and M. J. Padgett, "Orbital angular momentum: origins, behavior and applications," *Advances in Optics and Photonics*, vol. 3, no. 2, pp. 161–204, 2011.

[8] L. Allen, M. Padgett, and M. Babiker, "The orbital angular momentum of light," in *Progress in optics*, vol. 39, pp. 291–372, Elsevier, 1999.

[9] J. C. Maxwell, *A dynamical theory of the electromagnetic field*. The Society, 1864.

[10] J. H. Poynting *et al.*, "The wave motion of a revolving shaft, and a suggestion as to the angular momentum in a beam of circularly polarised light," *Proc. R. Soc. Lond. A*, vol. 82, no. 557, pp. 560–567, 1909.

[11] M. Padgett, J. Courtial, and L. Allen, "Light's orbital angular momentum," *Physics Today*, vol. 57, no. 5, pp. 35–40, 2004.

[12] R. A. Beth, "Mechanical detection and measurement of the angular momentum of light," *Phys. Rev.*, vol. 50, pp. 115–125, 1936.

[13] S. Franke-Arnold and N. Radwell, "Light served with a twist," *Optics and Photonics News*, vol. 28, no. 6, pp. 28–35, 2017.

[14] J. W. Goodman, *Introduction to Fourier optics*. Roberts and Company Publishers, 2005.

[15] L. C. Andrews and R. L. Phillips, *Laser beam propagation through random media*, vol. 152. SPIE Press, 2005.

[16] S. M. Barnett and L. Allen, "Orbital angular momentum and nonparaxial light beams," *Optics Communications*, vol. 110, no. 5-6, pp. 670–678, 1994.

[17] A. O'neil, I. MacVicar, L. Allen, and M. Padgett, "Intrinsic and extrinsic nature of the orbital angular momentum of a light beam," *Physical Review Letters*, vol. 88, no. 5, p. 053601, 2002.

[18] Y. Zhao, J. S. Edgar, G. D. Jeffries, D. McGloin, and D. T. Chiu, "Spin-to-orbital angular momentum conversion in a strongly focused optical beam," *Physical Review Letters*, vol. 99, no. 7, p. 073901, 2007.

[19] A. Siegman, *Lasers*. University Science Books, 1986.

[20] O. Svelto and D. C. Hanna, *Principles of lasers*, vol. 4. Springer, 1998.

[21] B. Saleh and M. Teich, *Fundamentals of photonics*. Wiley Series in Pure and Applied Optics, Wiley, 2007.

[22] M. I. Kolobov, *Quantum imaging*. Springer Science & Business Media, 2007.

[23] A. Siegman, "Hermite-Gaussian functions of complex argument as optical-beam eigenfunctions," *JOSA*, vol. 63, no. 9, pp. 1093–1094, 1973.

[24] D. J. Griffiths, *Introduction to electrodynamics*. AAPT, 2005.

[25] M. V. Berry and K. McDonald, "Exact and geometrical optics energy trajectories in twisted beams," *Journal of Optics A: Pure and Applied Optics*, vol. 10, no. 3, p. 035005, 2008.

[26] J. P. Torres and L. Torner, *Twisted photons: Applications of light with orbital angular momentum*. John Wiley & Sons, 2011.

[27] M. Beijersbergen, R. Coerwinkel, M. Kristensen, and J. Woerdman, "Helical-wavefront laser beams produced with a spiral phaseplate," *Optics Communications*, vol. 112, no. 5-6, pp. 321–327, 1994.

[28] G. Turnbull, D. Robertson, G. Smith, L. Allen, and M. Padgett, "The generation of free-space Laguerre-Gaussian modes at millimetre-wave frequencies by use of a spiral phaseplate," *Optics Communications*, vol. 127, no. 4-6, pp. 183–188, 1996.

[29] S. Oemrawsingh, J. Van Houwelingen, E. Eliel, J. Woerdman, E. Verstegen, J. Kloosterboer, *et al.*, "Production and characterization of spiral phase plates for optical wavelengths," *Applied optics*, vol. 43, no. 3, pp. 688–694, 2004.

[30] M. W. Beijersbergen, L. Allen, H. Van der Veen, and J. Woerdman, "Astigmatic laser mode converters and transfer of orbital angular momentum," *Optics Communications*, vol. 96, no. 1-3, pp. 123–132, 1993.

[31] J. Courtial, K. Dholakia, L. Allen, and M. Padgett, "Gaussian beams with very high orbital angular momentum," *Optics Communications*, vol. 144, no. 4-6, pp. 210–213, 1997.

[32] V. Y. Bazhenov, M. Vasnetsov, and M. Soskin, *Laser beams with screw dislocations in their wavefronts*. PhD thesis, 1990.

[33] N. Heckenberg, R. McDuff, C. Smith, and A. White, "Generation of optical phase singularities by computer-generated holograms," *Optics Letters*, vol. 17, no. 3, pp. 221–223, 1992.

[34] V. Y. Bazhenov, M. Soskin, and M. Vasnetsov, "Screw dislocations in light wavefronts," *Journal of Modern Optics*, vol. 39, no. 5, pp. 985–990, 1992.

[35] S. Topuzoski and L. Janicijevic, "Fraunhofer diffraction of a Laguerre-Gaussian laser beam by fork-shaped grating," *Journal of Modern Optics*, vol. 58, no. 2, pp. 138–145, 2011.

[36] P. Bierdz, M. Kwon, C. Roncaioli, and H. Deng, "High fidelity detection of the orbital angular momentum of light by time mapping," *New Journal of Physics*, vol. 15, no. 11, p. 113062, 2013.

[37] A. Mair, A. Vaziri, G. Weihs, and A. Zeilinger, "Entanglement of the orbital angular momentum states of photons," *Nature*, vol. 412, no. 6844, p. 313, 2001.

[38] M. Padgett and L. Allen, "Light with a twist in its tail," *Contemporary Physics*, vol. 41, no. 5, pp. 275–285, 2000.

[39] M. Harris, C. Hill, P. Tapster, and J. Vaughan, "Laser modes with helical wave fronts," *Physical Review A*, vol. 49, no. 4, p. 3119, 1994.

[40] I. Basistiy, V. Y. Bazhenov, M. Soskin, and M. V. Vasnetsov, "Optics of light beams with screw dislocations," *Optics Communications*, vol. 103, no. 5-6, pp. 422–428, 1993.

[41] N. Heckenberg, R. McDuff, C. Smith, H. Rubinsztein-Dunlop, and M. Wegener, "Laser beams with phase singularities," *Optical and Quantum Electronics*, vol. 24, no. 9, pp. S951–S962, 1992.

[42] A. DErrico, R. DAmelio, B. Piccirillo, F. Cardano, and L. Marrucci, "Measuring the complex orbital angular momentum spectrum and spatial mode decomposition of structured light beams," *Optica*, vol. 4, no. 11, pp. 1350–1357, 2017.

[43] J. Hickmann, E. Fonseca, W. Soares, and S. Chávez-Cerda, "Unveiling a truncated optical lattice associated with a triangular aperture using lights orbital angular momentum," *Physical Review Letters*, vol. 105, no. 5, p. 053904, 2010.

[44] L. E. de Araujo and M. E. Anderson, "Measuring vortex charge with a triangular aperture," *Optics Letters*, vol. 36, no. 6, pp. 787–789, 2011.

[45] D. L. Andrews, *Structured light and its applications: An introduction to phase-structured beams and nanoscale optical forces*. Academic press, 2011.

[46] A. Ashkin, "Acceleration and trapping of particles by radiation pressure," *Physical Review Letters*, vol. 24, no. 4, p. 156, 1970.

[47] A. Ashkin, J. M. Dziedzic, J. Bjorkholm, and S. Chu, "Observation of a single-beam gradient force optical trap for dielectric particles," *Optics Letters*, vol. 11, no. 5, pp. 288–290, 1986.

[48] H. He, M. Friese, N. Heckenberg, and H. Rubinsztein-Dunlop, "Direct observation of transfer of angular momentum to absorptive particles from a laser beam with a phase singularity," *Physical Review Letters*, vol. 75, no. 5, p. 826, 1995.

[49] M. Friese, J. Enger, H. Rubinsztein-Dunlop, and N. R. Heckenberg, "Optical angular-momentum transfer to trapped absorbing particles," *Physical Review A*, vol. 54, no. 2, p. 1593, 1996.

[50] N. Simpson, K. Dholakia, L. Allen, and M. Padgett, "Mechanical equivalence of spin and orbital angular momentum of light: An optical spanner," *Optics Letters*, vol. 22, no. 1, pp. 52–54, 1997.

[51] T. Xie, H. Wang, F. Yuan, S. Chang, P. Sun, S. Zhang, H. Li, S. Liu, C. Wang, and Z. Zheng, "Arbitrary manipulation of micro-particles in three dimensions by steering of multiple orbital angular momentum modes," in *Optical Trapping and Optical Micromanipulation XIV*, vol. 10347, p. 103470Y, International Society for Optics and Photonics, 2017.

[52] L.-M. Zhou, K.-W. Xiao, J. Chen, and N. Zhao, "Optical levitation of nanodiamonds by doughnut beams in vacuum," *Laser & Photonics Reviews*, vol. 11, no. 2, 2017.

[53] D. McGloin, N. B. Simpson, and M. J. Padgett, "Transfer of orbital angular momentum from a stressed fiber-optic waveguide to a light beam," *Applied Optics*, vol. 37, no. 3, pp. 469–472, 1998.

[54] G. Gibson, J. Courtial, M. J. Padgett, M. Vasnetsov, V. Pasko, S. M. Barnett, and S. Franke-Arnold, "Free-space information transfer using light beams carrying orbital angular momentum," *Optics Express*, vol. 12, no. 22, pp. 5448–5456, 2004.

[55] J. Wang, J.-Y. Yang, I. M. Fazal, N. Ahmed, Y. Yan, H. Huang, Y. Ren, Y. Yue, S. Dolinar, M. Tur, *et al.*, "Terabit free-space data transmission employing orbital angular momentum multiplexing," *Nature Photonics*, vol. 6, no. 7, p. 488, 2012.

[56] A. E. Willner, H. Huang, Y. Yan, Y. Ren, N. Ahmed, G. Xie, C. Bao, L. Li, Y. Cao, Z. Zhao, *et al.*, "Optical communications using orbital angular momentum beams," *Advances in Optics and Photonics*, vol. 7, no. 1, pp. 66–106, 2015.

[57] N. Bozinovic, Y. Yue, Y. Ren, M. Tur, P. Kristensen, H. Huang, A. E. Willner, and S. Ramachandran, "Terabit-scale orbital angular momentum mode division multiplexing in fibers," *Science*, vol. 340, no. 6140, pp. 1545–1548, 2013.

[58] A. Trichili, K.-H. Park, M. Zghal, B. S. Ooi, and M.-S. Alouin, "Communicating using spatial mode multiplexing: Potentials, challenges and perspectives," *arXiv preprint arXiv:1808.02462*, 2018.

[59] B. Rodenburg, M. P. Lavery, M. Malik, M. N. OSullivan, M. Mirhosseini, D. J. Robertson, M. Padgett, and R. W. Boyd, "Influence of atmospheric turbulence on states of light carrying orbital angular momentum," *Optics Letters*, vol. 37, no. 17, pp. 3735–3737, 2012.

[60] L. Torner, J. P. Torres, and S. Carrasco, "Digital spiral imaging," *Optics Express*, vol. 13, no. 3, pp. 873–881, 2005.

[61] V. Westphal, S. O. Rizzoli, M. A. Lauterbach, D. Kamin, R. Jahn, and S. W. Hell, "Video-rate far-field optical nanoscopy dissects synaptic vesicle movement," *Science*, vol. 320, no. 5873, pp. 246–249, 2008.

[62] S. W. Hell and J. Wichmann, "Breaking the diffraction resolution limit by stimulated emission: Stimulated-emission-depletion fluorescence microscopy," *Optics Letters*, vol. 19, no. 11, pp. 780–782, 1994.

[63] W. Yu, Z. Ji, D. Dong, X. Yang, Y. Xiao, Q. Gong, P. Xi, and K. Shi, "Super-resolution deep imaging with hollow Bessel beam STED microscopy," *Laser & Photonics Reviews*, vol. 10, no. 1, pp. 147–152, 2016.

[64] H. Blom and J. Widengren, "Stimulated emission depletion microscopy," *Chemical Reviews*, vol. 117, no. 11, pp. 7377–7427, 2017.

[65] G. A. Swartzlander, "Peering into darkness with a vortex spatial filter," *Optics Letters*, vol. 26 8, pp. 497–9, 2001.

[66] G. Foo, D. M. Palacios, and G. A. Swartzlander, "Optical vortex coronagraph," *Optics Letters*, vol. 30, no. 24, pp. 3308–3310, 2005.

[67] G. A. Swartzlander, E. L. Ford, R. S. Abdul-Malik, L. M. Close, M. A. Peters, D. M. Palacios, and D. W. Wilson, "Astronomical demonstration of an optical vortex coronagraph," *Optics Express*, vol. 16, no. 14, pp. 10200–10207, 2008.

[68] J. Kühn, E. Serabyn, J. Lozi, N. Jovanovic, T. Currie, O. Guyon, T. Kudo, F. Martinache, K. Liewer, G. Singh, *et al.*, "An h-band vector vortex coronagraph for the Subaru coronagraphic extreme adaptive optics system," *Publications of the Astronomical Society of the Pacific*, vol. 130, no. 985, p. 035001, 2018.

[69] G. A. Swartzlander Jr, "The optical vortex coronagraph," *Journal of Optics A: Pure and Applied Optics*, vol. 11, no. 9, p. 094022, 2009.

[70] B. Pullman, *The atom in the history of human thought*. Oxford University Press, USA, 2001.

[71] M. Fox, *Quantum optics: An introduction*, vol. 15. OUP Oxford, 2006.

[72] W. T. Hill III and C. H. Lee, *Light-Matter interaction: Atoms and molecules in external fields and nonlinear optics*. John Wiley & Sons, 2008.

[73] J. B. Pendry, A. J. Holden, D. J. Robbins, and W. Stewart, "Magnetism from conductors and enhanced nonlinear phenomena," *IEEE Transactions on Microwave Theory and Techniques*, vol. 47, no. 11, pp. 2075–2084, 1999.

[74] A. C. Phillips, *Introduction to quantum mechanics*. John Wiley & Sons, 2013.

[75] A. Beiser, *Concepts of modern physics*. Tata McGraw-Hill Education, 2003.

[76] E. Schrödinger, "An undulatory theory of the mechanics of atoms and molecules," *Physical Review*, vol. 28, no. 6, p. 1049, 1926.

[77] R. A. Serway and J. W. Jewett, *Physics for scientists and engineers with modern physics*. Cengage Learning, 2018.

[78] Wikipedia contributors, "Hydrogen-like atom — Wikipedia, the free encyclopedia," 2019. [Online; accessed 26-February-2019].

[79] P. A. M. Dirac, "The quantum theory of the emission and absorption of radiation," *Proc. R. Soc. Lond. A*, vol. 114, no. 767, pp. 243–265, 1927.

[80] E. Fermi, *Nuclear physics: A course given by Enrico Fermi at the University of Chicago*. University of Chicago Press, 1950.

[81] H. Haug and S. W. Koch, *Quantum theory of the optical and electronic properties of semiconductors: Fifth edition*. World Scientific Publishing Company, 2009.

[82] J. D. Jackson, "Classical electrodynamics," 1999.

[83] M. Cahay, "Quantum confinement VI: Nanostructured materials and devices: Proceedings of the international symposium," The Electrochemical Society, 2001.

[84] A. Nozik, "Quantum dot solar cells," *Physica E: Low-Dimensional Systems and Nanostructures*, vol. 14, no. 1-2, pp. 115–120, 2002.

[85] I. Robel, V. Subramanian, M. Kuno, and P. V. Kamat, "Quantum dot solar cells. harvesting light energy with cdse nanocrystals molecularly linked to mesoscopic tio2 films," *Journal of the American Chemical Society*, vol. 128, no. 7, pp. 2385–2393, 2006.

[86] P. V. Kamat, "Quantum dot solar cells. semiconductor nanocrystals as light harvesters," *The Journal of Physical Chemistry C*, vol. 112, no. 48, pp. 18737–18753, 2008.

[87] B. Choi, S. Hwang, I. Kim, H. Shin, Y. Kim, and E. Kim, "Fabrication and room-temperature characterization of a silicon self-assembled quantum-dot transistor," *Applied Physics Letters*, vol. 73, no. 21, pp. 3129–3131, 1998.

[88] G. Konstantatos, M. Badioli, L. Gaudreau, J. Osmond, M. Bernechea, F. P. G. De Arquer, F. Gatti, and F. H. Koppens, "Hybrid graphene–

quantum dot phototransistors with ultrahigh gain," *Nature nanotechnology*, vol. 7, no. 6, p. 363, 2012.

[89] S. Karmakar, *Novel three-state quantum dot gate field effect transistor*, vol. 6. Springer, 2014.

[90] V. I. Klimov and M. G. Bawendi, "Ultrafast carrier dynamics, optical amplification, and lasing in nanocrystal quantum dots," *MRS Bulletin*, vol. 26, no. 12, pp. 998–1004, 2001.

[91] G. Konstantatos, I. Howard, A. Fischer, S. Hoogland, J. Clifford, E. Klem, L. Levina, and E. H. Sargent, "Ultrasensitive solution-cast quantum dot photodetectors," *Nature*, vol. 442, no. 7099, p. 180, 2006.

[92] P. Bhattacharya and Z. Mi, "Quantum-dot optoelectronic devices," *Proceedings of the IEEE*, vol. 95, no. 9, pp. 1723–1740, 2007.

[93] C. Kittel, P. McEuen, and P. McEuen, *Introduction to solid state physics*, vol. 8. Wiley New York, 1996.

[94] M. L. Cohen and J. R. Chelikowsky, *Electronic structure and optical properties of semiconductors*, vol. 75. Springer Science & Business Media, 2012.

[95] G. Konstantatos, *Colloidal quantum dot optoelectronics and photovoltaics*. Cambridge University Press, 2013.

[96] R. S. Yadav, P. Mishra, R. Mishra, M. Kumar, and A. C. Pandey, "Growth mechanism and optical property of CdS nanoparticles synthe-

sized using amino-acid histidine as chelating agent under sonochemical process," *Ultrasonics Sonochemistry*, vol. 17, no. 1, pp. 116–122, 2010.

[97] K. Kyhm, J. Kim, S. Kim, and H.-s. Yang, "Gain dynamics and excitonic transition in CdSe colloidal quantum dots," *Optical Materials*, vol. 30, no. 1, pp. 158–160, 2007.

[98] T. Rajh, O. I. Micic, and A. J. Nozik, "Synthesis and characterization of surface-modified colloidal cadmium telluride quantum dots," *The Journal of Physical Chemistry*, vol. 97, no. 46, pp. 11999–12003, 1993.

[99] H.-J. Byun, J. C. Lee, and H. Yang, "Solvothermal synthesis of InP quantum dots and their enhanced luminescent efficiency by post-synthetic treatments," *Journal of Colloid and Interface Science*, vol. 355, no. 1, pp. 35–41, 2011.

[100] T. Puangmali, M. Califano, and P. Harrison, "Monotonic evolution of the optical properties in the transition from three- to quasi-two-dimensional quantum confinement in InAs nanorods," *The Journal of Physical Chemistry C*, vol. 114, no. 15, pp. 6901–6908, 2010.

[101] K. Zhu, J. Shi, and L. Zhang, "Preparation and optical absorption of insb microcrystallites embedded in SiO2 thin films," *Solid State Communications*, vol. 107, no. 2, pp. 79–84, 1998.

[102] O. Madelung, *Semiconductors: Data handbook*. Springer Science & Business Media, 2012.

[103] C. E. Ekuma, D. J. Singh, J. Moreno, and M. Jarrell, "Optical properties of PbTe and PbSe," *Physical Review B*, vol. 85, no. 8, p. 085205, 2012.

[104] M. G. Kanatzidis, "Nanostructured thermoelectrics: the new paradigm?," *Chemistry of Materials*, vol. 22, no. 3, pp. 648–659, 2009.

[105] A. L. Rogach, *Semiconductor nanocrystal quantum dots*. Springer, 2008.

[106] L. Jacak, P. Hawrylak, and A. Wójs, *Quantum dots*. Springer Science & Business Media, 2013.

[107] L. Brus, "Electronic wave functions in semiconductor clusters: Experiment and theory," *The Journal of Physical Chemistry*, vol. 90, no. 12, pp. 2555–2560, 1986.

[108] S. V. Gaponenko, *Optical properties of semiconductor nanocrystals*, vol. 23. Cambridge University Press, 1998.

[109] A. Yoffe, "Semiconductor quantum dots and related systems: Electronic, optical, luminescence and related properties of low dimensional systems," *Advances in Physics*, vol. 50, no. 1, pp. 1–208, 2001.

[110] B. O. Dabbousi, J. Rodriguez-Viejo, F. V. Mikulec, J. R. Heine, H. Mattoussi, R. Ober, K. F. Jensen, and M. G. Bawendi, "(CdSe) ZnS core-shell quantum dots: Synthesis and characterization of a size series of highly luminescent nanocrystallites," *The Journal of Physical Chemistry B*, vol. 101, no. 46, pp. 9463–9475, 1997.

[111] J. K. Jaiswal, H. Mattoussi, J. M. Mauro, and S. M. Simon, "Long-term multiple color imaging of live cells using quantum dot bioconjugates," *Nature Biotechnology*, vol. 21, no. 1, p. 47, 2003.

[112] N. N. Greenwood and A. Earnshaw, *Chemistry of the Elements*. Elsevier, 2012.

[113] M. A. Hines and G. D. Scholes, "Colloidal PbS nanocrystals with size-tunable near-infrared emission: Observation of post-synthesis self-narrowing of the particle size distribution," *Advanced Materials*, vol. 15, no. 21, pp. 1844–1849, 2003.

[114] M. Friese, T. Nieminen, N. Heckenberg, and H. Rubinsztein-Dunlop, "Optical alignment and spinning of laser-trapped microscopic particles," *Nature*, vol. 394, no. 6691, p. 348, 1998.

[115] B. Piccirillo, C. Toscano, F. Vetrano, and E. Santamato, "Orbital and spin photon angular momentum transfer in liquid crystals," *Physical Review Letters*, vol. 86, no. 11, p. 2285, 2001.

[116] M. Andersen, C. Ryu, P. Cladé, V. Natarajan, A. Vaziri, K. Helmerson, and W. D. Phillips, "Quantized rotation of atoms from photons with orbital angular momentum," *Physical Review Letters*, vol. 97, no. 17, p. 170406, 2006.

[117] S. Van Enk and G. Nienhuis, "Commutation rules and eigenvalues of spin and orbital angular momentum of radiation fields," *Journal of Modern Optics*, vol. 41, no. 5, pp. 963–977, 1994.

[118] M. Babiker, C. Bennett, D. Andrews, and L. D. Romero, "Orbital angular momentum exchange in the interaction of twisted light with molecules," *Physical Review Letters*, vol. 89, no. 14, p. 143601, 2002.

[119] R. Jáuregui, "Rotational effects of twisted light on atoms beyond the paraxial approximation," *Physical Review A*, vol. 70, no. 3, p. 033415, 2004.

[120] D. L. Andrews, L. D. Romero, and M. Babiker, "On optical vortex interactions with chiral matter," *Optics Communications*, vol. 237, no. 1-3, pp. 133–139, 2004.

[121] V. Klimov, D. Bloch, M. Ducloy, and J. R. R. Leite, "Detecting photons in the dark region of Laguerre-Gauss beams," *Optics Express*, vol. 17, no. 12, pp. 9718–9723, 2009.

[122] Y. Tang and A. E. Cohen, "Optical chirality and its interaction with matter," *Physical Review Letters*, vol. 104, no. 16, p. 163901, 2010.

[123] D. L. Andrews, "On the conveyance of angular momentum in electronic energy transfer," *Physical Chemistry Chemical Physics*, vol. 12, no. 27, pp. 7409–7417, 2010.

[124] C. T. Schmiegelow and F. Schmidt-Kaler, "Light with orbital angular momentum interacting with trapped ions," *The European Physical Journal D*, vol. 66, no. 6, p. 157, 2012.

[125] P. K. Mondal, B. Deb, and S. Majumder, "Angular momentum transfer in interaction of Laguerre-Gaussian beams with atoms and molecules," *Physical Review A*, vol. 89, no. 6, p. 063418, 2014.

[126] H. Scholz-Marggraf, S. Fritzsche, V. Serbo, A. Afanasev, and A. Surzhykov, "Absorption of twisted light by hydrogenlike atoms," *Physical Review A*, vol. 90, no. 1, p. 013425, 2014.

[127] A. Afanasev, C. E. Carlson, and A. Mukherjee, "High-multipole excitations of hydrogen-like atoms by twisted photons near a phase singularity," *Journal of Optics*, vol. 18, no. 7, p. 074013, 2016.

[128] A. Peshkov, V. Serbo, S. Fritzsche, and A. Surzhykov, "Absorption of twisted light by a mesoscopic atomic target," *Physica Scripta*, vol. 91, no. 6, p. 064001, 2016.

[129] E. Leader, "The photon angular momentum controversy: Resolution of a conflict between laser optics and particle physics," *Physics Letters B*, vol. 756, pp. 303–308, 2016.

[130] S. Franke-Arnold, "Optical angular momentum and atoms," *Phil. Trans. R. Soc. A*, vol. 375, no. 2087, p. 20150435, 2017.

[131] F. Araoka, T. Verbiest, K. Clays, and A. Persoons, "Interactions of twisted light with chiral molecules: An experimental investigation," *Physical Review A*, vol. 71, no. 5, p. 055401, 2005.

[132] W. Löffler, D. Broer, and J. Woerdman, "Circular dichroism of cholesteric polymers and the orbital angular momentum of light," *Physical Review A*, vol. 83, no. 6, p. 065801, 2011.

[133] R. Mathevet, B. V. de Lesegno, L. Pruvost, and G. L. Rikken, "Negative experimental evidence for magneto-orbital dichroism," *Optics Express*, vol. 21, no. 4, pp. 3941–3945, 2013.

[134] C. T. Schmiegelow, J. Schulz, H. Kaufmann, T. Ruster, U. G. Poschinger, and F. Schmidt-Kaler, "Transfer of optical orbital angu-

lar momentum to a bound electron," *Nature Communications*, vol. 7, p. 12998, 2016.

[135] F. Giammanco, A. Perona, P. Marsili, F. Conti, F. Fidecaro, S. Gozzini, and A. Lucchesini, "Influence of the photon orbital angular momentum on electric dipole transitions: Negative experimental evidence," *Optics Letters*, vol. 42, no. 2, pp. 219–222, 2017.

[136] G. Quinteiro, A. Lucero, and P. Tamborenea, "Electronic transitions in quantum dots and rings induced by inhomogeneous off-centered light beams," *Journal of Physics: Condensed Matter*, vol. 22, no. 50, p. 505802, 2010.

[137] C. Cohen-Tannoudji, J. Dupont-Roc, and G. Grynberg, *Photons and atoms: Introduction to quantum electrodynamics*. Wiley-VCH, 1997.

[138] J. H. Poynting, "On the transfer of energy in the electromagnetic field," *Proceedings of the Royal Society of London*, vol. 36, no. 228-231, pp. 186–187, 1883.

[139] J. Durnin, "Exact solutions for nondiffracting beams. I. The scalar theory," *J. Opt. Soc. Am. A*, vol. 4, pp. 651–654, Apr 1987.

[140] J. Durnin, J. Miceli Jr, and J. Eberly, "Diffraction-free beams," *Physical Review Letters*, vol. 58, no. 15, p. 1499, 1987.

[141] M. R. LaPointe, "Review of nondiffracting Bessel beams," in *Current Developments in Optical Design and Optical Engineering*, vol. 1527, pp. 258–277, International Society for Optics and Photonics, 1991.

[142] L. D. Romero, D. Andrews, and M. Babiker, "A quantum electrodynamics framework for the nonlinear optics of twisted beams," *Journal of Optics B: Quantum and Semiclassical Optics*, vol. 4, no. 2, p. S66, 2002.

[143] V. Fock, "Bemerkung zur quantelung des harmonischen oszillators im magnetfeld," *Zeitschrift für Physik A Hadrons and Nuclei*, vol. 47, no. 5, pp. 446–448, 1928.

[144] C. G. Darwin, "The diamagnetism of the free electron," *Mathematical Proceedings of the Cambridge Philosophical Society*, vol. 27, no. 1, p. 8690, 1931.

[145] R. Dingle, "Some magnetic properties of metals: I. General introduction, and properties of large systems of electrons," *Proc. R. Soc. Lond. A*, vol. 211, no. 1107, pp. 500–516, 1952.

[146] P. Maksym and T. Chakraborty, "Quantum dots in a magnetic field: Role of electron-electron interactions," *Physical Review Letters*, vol. 65, no. 1, p. 108, 1990.

[147] G. Quinteiro and P. Tamborenea, "Electronic transitions in disk-shaped quantum dots induced by twisted light," *Physical Review B*, vol. 79, no. 15, p. 155450, 2009.

[148] A. Niukkanen, "Clebsch-Gordan-type linearisation relations for the products of Laguerre polynomials and hydrogen-like functions," *Journal of Physics A: Mathematical and General*, vol. 18, no. 9, p. 1399, 1985.

[149] M. V. Berry, "Paraxial beams of spinning light," in *International conference on singular optics*, vol. 3487, pp. 6–12, International Society for Optics and Photonics, 1998.

[150] G. Molina-Terriza, J. P. Torres, and L. Torner, "Management of the angular momentum of light: Preparation of photons in multidimensional vector states of angular momentum," *Physical Review Letters*, vol. 88, no. 1, p. 013601, 2001.

[151] M. Vasnetsov, V. Pas' Ko, and M. Soskin, "Analysis of orbital angular momentum of a misaligned optical beam," *New Journal of Physics*, vol. 7, no. 1, p. 46, 2005.

[152] M. Abramowitz and I. A. Stegun, *Handbook of mathematical functions: With formulas, graphs, and mathematical tables*, vol. 55. Courier Corporation, 1965.

[153] F. Gori, G. Guattari, and C. Padovani, "Bessel-Gauss beams," *Optics Communications*, vol. 64, no. 6, pp. 491–495, 1987.

[154] B. G. Korenev, *Bessel functions and their applications*. CRC Press, 2003.

[155] R. W. Heeres and V. Zwiller, "Subwavelength focusing of light with orbital angular momentum," *Nano letters*, vol. 14, no. 8, pp. 4598–4601, 2014.

[156] M. E. Anderson, H. Bigman, L. E. de Araujo, and J. L. Chaloupka, "Measuring the topological charge of ultrabroadband, optical-vortex beams with a triangular aperture," *JOSA B*, vol. 29, no. 8, pp. 1968–1976, 2012.

[157] I. Zeylikovich, H. Sztul, V. Kartazaev, T. Le, and R. Alfano, "Ultrashort Laguerre-Gaussian pulses with angular and group velocity dispersion compensation," *Optics Letters*, vol. 32, no. 14, pp. 2025–2027, 2007.

[158] I. Mariyenko, J. Strohaber, and C. Uiterwaal, "Creation of optical vortices in femtosecond pulses," *Optics Express*, vol. 13, no. 19, pp. 7599–7608, 2005.

[159] K. Bezuhanov, A. Dreischuh, G. G. Paulus, M. G. Schätzel, and H. Walther, "Vortices in femtosecond laser fields," *Optics Letters*, vol. 29, no. 16, pp. 1942–1944, 2004.

[160] K. Bezuhanov, A. Dreischuh, G. G. Paulus, M. G. Schätzel, H. Walther, D. Neshev, W. Królikowski, and Y. Kivshar, "Spatial phase dislocations in femtosecond laser pulses," *JOSA B*, vol. 23, no. 1, pp. 26–35, 2006.

[161] E. I. Gordon, "A review of acoustooptical deflection and modulation devices," *Applied Optics*, vol. 5, no. 10, pp. 1629–1639, 1966.

Appendix A

Building the Fork Grating

A fork diffraction grating can be generated by numerically calculating the intensity profile that results from interference between a tilted plane wave and a twisted wave. We attempted to build a normal fork grating and a blazed fork grating. These gratings were displayed on the SLM, and by shining a plane wave on these gratings, beams with different orders were created.

A.1 Normal Fork Grating

The first type of fork grating we used to create twisted light was a normal fork grating, in which the incident beam gets diffracted into several different orders. The 0 order is just the plane wave, and the first orders are the twisted waves with OAMs of $+\ell$ and $-\ell$, as shown in Figure A.1. As the order increases, the light intensity decreases. Therefore, we usually use the first diffracted order and block the other beams.

Mathematica code used to build this fork grating is:

```
w= w0 (1 + (z^2/zR^2) );
w1= 100*200^-6;
w0set= 2^-6;
\[Lambda]0 = 800^-9;
Ixy2 = FullSimplify[ ComplexExpand[(.5 Exp[I(kx
```

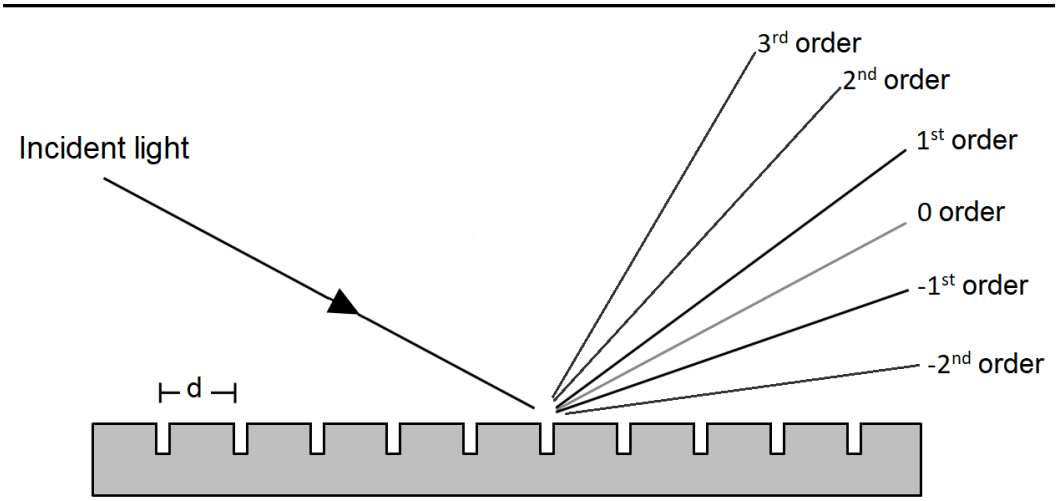

Figure A.1: Diffraction at a normal grating. The incident light gets diffracted into multiple diffraction orders in addition to the 0 order.

```
        +\[CapitalDelta]\[Phi])]+.5 Exp[I l ArcTan[y, x]])
        *Conjugate[.5 Exp[I (kx +\[CapitalDelta]\[Phi])]
        +.5 Exp[I l ArcTan[y, x]]]]];
Grating0 = Ixy2 /. {k -> 11*2 \[Pi]/\[Lambda]0/8,
        w0 -> w0set, zR -> \[Pi] w0set^2/\[Lambda]0,
        z -> 10^-4, p -> 0, l -> 0, r -> Norm[{x, y}],
        \[CapitalDelta]\[Phi] -> 0};
Grating1 = Ixy2 /. {k -> 11*2 \[Pi]/\[Lambda]0/8,
        w0 -> w0set, zR -> \[Pi] w0set^2/\[Lambda]0,
        z -> 10^-4, p -> 0, l -> 1, r -> Norm[{x, y}],
        \[CapitalDelta]\[Phi] -> 0};
CG = MatrixPlot[Table[Grating0 + Grating0, {y, -w1/1000,
        w1/1000, w1/500000}, {x, -w1/1000, w1/1000,
        w1/500000}], ColorFunction -> "GrayTones",
        Frame ->False, PlotRangePadding -> 0]
```

A.2 Blazed Fork Grating

A blazed fork grating, also known as an echelette grating, is a diffraction grating with grooves that have a sawtooth profile. This grating is designed to achieve maximum grating efficiency in a specific diffraction order. Therefore, the optical power will be maximized in the desired diffraction order while minimized in the other orders. Figure A.2 shows diffraction at a blazed grating, and figure A.3 shows the generated fork grating and blazed fork grating for

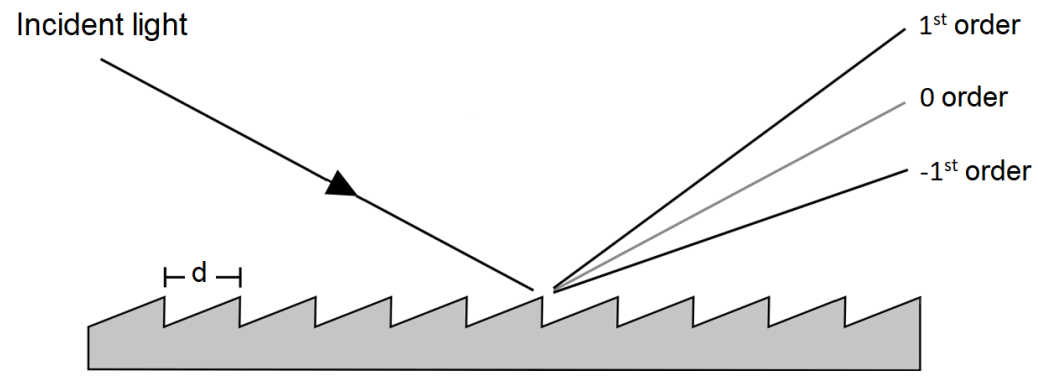

Figure A.2: Schematic of a blazed grating surface. The incident light is diffracted into a specific diffraction order, which maximizes the optical power in that order.

$\ell = 1$.

The code used to build a blazed fork grating is:

```
R[x_, y_] := Norm[{x, y}];
th[x_, y_] := Piecewise[{{2\[Pi]-ArcCos[x/Norm[{x, y}]],
    y >= 0}, {ArcCos[x/Norm[{x, y}]],
    y < 0}} spiral[x_, y_] := l th[x, y];

sawtooth[s_] := SawtoothWave[{-1, 1}, s/(2 \[Pi])];
contrastfunction[gratin_, contrast_, npix_] :=
    Module[{inmax, inmin},
    inmax = Max[gratin];
    inmin = Min[gratin];
```

```
    scaledinitial =
    ((gratin - inmin) (npix - 1))/(inmax - inmin);
    scaledcontrast = scaledinitial contrast;
    shifted = scaledcontrast - 127 (contrast - 1);
    shifted = Clip[shifted, {0, npix-1}]; shifted];

nx = 1080;
ny = 1920;
l = 1;
tilt = -100;
contrast = 3;
ampfork := Monitor[Table[Re[E^(I (spiral[x, y]
    + tilt 2 \[Pi] x/2))],
    {x, -1, 1, (1 - (-1))/(nx - 1)},
    {y, -1, 1, (1 - (-1))/(ny - 1)}], N[x]];
blazefork :=  Monitor[Table[
    Re[sawtooth[spiral[x, y] +tilt 2 \[Pi] y/2]],
    {x, -1, 1, (1 - (-1))/(nx - 1)},
    {y, -1, 1, (1 - (-1))/(ny - 1)}], N[x]];

MatrixPlot[N[ampfork], ColorFunction -> "GrayTones",
    Frame -> False,  PlotRangePadding -> 0,
    ImageSize -> 1080];
blazeforkvalues = N[blazefork];
enhblazefork = contrastfunction[blazeforkvalues,
```

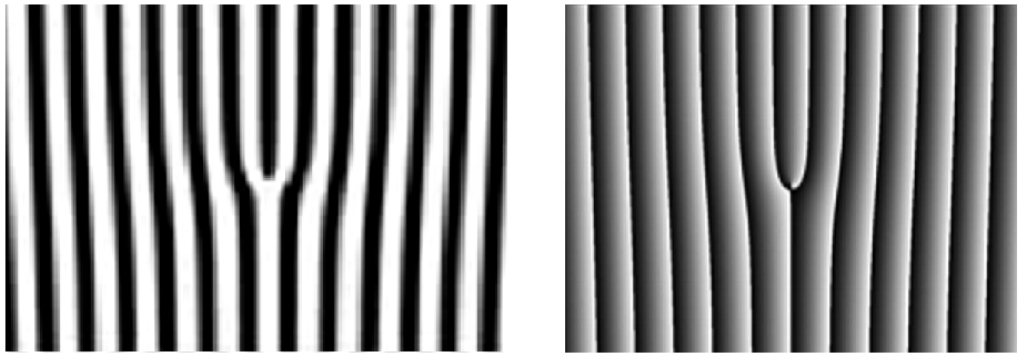

Figure A.3: The generated grating for $\ell = 1$ for: (a) normal fork grating and (b) blazed fork grating.

```
        contrast , 256];
FG = MatrixPlot[enhblazefork , ColorFunction-> "GrayTones",
        PlotRangePadding -> 0, ImageSize -> 1920]
```

Appendix B

Alignment Process for a Ti:Sapphire Oscillator

This appendix describes the components and the alignment procedure of the Ti:sapphire femtosecond laser used in this work.

B.1 Components

The laser cavity contains:

- A continuous-wave (cw) green laser with 4 to 4.5 W pump power and wavelength of 514 nm
- Lasing medium of titanium-doped sapphire crystal
- A pair of fused silica prisms for dispersion compensation
- High-reflectively broadband mirrors (>0.99); silver-coated mirrors are less effective because they might get distorted from the pump laser high intensity
- Curved mirrors with antireflection coatings for the pump laser wavelength on the planar side and a curvature of R = 10 cm on the concave side
- Output coupler that transmits ∼12% of the pump power

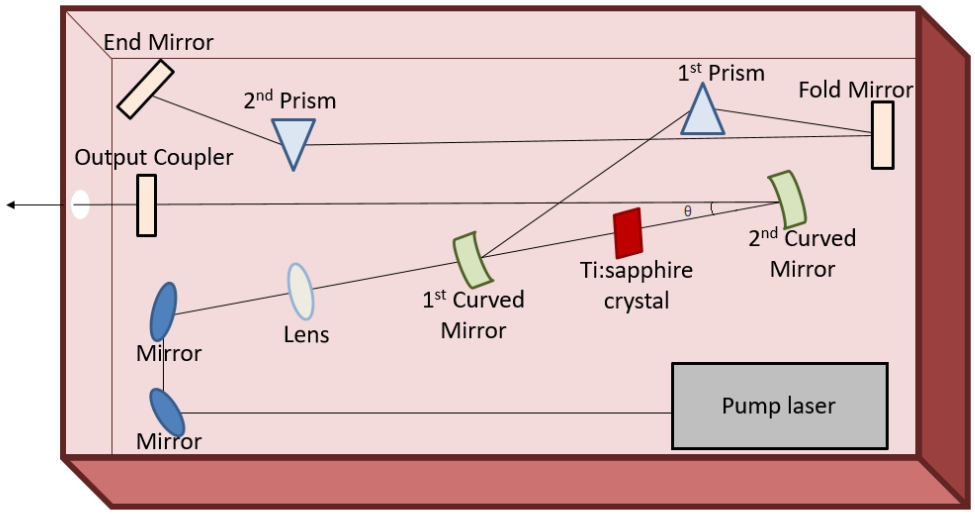

Figure B.1: Ti:sapphire laser parameters and the beam path in the cavity.

Figure B.1 shows the Ti:sapphire components and the beam path in the cavity. In a single trip through the cavity, the beam bounces on the end mirror and the output coupler once, then it bounces twice on the two curved mirrors and the fold mirror, then it passes through the crystal and both prisms twice.

Within the cavity, the path lengths and the distances between the optics are important for correct dispersion compensation and mode locking. The distance between the output coupler and the second curved mirror is 62 cm, the distance between the first and second curved mirror is 10.4 cm, the distance between the first curved mirror and the first prism is 22 cm, the total distance between the first and second prism is 62 cm, the distance between the second prism and the end mirror is 5 cm, and the angle $\theta = 16°$.

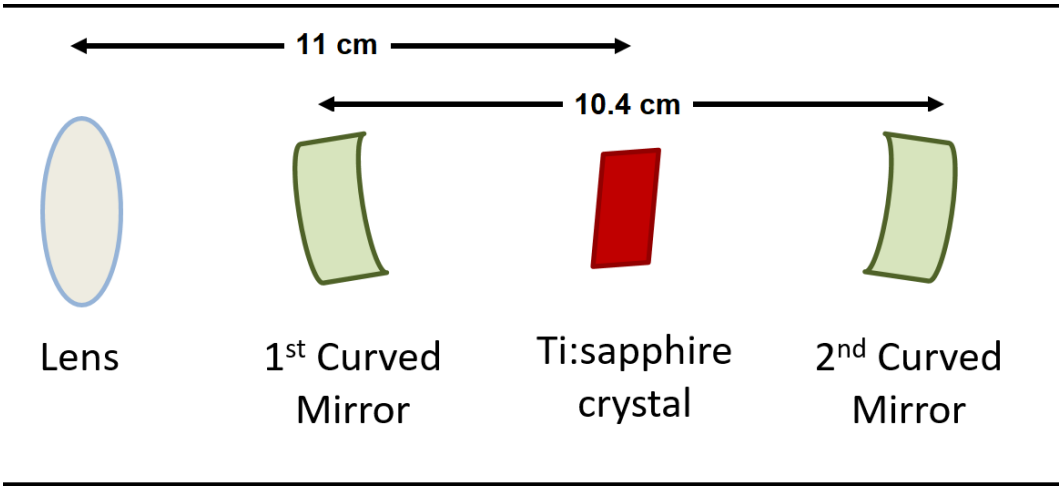

Figure B.2: Distances between the optics on the rail.

B.2 Alignment

The alignment process usually starts with aligning the optics to get the oscillator to lase, then maximizing the output power, and finally mode-locking the laser. The alignment process in detail is:

- Align the pump beam along the rail. The beam should be parallel to the rail and also to the table. This can be done by removing all optics and aligning using two mirrors and two pinholes. The height of the beam can be adjusted to match the height of the crystal. Then, place the lens so that the beam passes through the center of the lens. After that, place the curved mirrors and the crystal. The beam should pass through the crystal at the focus of the lens and through the centers of the curved mirrors. The two curved mirrors should be symmetric about the crystal, roughly 10.4 cm apart. The distances between the crystal and both curved mirrors are shown in Figure B.3.

- Adjust the central translational axis of the rail to an angle of 16 degrees to the grid of table, and make sure that the reflection of the second curved mirror to the output coupler is parallel to the grid.

- A bright reddish fluorescence propagating through the cavity allows alignment for lasing. To reduce total dispersion, we adjust the prisms so that the beams eventually propagate through the minimum amount of glass. However, the alignment is easier when we have the maximum amount of fluorescent light propagating through the cavity, so we start by setting the prism translation stages at the middle of their scale. Moreover, to improve the visibility of the fluorescence, this can be done with low room lights or even in the dark.

- Set the first prism at minimum deviation, where the minimum deviation defines the angle at which the beam enters and exits the prism at the Brewster angle, and so passes through the prism parallel to its base. After that, we adjust the fold mirror so that the incidence angle is small and then set the second prism at minimum deviation. Finally, reflect the fluorescence spot with the end mirror.

- If the rail optics are close to their optimal positions, we should be able to see a specific shape to the fluorescence at the first prism, as shown in Figure B.3a. The diameter of the larger red spot is roughly the size of the prism. This is the light reflected from the crystal, and we can adjust its size by adjusting the crystal position. The smaller spot is the light reflected from the output coupler. It may not be in focus at the first prism, but this can be fixed by adjusting the translational position of

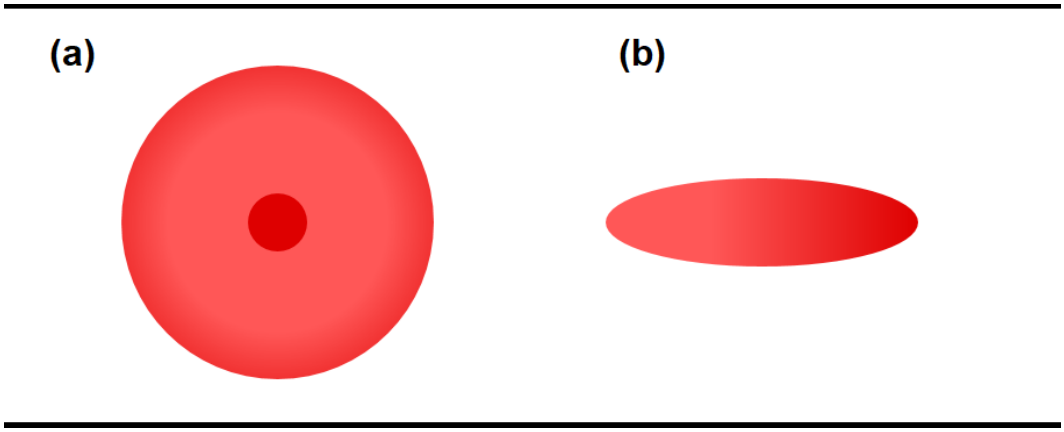

Figure B.3: The fluorescence shape appearance at (a) first prism and (b) second prism.

the second curved mirror reflecting to the output coupler. Once we see this shape at the first prism, we should see a spatially dispersed shape to the fluorescence at the second prism, as shown in Figure B.3b. If the fluorescence does not appear as described, make small adjustments in the translational positions of the second curved mirror and crystal.

- The reflected beam from the end mirror must be aligned to overlap with that of the output coupler. The two beams can be seen easily with an index card at the fold mirror. We can adjust the crystal and the second curved mirror so that the two spots of fluorescence are focused at the fold mirror. When the beams are aligned, and by making small adjustments to the output coupler, end mirror, and the position of the second curved mirror, lasing can be initiated. The oscillator will lase only when the mirrors are aligned accurately, and the second curved mirror and crystal are in approximately the correct positions. The distances between the curved mirrors and the end mirrors are not very important for cw oper-

ation, although they become more significant for mode-locking stability. It is also useful to make sure that the fluorescence is passing through the centers of the prisms. Later, when mode locking, the prism positions will probably require some adjustment for optimal dispersion compensation.

- After the laser lases, we can increase the peak power by adjusting the horizontal and vertical tilt of the output coupler and the end mirror. Also, small tweaks to the curved mirror and the crystal translational positions will greatly help to increase the power. At 4 to 4.5 W of pump power, the laser will usually have an output power of about 200 to 300 mW.

- Another approach for increasing the cw power is to align the green and red beams in the crystal so that there is efficient coupling between the two beams. This can be done by looking at the scatter of both beams on either of the curved mirrors. The green beam would appear slightly to the left of the red beam, as seen in Figure B.4a. Alignment for the highest power should associate with this configuration. However, if the two beams are significantly separated, or if the green beam appears to the right of the red, this might suggest that the red beam is being clipped somewhere within the cavity.

- Now that the laser is lasing and the peak power is maximized, we can start the process of mode-locking the laser. The distance between the second curved mirror and the crystal is one of the critical components for mode locking. In fact, the oscillator will lase for a range of values for this distance, but mode locks for a specific distance between the

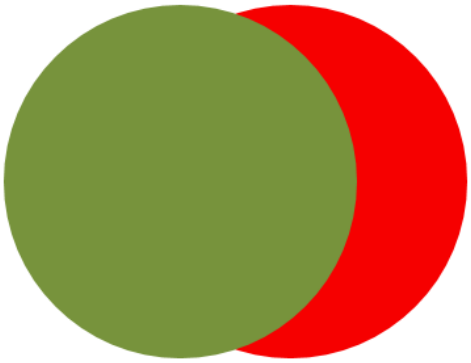

Figure B.4: Shape of the green and red beams at either of the curved mirrors for maximum coupling between the two beams.

second curved mirror and the crystal. When the oscillator is lasing, there will be two regions where the laser is stable. Starting with the biggest distance between the second curved mirror and the crystal at which the cavity is still lasing and moving the second curved mirror closer to the crystal, the laser will stop lasing at one point, start again as the mirror is moved further, then stop lasing again. The most stable mode locking will happen when the second curved mirror has been moved to the inside of the outer stability region. In other words, mode locking will be most stable just before the first stop of lasing as the second curved mirror is moved closer to the crystal. When the laser is aligned in cw mode, it should have highest power when the second curved mirror is farthest from the crystal.

- Running at high output power, the laser may be favoring continuous mode. Therefore, move the second curved mirror toward the crystal until the output power is reduced. Then use only the output coupler

and end mirror to increase the power as high as it will go. To mode-lock the laser, give the translation stage of the first prism a quick push to introduce a brief fluctuation in the intensity of the beam, since the cavity is aligned to favor mode-locked operation. The power may be increased by slight adjustments to the end mirror and the output coupler.

Not all these steps are required every time the laser is used. The daily routine is usually to maximize the cw power by adjusting the output coupler and the end mirror, followed by a quick push for the first prism. If the laser is not mode locking or not lasing, go through alignment process starting from the third step (we don't need to do the first two because we almost never change the optics position). Moreover, if the cw power is lower than usual, cleaning the optics may be helpful.

B.2.1 Rail micrometers

The translational position for the optics are:

- Crystal: 4.96 mm
- First curved mirror: 0.253 inch
- Second curved mirror for max cw power: 7.13 mm
- Second curved mirror for mode-locked operation: 7.918 mm
- Lens: 0.4287 inch
- First prism: 2.12 mm
- Second prism: 0.318 inch